

**ISTANBUL TECHNICAL UNIVERSITY ★ GRADUATE SCHOOL OF SCIENCE**  
**ENGINEERING AND TECHNOLOGY**

**FABRICATION AND CHARACTERIZATION OF NANOTUBULAR Ti AND  
TiAl ANODIC OXIDE FILMS FOR GAS SENSING APPLICATION**

**Ph.D. THESIS**

**Fatma BAYATA**

**Advanced Technologies**

**Materials Science and Engineering Programme**

**FEBRUARY 2013**



**ISTANBUL TECHNICAL UNIVERSITY ★ GRADUATE SCHOOL OF SCIENCE**  
**ENGINEERING AND TECHNOLOGY**

**FABRICATION AND CHARACTERIZATION OF NANOTUBULAR Ti AND  
TiAl ANODIC OXIDE FILMS FOR GAS SENSING APPLICATION**

**Ph.D. THESIS**

**Fatma BAYATA**  
**(521062011)**

**Advanced Technologies**

**Materials Science and Engineering Programme**

**Thesis Advisor: Prof. Dr. Mustafa ÜRGEN**

**FEBRUARY 2013**



**İSTANBUL TEKNİK ÜNİVERSİTESİ ★ FEN BİLİMLERİ ENSTİTÜSÜ**

**GAZ ALGILAMA UYGULAMALARINDA KULLANILMAK ÜZERE  
NANOTÜPLÜ Ti VE TiAl ANODİK OKSİT FİMLERİN ÜRETİMİ VE  
KARAKTERİZASYONU**

**DOKTORA TEZİ**

**Fatma BAYATA  
(521062011)**

**İleri Teknolojiler Anabilim Dalı**

**Malzeme Bilimi ve Mühendisliği Programı**

**Tez Danışmanı: Prof. Dr. Mustafa ÜRGEN**

**ŞUBAT 2013**



**Fatma BAYATA, a Ph.D. student of ITU Graduate School of Science Engineering and Technology student ID 521062011 successfully defended the thesis/dissertation entitled “FABRICATION AND CHARACTERIZATION OF NANOTUBULAR Ti AND TiAl ANODIC OXIDE FILMS FOR GAS SENSING APPLICATION”, which she prepared after fulfilling the requirements specified in the associated legislations, before the jury whose signatures are below.**

**Thesis Advisor :**      **Prof. Dr. Mustafa ÜRGEN**      .....  
Istanbul Technical University

**Jury Members :**      **Prof. Dr. Servet TİMUR**      .....  
Istanbul Technical University

**Assoc.Prof. Dr. Oğuzhan GÜRLÜ**      .....  
Istanbul Technical University

**Prof. Dr. Gökhan ORHAN**      .....  
Istanbul University

**Prof. Dr. Müzeyyen MARŞOĞLU**      .....  
Yıldız Technical University

**Date of Submission : 28 December 2012**  
**Date of Defense : 19 February 2013**





*To my parents,*



## **FOREWORD**

I would like to express my sincerest thanks the many people who made this thesis possible. In particular:

Foremost, I am deeply indebted to Prof. Mustafa ÜRGEN for supervising my PhD work and for providing me the opportunity to work with him and his group. He has been a steady influence throughout my Ph.D. study; he has oriented and supported me with promptness and care, and has always been patient and encouraging in times of new ideas and difficulties; he has listened to my ideas and discussions with him frequently led to key insights. His ability to select and to approach compelling research problems, his high scientific standards, and his hard work set an example. I could not have imagined having a better advisor and mentor for my Ph.D study.

I would like to express my special thanks to Assoc. Prof. Dr. Kürşat KAZMANLI for insightful comments both in my work and in this thesis, for his support, and for many motivating discussions.

The members of my dissertation committee, Prof. Dr. Servet TİMUR and Assoc. Prof. Oğuzhan GÜRLÜ, have generously given their time and expertise to better my work. I thank them for their contribution and their good-natured support.

I wish to express my special thanks to Prof. Dr. Gültekin GÖLLER who has provided the support and equipment I have needed to produce and complete my thesis.

I would also like to thank Hüseyin SEZER, Talat ALPAK , Sevgin TÜRKEİ, for their technical support and help throughout this work. Thanks to all of you. This thesis would not have happened without your help.

I would like to express my sincerest thanks all my Proffessors and the staff in Faculty for their considerable contributions to my Ph.D study.

I would like to express my special thanks to Filiz KARAOSMANOĞLU, for her scientific support but most importantly for believing in me and always having time for me. Her insights and comments about my education and my life are invaluable over the years.

I would like to acknowledge the technical support of Deutschen Zentrum für Luft- und Raumfahrt (DLR) for my sensor tests. I would also like to thank Dr. Bilge SARUHAN-BRINGS for her technical support but also for being the perfect host during my stay in DLR. I am particularly thankful to Philipp for his help in my sensor tests. I had also the pleasure to work with Yakup GÖNÜLLÜ, Ayhan YÜCE and Cesar RODRIGUES.

I would like thank TÜBİTAK for the financial support to my PhD study. The work on this thesis was supported by the TÜBİTAK under project number 110M745. Especially, I would like to thank my friends, Sinan AKKAYA, Semih ÖNCEL, Erdem ARPAT for helping me produce coating samples.

In addition, I have been very privileged to get to know and to collaborate with many other great people who became friends over the last several years. Special thanks to; Gizem, Özden, Sinem, Eren, Güldem, Özgenur, Mehmet, Nagihan, Beril, Münevver, Emek, Ebru, Dilek, Alper, Özgen and many other my friends.

Last but not least, I would like to thank Seyhan, who as a good friend, has always willing to help and give her best suggestions.

Finally, I would like to deeply thank my mother, my father, my elder brothers and my elder sister, for their love, support, and encouragement throughout my life. It is to them that I dedicate this work.

December 2012

Fatma BAYATA

## TABLE OF CONTENTS

	<u>Page</u>
<b>FOREWORD</b> .....	<b>ix</b>
<b>TABLE OF CONTENTS</b> .....	<b>xi</b>
<b>ABBREVIATIONS</b> .....	<b>xiii</b>
<b>LIST OF TABLES</b> .....	<b>xv</b>
<b>LIST OF FIGURES</b> .....	<b>xvii</b>
<b>SUMMARY</b> .....	<b>xxiii</b>
<b>ÖZET</b> .....	<b>xxvii</b>
<b>1. INTRODUCTION</b> .....	<b>1</b>
1.1 Gas Sensors and Their Operating Principles .....	1
1.2 Types of Gas Sensors .....	1
1.3 Semiconductor Based Chemiresistive Sensors .....	2
1.3.1 The characteristics of semiconductor based chemiresistive sensors .....	3
1.3.2 Problems associated with metal oxide sensors .....	5
1.4 TiO <sub>2</sub> Based Gas Sensors .....	6
1.4.1 <i>n</i> -type and p-type behavior of TiO <sub>2</sub> based gas sensors .....	6
1.4.2 Doped TiO <sub>2</sub> Based Gas Sensors .....	7
1.4.3 The effects of adding dopant elements into TiO <sub>2</sub> .....	8
1.4.4 The anatase-rutile phase transition temperatures of TiO <sub>2</sub> .....	8
1.4.5 The inhibiting and promoting dopants for TiO <sub>2</sub> .....	10
1.4.6 Modification of the anatase-rutile phase transition temperatures of TiO <sub>2</sub> with various dopant elements .....	11
1.4.7 The effects of adding Al dopant on gas sensing properties of TiO <sub>2</sub> based gas sensors.....	14
1.4.8 The effects of Al doping on TiO <sub>2</sub> structure.....	14
1.5 Hydrogen Gas Sensors .....	16
1.6 The Sensing Mechanism of TiO <sub>2</sub> Based Gas Sensors .....	17
1.6.1 H <sub>2</sub> sensing mechanism of TiO <sub>2</sub> based gas sensors .....	17
1.7 Nanostructured Gas Sensors .....	20
1.7.1 Nanostructured TiO <sub>2</sub> based gas sensors .....	21
1.7.2 Nanostructured TiO <sub>2</sub> based thin film gas sensors .....	22
1.7.3 H <sub>2</sub> sensing mechanism in nanotubular TiO <sub>2</sub> based sensors .....	22
1.7.4 The Effects of crystallographic structure of TiO <sub>2</sub> nanotubes on sensing properties.....	24
1.7.5 The effects of TiO <sub>2</sub> nanotube sizes on gas sensing properties .....	25
1.8 TiO <sub>2</sub> Nanotubular Structures .....	25
1.8.1 The nanotube growth mechanism on the surface of Ti metal .....	25
1.8.2 Anodization parameters influencing the nanotube morphology .....	27
1.8.3 The nano structures grown on Ti alloys .....	29
1.9 The Deposition Techniques for Producing Ti or TiO <sub>2</sub> Thin Film Coatings.....	30

<b>2. EXPERIMENTAL DETAILS.....</b>	<b>33</b>
<b>3. INVESTIGATION OF THE CAPVD PROCESS PARAMETERS FOR THE DEPOSITION OF WELL ADHERENT AND DENSE Ti AND TiAl COATINGS.....</b>	<b>37</b>
3.1 Investigation of the CAPVD Process Parameters for the Deposition of Ti Coatings .....	38
3.1.1 The effects of bias voltage on microstructural properties of Ti coating ...	38
3.1.2 The effects of post treatment with high bias voltage on microstructural properties of Ti coating .....	41
3.1.3 The effects of bias voltage on structural properties of Ti coating .....	44
3.1.4 The effects of post treatment with high bias voltage on the structural properties of Ti coating .....	44
3.2 Investigation of the CAPVD Process Parameters for the Deposition of Ti-Al Coatings .....	47
3.2.1 The effects of bias voltage on microstructural properties TiAl coating....	47
3.2.2 The effects of post treatment with high bias voltage on microstructural properties TiAl coating .....	50
3.2.3 The effects of bias voltage on structural properties TiAl coating .....	53
3.2.4 The effects of post treatment with high bias voltage on structural properties TiAl coating .....	55
<b>4. OPTIMIZATION OF PROCESS PARAMETERS FOR THE ANODIZATION OF Ti AND TiAl COATINGS.....</b>	<b>61</b>
4.1 Optimization of Process Parameters for the Anodization of TiAl Coatings ....	62
4.1.1 The effect of electrolyte composition.....	64
4.1.2 The effects of potential in TiAl coating anodization.....	69
4.1.3 The effects of temperature in TiAl coating anodization .....	70
4.1.4 The effects of water content in electrolyte in TiAl coating anodization...	72
4.1.5 The effects of anodization duration in TiAl coating anodization.....	73
4.1.6 The effects of agitation in TiAl coating anodization.....	75
4.2 Optimization of Process Parameters for the Anodization of Ti Coatings .....	76
4.3 The Influence of Different Coating Structures on Anodization Process .....	78
<b>5. INVESTIGATION OF AMORPHOUS TO ANATASE AND ANATASE TO RUTILE PHASE TRANSFORMATIONS IN NANOSTRUCTURED Ti AND TiAl ANODIC OXIDES.....</b>	<b>81</b>
5.1 The Crystallization Behavior of Nanostructured Ti and TiAl Anodic Oxides.	81
5.2 The Effect of Al Doping on TiO <sub>2</sub> Crystal Structure.....	92
5.3 The Role Al Dopant on Grain Size.....	95
5.4 The Effect of Al Doping on Anatase-Rutile Transformation .....	96
<b>6. H<sub>2</sub> SENSING PROPERTIES OF NANOSTRUCTURED Ti AND TiAl ANODIC OXIDES .....</b>	<b>99</b>
6.1 Fabrication and Characterization of Sensor Electrode Materials .....	99
<b>7. CONCLUSION.....</b>	<b>111</b>
<b>REFERENCES .....</b>	<b>117</b>
<b>APPENDICES .....</b>	<b>125</b>
<b>CURRICULUM VITAE .....</b>	<b>129</b>

## **ABBREVIATIONS**

<b>CAPVD</b>	: Cathodic Arc Physical Vapor Deposition
<b>RF</b>	: Radio Frequency
<b>SEM</b>	: Scanning Electron Microscopy
<b>FEG-SEM</b>	: Field Emission Gun Scanning Electron Microscopy
<b>EDS</b>	: Energy Dispersive Spectrometer
<b>XRD</b>	: X-Ray Diffraction
<b>PXRD</b>	: Powder (theta-2theta) X-Ray Diffraction
<b>GAXRD</b>	: Glancing Angle X-Ray Diffraction
<b>DC</b>	: Direct Current





## LIST OF TABLES

	<u>Page</u>
<b>Table 1.1 :</b> A list of gas sensors and their detection principles .....	2
<b>Table 1.2 :</b> The representative list of some of the chemiresistive materials .....	3
<b>Table 1.3 :</b> Some of the reported anatase-rutile transition temperatures for titania depending on their process methods . .....	9
<b>Table 3.1 :</b> The EDS analyses of TiAl coatings deposited at 0 V, 100 V, 200 V bias voltages.....	50
<b>Table 3.2 :</b> The surface EDS analyses of TiAl coatings deposited at 0 V, 100 V, 200 V bias voltage and successively subjected to post treatment with high bias voltage.....	53
<b>Table 4.1 :</b> EDS analyses of porous and nanotubular layer formed on the surface of TiAl coating after anodization process.....	68
<b>Table 6.1 :</b> Calculated sensor parameters for nanotubular TiAl anodic oxide sensor for different hydrogen concentrations at RT, 100°C, 200°C, 250°C, 300°C and 350°C.....	103
<b>Table 6.2 :</b> H <sub>2</sub> sensing properties of the TiO <sub>2</sub> sensors produced by various techniques.....	109



## LIST OF FIGURES

	<u>Page</u>
<b>Figure 1.1</b> : Operation principle of gas sensor .....	1
<b>Figure 1.2</b> : The schematic representation of response curve of a chemiresistive sensors .....	5
<b>Figure 1.3</b> : The effects of various cations on the phase transition temperatures in titania .....	9
<b>Figure 1.4</b> : Experimental and predicted inhibition of anatase to rutile transformation .....	10
<b>Figure 1.5</b> : The valence-radius plot of anatase to rutile transformation which is categorising inhibiting and promoting dopant elements.....	10
<b>Figure 1.6</b> : The transition temperature of anatase-rutile is plotted as a function of the ionic radius of the dopants .....	12
<b>Figure 1.7</b> : The binary $\text{TiO}_2\text{-Al}_2\text{O}_3$ phase diagram .....	16
<b>Figure 1.8</b> : Band bending after chemisorption of charged species (here ionosorption of oxygen on $E_{ss}$ levels). $\phi$ denotes the work function, $\chi$ is the electron affinity, and $\mu$ the electrochemical potential, $qV_s$ is the band bending and $z_0$ is the depth of depleted layer. $E_{vac}$ , $E_{Cb}$ , $E_{Vb}$ , $E_F$ are the vacuum energy level, bottom of the conductive band, top of the valence band and Fermi level energies, respectively. $E_{Cs}$ , $E_{Vs}$ are the values of conductive and valence band borders at the surface, $E_d$ and $E_{ss}$ are the levels of donors and surface states.....	19
<b>Figure 1.9</b> : Energy barriers formation at the grain boundaries due to the formation of space charge layer .....	20
<b>Figure 1.10</b> : The schematic illustration of grain size effect on gas sensitivity.....	21
<b>Figure 1.11</b> : The influence of nanotube wall thickness on band bending due to oxygen chemisorption: (a) when nanotube wall half-thickness ( $t/2$ ) is much greater than the space charge layer, (b) when comparable, and (c) when $t/2$ is less than the width of the space charge region. (d) Schematic illustration of nanotubes, top view, and the tube-to-tube connecting points corresponding to case shown in (a) .....	23
<b>Figure 1.12</b> : Schematic representation of the Ti anodization (a) in absence of fluorides (results in flat layers), and (b) in presence of fluorides (results in the tube growth) .....	27
<b>Figure 1.13</b> : The surface SEM images of a) Ti thin film produced by Rf sputtering technique b) the as-anodized surface of Ti thin film by RF sputtering technique .....	31
<b>Figure 3.1</b> : The surface SEM images of Ti deposited alumina produced by magnetron sputtering after anodization process .....	37
<b>Figure 3.2</b> : The SEM image of TiAl deposited alumina produced by magnetron sputtering after anodization process. ....	38

<b>Figure 3.3 :</b> The surface SEM image of Ti coating deposited on alumina at 0 V bias voltage using CAPVD technique. ....	39
<b>Figure 3.4 :</b> The surface SEM image of Ti coating deposited on alumina at 0 V bias voltage using CAPVD technique. ....	39
<b>Figure 3.5 :</b> The surface SEM image of Ti coating deposited on alumina at 100 V bias voltage using CAPVD technique. ....	40
<b>Figure 3.6 :</b> The surface SEM image of Ti coating deposited on alumina at 200 V bias voltage using CAPVD technique. ....	40
<b>Figure 3.7 :</b> The cross sectional SEM image of Ti coating deposited on alumina at 0 V bias voltage using CAPVD technique. ....	40
<b>Figure 3.8 :</b> The cross sectional SEM image of Ti coating deposited on alumina at 100 V bias voltage using CAPVD technique. ....	41
<b>Figure 3.9 :</b> The cross sectional SEM image of Ti coating deposited on alumina at 200 V bias voltage using CAPVD technique. ....	41
<b>Figure 3.10 :</b> SEM image of Ti coating which was deposited on alumina at 0 V bias voltage and then exposed to 1000 V high voltage. ....	42
<b>Figure 3.11 :</b> SEM image of Ti coating which was deposited on alumina at 100 V bias voltage and then exposed to 1000 V high voltage. ....	42
<b>Figure 3.12 :</b> SEM image of Ti coating which was deposited on alumina at 200 V bias voltage and then exposed to 1000 V high voltage. ....	43
<b>Figure 3.13 :</b> Cross sectional SEM image of Ti coating which was deposited on alumina at 0 V bias voltage and then exposed to 1000 V high voltage. ....	43
<b>Figure 3.14 :</b> Cross sectional SEM image of Ti coating which was deposited on alumina at 100 V bias voltage and then exposed to 1000 V high voltage. ....	43
<b>Figure 3.15 :</b> Cross sectional SEM image of Ti coating which was deposited on alumina at 200 V bias voltage and then exposed to 1000 V high voltage. ....	44
<b>Figure 3.16 :</b> The comparison of normalized XRD patterns of Ti coatings deposited on alumina at 0 V, 100 V and 200 V bias voltage using CAPVD technique. Red lines denote the XRD peak positions taken from PCPDF file 44-1294. ....	45
<b>Figure 3.17 :</b> The comparison of normalized XRD patterns of Ti coatings deposited on alumina at 0 V, 100 V and 200 V bias voltage and successively subjected to 1000 V. Red lines denote the XRD peak positions taken from PCPDF file 44-1294. ....	45
<b>Figure 3.18 :</b> Comparison of normalized XRD patterns of Ti coating deposited on alumina at 100 V and 1000 V high bias voltage applied Ti coating deposited at 100 V. Red lines denote the XRD peak positions taken from PCPDF file 44-1294. ....	46
<b>Figure 3.19 :</b> Comparison of normalized XRD patterns of Ti coating deposited on alumina at 100 V and 1000 V high bias voltage applied Ti coating deposited at 100 V in high magnification. Red lines denote the XRD peak positions taken from PCPDF file 44-1294. ....	46
<b>Figure 3.20 :</b> The SEM image of TiAl coating deposited on alumina at 0 V using CAPVD technique. ....	47
<b>Figure 3.21 :</b> The SEM image of TiAl coating deposited on alumina at 100 V using CAPVD technique. ....	48

<b>Figure 3.22 :</b>	The SEM image of TiAl coating deposited on alumina at 200 V using CAPVD technique. ....	48
<b>Figure 3.23 :</b>	The cross sectional SEM image of TiAl coating deposited on alumina at 0 V using CAPVD technique .....	49
<b>Figure 3.24 :</b>	The cross sectional SEM image of TiAl coating deposited on alumina at 100 V using CAPVD technique .....	49
<b>Figure 3.25 :</b>	The cross sectional SEM image of TiAl coating deposited on alumina at 200 V using CAPVD technique .....	49
<b>Figure 3.26 :</b>	The SEM image of TiAl coating deposited on alumina at 0 V and then subjected to 1000 V high bias voltage .....	51
<b>Figure 3.27 :</b>	The SEM image of TiAl coating deposited on alumina at 100 V and then exposed to 1000 V high bias voltage .....	51
<b>Figure 3.28 :</b>	The SEM image of TiAl coating deposited on alumina at 200 V and then subjected to 1000 V high bias voltage .....	51
<b>Figure 3.29 :</b>	The cross sectional SEM image of TiAl coating deposited on alumina at 0 V and then exposed to 1000 V high bias voltage.....	52
<b>Figure 3.30 :</b>	The cross sectional SEM image of TiAl coating deposited on alumina at 100 V and then exposed to 1000 V high bias voltage.....	52
<b>Figure 3.31 :</b>	The cross sectional SEM image of TiAl coating deposited on alumina at 200 V and then exposed to 1000 V high bias voltage.....	52
<b>Figure 3.32 :</b>	Al-Ti binary phase diagram.....	54
<b>Figure 3.33 :</b>	The normalized XRD patterns of TiAl coatings deposited on alumina at 0 V, 100 V and 200 V bias voltage using cathodic arc method. Red lines and blue lines denote the XRD peak positions taken from PCPDF file 44-1294 and 52-0859, respectively. ....	54
<b>Figure 3.34 :</b>	The comparison of normalized XRD patterns of TiAl coatings deposited on alumina at 0 V, 100 V and 200 V bias voltage and successively subjected to 1000 V. Red lines and blue lines denote the XRD peak positions taken from PCPDF file 44-1294 and 52-0859, respectively. ....	55
<b>Figure 3.35 :</b>	The comparison of normalized XRD patterns of TiAl coatings deposited on alumina at 0 V and 200 V bias voltage and successively subjected to 1000 V. Red lines and blue lines denote the XRD peak positions taken from PCPDF file 44-1294 and 52-0859, respectively. ....	56
<b>Figure 3.36 :</b>	Comparison of normalized XRD patterns of TiAl coating deposited at 100 V and TiAl coating deposited at 100 V successively applied 1000 V high voltage. Red lines and blue lines denote the XRD peak positions taken from PCPDF file 44-1294 and 52-0859, respectively. ....	57
<b>Figure 3.37 :</b>	Comparison of normalized XRD patterns of TiAl coating deposited on alumina at 100 V and 1000 V high bias voltage applied TiAl coating deposited at 100 V in high magnification. Red lines and blue lines denote the XRD peak positions taken from PCPDF file 44-1294 and 52-0859, respectively. ....	57
<b>Figure 4.1 :</b>	The SEM image of anodically oxidized TiAl coatings which have higher amount of droplets on their surfaces.....	62
<b>Figure 4.2 :</b>	The cross sectional image of anodically oxidized Ti coated alumina in ethylene glycol without any spalling. ....	63
<b>Figure 4.3 :</b>	The relationship between $\text{NH}_4\text{F}$ concentration in ethylene glycol electrolyte and nanotube in anodization process conducted at 40 V and 13°C. ....	65

<b>Figure 4.4 :</b> The cross sectional SEM image of nanotubular structure formed on TiAl coating after the anodization process conducted at 40 V and 13 °C in ethylene glycol containing 0.25 wt % NH <sub>4</sub> F. ....	65
<b>Figure 4.5 :</b> The cross sectional SEM image of nanotubular structure formed on TiAl coating after the anodization process conducted at 40 V and 13 °C in ethylene glycol containing 0.61 wt % NH <sub>4</sub> F. ....	66
<b>Figure 4.6 :</b> The SEM image of nanotubular structure formed on TiAl coating after the first anodization process conducted at 40 V and 13 °C in ethylene glycol containing 0.61 wt % NH <sub>4</sub> F. ....	67
<b>Figure 4.7 :</b> The SEM image of etched nanoporous structure using second anodization process conducted at 40 V in 0.6 v % HF containing electrolyte. ....	68
<b>Figure 4.8 :</b> The SEM image of resulting nanotubular structure formed on TiAl coating after the second anodization process. ....	68
<b>Figure 4.9 :</b> The cross sectional SEM image of nanotubular structure formed on TiAl coating after the anodization process conducted at 60V and 13°C for 250 min in 0.25 wt % NH <sub>4</sub> F containing electrolyte. ....	69
<b>Figure 4.10 :</b> The SEM image of nanotubular structure formed on TiAl coating after the anodization process conducted at 50V and 13°C for 120 min in 0.61 wt % NH <sub>4</sub> F containing electrolyte. ....	70
<b>Figure 4.11 :</b> The cross sectional SEM image of nanotubular structure formed on TiAl surface after 250 min anodic oxidation at 60 V in 0.25 wt % NH <sub>4</sub> F containing electrolyte at 13°C. ....	71
<b>Figure 4.12 :</b> The cross sectional SEM image of nanotubular structure formed on TiAl surface after 250 min anodic oxidation at 60 V in 0.25 wt % NH <sub>4</sub> F containing electrolyte at 21°C. ....	71
<b>Figure 4.13 :</b> The cross section SEM image of nanotubular structure formed on TiAl surface after 250 min anodic oxidation at 60 V in 0.25 wt % NH <sub>4</sub> F containing electrolyte at 29°C. ....	72
<b>Figure 4.14 :</b> The surface SEM image of nanotubular structure formed on TiAl surface after anodic oxidation at 60 V in 1.6 vol % water and 0.25 wt % NH <sub>4</sub> F containing electrolyte at 21°C. ....	73
<b>Figure 4.15 :</b> The cross sectional SEM image of nanotubular structure formed on TiAl surface after anodic oxidation at 60 V in 1.6 vol % water and 0.25 wt % NH <sub>4</sub> F containing electrolyte at 21°C. ....	73
<b>Figure 4.16 :</b> The cross sectional images of nanotubular structures with different lengths formed on TiAl coating in 1.6 vol % water and 0.25 wt % NH <sub>4</sub> F containing electrolyte at 60 V for a) 30 min b) 40 min c) 60 min d) 100 min e) 250 min f) 270 min. ....	74
<b>Figure 4.17 :</b> The relationship between anodization time and nanotube length grown in 1.6 vol % water and 0.25 wt % NH <sub>4</sub> F containing electrolyte at 60 V and 21°C. ....	75
<b>Figure 4.18 :</b> The surface SEM images of TiAl nanotubular structure formed on TiAl coated substrate after anodic oxidation at 60 V for 250 min in 0.7g NH <sub>4</sub> F containing electrolyte using Figure 4.18. The SEM images of nanotubular structures formed on TiAl coating in 1.6 vol % water and 0.25 wt % NH <sub>4</sub> F containing electrolyte at 60 V for and 21°C using a) magnetron stirring b) ultrasonic stirring. ....	75

<b>Figure 4.19 :</b> The nanotubular structure which was formed on Ti coated alumina substrate after anodization process that conducted at 40 V and 13 °C in 0.61 wt % NH <sub>4</sub> F consisting ethylene glycol for 40 min .....	76
<b>Figure 4.20 :</b> The surface SEM image of nanotubular structure formed on Ti coating after the anodization process done at 60 V and 13 °C in 0.25 wt % NH <sub>4</sub> F containing electrolyte for 250 min.....	77
<b>Figure 4.21 :</b> The cross sectional SEM image of nanotubular structure formed on Ti coating after it was anodized at 60 V and 13°C in 0.25 wt % NH <sub>4</sub> F containing electrolyte for 250 min. ....	77
<b>Figure 4.22 :</b> The SEM image of nanotubular structure formed on Ti coating after it was anodized at 60 V and 21°C in 0.25 wt % NH <sub>4</sub> F and 1.6 v % water containing electrolyte for 120 min. ....	78
<b>Figure 4.23 :</b> The cross sectional SEM image of nanotubular structure formed on Ti coating after it was anodized at 60 V and 21°C in 0.25 wt % NH <sub>4</sub> F and 1.6 v % water containing electrolyte for 120 min.....	78
<b>Figure 4.24 :</b> The surface SEM image of anodically oxidized TiAl coating deposited at -100 V bias and then subjected to high bias voltage post treatment. ....	79
<b>Figure 5.1 :</b> The GAXRD patterns of Ti and TiAl anodic oxides after the heat treatment at 280 °C. ....	83
<b>Figure 5.2 :</b> The GAXRD patterns of Ti and TiAl anodic oxides after heat treatment at 350 °C. ....	83
<b>Figure 5.3 :</b> The comparison of the GAXRD patterns of Ti and TiAl anodic oxides after heat treatment at 420 °C. ....	84
<b>Figure 5.4 :</b> The GAXRD patterns of Ti anodic oxide obtained after the heat treatments conducted at 420°C, 485°C, 550°C, 600°C and 650°C. ....	85
<b>Figure 5.5 :</b> The Raman spectra of Ti anodic oxide obtained after the heat treatments conducted at 420°C, 485°C, 550°C, 600°C and 650°C.....	85
<b>Figure 5.6 :</b> The PXRD patterns of Ti anodic oxide obtained after the heat treatments conducted at 350°C, 485°C and 600°C.....	86
<b>Figure 5.7 :</b> The GAXRD patterns of TiAl anodic oxide obtained after the heat treatments conducted at 420°C, 485°C, 550°C, 600°C and 650°C. ....	86
<b>Figure 5.8 :</b> The Raman spectra of TiAl anodic oxide obtained after the heat treatments conducted at 420°C, 485°C, 550°C, 600°C and 650°C. ....	87
<b>Figure 5.9 :</b> The PXRD patterns of TiAl anodic oxide obtained after the heat treatments conducted at 485°C, 550°C and 600°C.....	88
<b>Figure 5.10 :</b> The comparison of PXRD patterns of Ti and TiAl anodic oxides in the presence of metallic film underneath the nanotube layer which were obtained after the heat treatment at 720°C.....	89
<b>Figure 5.11 :</b> The comparison of GAXRD patterns of Ti and TiAl anodic oxides in the presence of metallic film underneath the nanotube layer which were obtained after the heat treatment at 720°C.....	89
<b>Figure 5.12 :</b> The comparison of Raman spectra of Ti and TiAl anodic oxides in the presence of metallic film underneath the nanotube layer after the heat treatment at 720 °C. ....	90
<b>Figure 5.13 :</b> The PXRD pattern of TiAl anodic oxide in the absence of metallic film underneath the nanotube layer which were obtained after the heat treatment at 720°C. ....	90

<b>Figure 5.14 :</b> The GAXRD pattern of TiAl anodic oxide in the absence of metallic film underneath the nanotube layer which were obtained after the heat treatment at 720°C. ....	91
<b>Figure 5.15 :</b> The shifts in TiO <sub>2</sub> anatase peak positions after the heat treatment of TiAl anodic oxide at 600°C. ....	93
<b>Figure 5.16 :</b> The observed shifts in TiO <sub>2</sub> anatase peak positions after the heat treatment of TiAl anodic oxide at 600°C in high magnification.....	94
<b>Figure 5.17 :</b> The comparison of original TiO <sub>2</sub> anatase peak positions and the calculated TiO <sub>2</sub> anatase peak positions if “c” parameter is taken 10% less than the original values. ....	94
<b>Figure 5.18 :</b> The comparison of GAXRD pattern of heat treated TiAl anodic oxide and the simulated pattern .....	95
<b>Figure 5.19 :</b> The peak fitting for the calculation of the crystallite size of Ti anodic oxide which was heat treated at 600°C. ....	97
<b>Figure 5.20 :</b> The peak fitting for the calculation of the crystallite size of TiAl anodic oxide which was heat treated at 600°C. ....	97
<b>Figure 6.1 :</b> The surface SEM image of nanotubular structure formed on TiAl surface after anodic oxidation at 60 V in 1.6 vol % water and 0.25 wt % NH <sub>4</sub> F containing electrolyte at 21°C. ....	99
<b>Figure 6.2 :</b> The cross sectional SEM image of nanotubular structure formed on TiAl surface after anodic oxidation at 60 V in 1.6 vol % water and 0.25 wt % NH <sub>4</sub> F containing electrolyte at 21°C. ....	100
<b>Figure 6.3 :</b> The image of the fabricated nanotubular TiAl oxide sensor after placing the Pt electrodes on the surface.....	101
<b>Figure 6.4 :</b> The response graph of the nanotubular TiAl anodic oxide against different H <sub>2</sub> concentrations at 100°C. ....	104
<b>Figure 6.5 :</b> The response graph of the nanotubular TiAl anodic oxide against different H <sub>2</sub> concentrations at 250°C. ....	105
<b>Figure 6.6 :</b> The response graph of the nanotubular TiAl anodic oxide against different H <sub>2</sub> concentrations at 300°C. ....	105
<b>Figure 6.7 :</b> The temperature dependence of sensor sensitivity upon exposure to 2500ppm hydrogen. ....	107
<b>Figure 6.8 :</b> The interactions between the surface and the gas phase depends on temperature .....	108
<b>Figure A.1 :</b> The response graph of the nanotubular TiAl anodic oxide against different H <sub>2</sub> concentrations at room temperature. ....	126
<b>Figure A.2 :</b> The response graph of the nanotubular TiAl anodic oxide against different H <sub>2</sub> concentrations at 200°C. ....	126
<b>Figure A.3 :</b> The response graph of the nanotubular TiAl anodic oxide against different H <sub>2</sub> concentrations at 350°C. ....	127



## **FABRICATION AND CHARACTERIZATION OF NANOTUBULAR Ti AND TiAl ANODIC OXIDE FILMS FOR GAS SENSING APPLICATION**

### **SUMMARY**

Gas sensors are extensively used for effective detection and control of industrial and automotive exhaust emissions that mainly consists of CO<sub>2</sub>, CO, H<sub>2</sub>, NO<sub>x</sub>. The concentration measurement of these emissions is important for human health, ecological balance, industrial safety and efficiency. Selectivity, sensitivity, long term stability, response and recovery time are the most significant properties of gas sensors. These properties govern the effectivity on functionality, performance and cost of sensors. Industrialization and technological advancements forces the development of fast responding better sensors with higher selectivity. Hence, there has been on going research and development efforts in this field.

Semiconductor oxide based sensors, known also as chemiresistive sensors, are the most investigated and widely used ones for detection of combustible and toxic gases. These sensors are advantageous due to their high sensitivity to exhaust gases, low cost and relative simplicity. Since hydrogen interacts with the other reducing gases in a gas mixture consisting of CO<sub>2</sub>, CO, H<sub>2</sub>, sensors with high selectivity and sensitivity properties is required for effective hydrogen sensing. However, available sensors are still not sufficient to succeed this task and development of highly sensitive hydrogen gas sensors using semiconductor oxide based sensor materials is still a challenge. TiO<sub>2</sub> has gained much attention among semiconductor oxide based sensor materials, owing to its high stability at elevated temperatures and in harsh environments, low cost, non-toxic properties. TiO<sub>2</sub> is one the most promising sensor material for development of highly selective hydrogen sensors. The possibility of oxidizing and nanotubular structure formation of metallic titanium with electrolytic processess opened up new horizons for increasing the sensing and selectivity characteristics of titania based gas sensors.

In production and applications of sensor platforms of functional sensor devices that are used in harsh environments the sensor material is generally deposited on ceramic substrates. In literature, RF sputtering and e-beam evaporation PVD are two commonly used techniques to deposit TiO<sub>2</sub> or metallic Ti thin films on different substrates. However, there are some problems in thin film coatings produced via these techniques. The most important bottleneck of these techniques is their inability to produce coatings that are well-adherent, dense and resistant to electrolytic process.

In the present study, the well-adherent, dense metallic Ti and TiAl thin films were deposited on alumina substrates using CAPVD method. This has been accomplished for the first time in this study. The pretreatment process applied before deposition generated heat on the surface of substrates by the effect of energetic ions and this

heating provided good adhesion between substrate and coating. The main effects of different bias voltage on the resulting coating structures and morphologies were investigated. As the deposition bias voltage was increased, the columnar structure of coatings became denser and this resulted in a decrease in Ti and TiAl coating thicknesses. The aluminum content of the films showed dependence on the bias voltage. The high bias voltage applied during post treatment caused a heating on the surface of coatings. Post treatment of the coating resulted in the densification of the coating structure. The columnar structure of coatings was converted into equiaxed structure by the effect of post treatment with high bias voltage. Surface morphologies of coatings were improved compared to the coatings without post treatment and smoother surfaces were obtained. The rapid heat treatment supplied by the application of high bias voltage led to stabilize the meta-stable  $\text{Ti}_3\text{Al}$  phase in TiAl coatings and the amount of this phase increased with the aluminum content.

All the coatings produced by CAPVD method were anodized in ethylene glycol electrolyte without any spalling. This result shows that CAPVD is a suitable method for producing well-adherent coatings which are resistant to electrolytic processes. Among the coatings produced, two types of Ti and TiAl coatings were selected for the optimization of anodization studies. These are the coatings produced at -100 V bias voltage with and without high bias voltage post treatment. The suitability and durability of these two different Ti and TiAl coating structures were tested for anodization process and the possible effects of post treatment on as grown nanoporous structure were investigated. Both these two different coating structures promoted the formation of highly ordered nanoporous-nanotubular structures on their surfaces. In post treated coatings crack formation induced by internal stresses was observed on the surface of anodized structures. Therefore, the coatings produced without post treatment was selected as the most appropriate coating structures for anodization process. The optimization studies are mainly conducted by using TiAl alloy coatings since there are no studies about the anodization of these coatings in the literature. In anodization of both Ti and TiAl thin film coatings, various anodization voltages, electrolyte compositions, temperatures, agitation types and durations were performed. The effects of these parameters on the morphologies and diameters of as-grown nanotubes were also investigated and evaluated. The optimal anodization parameters for obtaining high thickness of nanotube layer and well-aligned nanotube arrays were determined. These produced nanotubes with high thickness are thought to be appropriate for using as a sensor material since there is a possibility to occur a short circuit between Pt circuits and the conductive layer underneath the nanotubes.

The crystallization behaviors of nanostructured Ti and TiAl anodic oxides were investigated after heat treatments conducted at different temperatures from 280 °C to 720 °C. The anatase-rutile phase transformation was observed at about 720 °C in nanostructured Ti anodic oxide. However, this phase transformation was kinetically hindered by the addition of Al dopant into  $\text{TiO}_2$  structure. It was found that the presence and absence of metallic layer underneath the nanotube has a considerable effect on the phase transformation. The presence of metallic film favors the anatase-rutile phase transformation in the nanotube structure. In Al-doped  $\text{TiO}_2$ , some of the peaks slightly shifted from  $\text{TiO}_2$  anatase peak positions due to the presence of smaller ionic radius of  $\text{Al}^{3+}$  ions in  $\text{TiO}_2$  lattice. It was determined that these peak shifts were observed in the planes which are mainly affected from the changes in c axis. The anatase  $\text{TiO}_2$  planes that are affected from “c” lattice parameter in TiAl

anodic oxides were determined and the peak positions were calculated using a simulation study. For heat treated TiAl anodic oxide, definitely smaller crystallite size was calculated compared to the heat treated Ti anodic oxide. The results of heat treatment investigations indicated that 3 parameters are mainly effective on anatase to rutile transformation. These are; rigid nanostructure form, the presence or absence of metallic film underneath the nanotubes and the addition of Al dopant.

The hydrogen sensing performance of nanotubular TiAl oxide sensor was investigated. The changes in sensor resistance were measured at various hydrogen gas concentrations and operating temperatures. The produced nanotubular TiAl oxide sensor exhibited good responses towards H<sub>2</sub> gas concentrations at all operating temperatures, however, the optimum operating temperature for maximum sensor response was determined as 300 °C since high sensitivity with lower response and recovery times were obtained at this temperature. The prepared sensor is also sensitive to gas concentration and it can detect even lower concentrations (50 ppm) of H<sub>2</sub> gas. It can be concluded that the electrical resistance of TiO<sub>2</sub> decreased to lower values by using Al dopant and the electrical conductivity provided by Al doping caused an increase in the sensor stability and sensitivity.



# **TİTANYA ESASLI NANOTÜPLÜ İNCE FİLM HİDROJEN GAZ SENSÖRLERİNİN ÜRETİMİ VE KARAKTERİZASYONU**

## **ÖZET**

Endüstriyel ve araç egzoz kirliliklerini kontrol etmek amacı ile ortamdaki CO<sub>2</sub>, CO, H<sub>2</sub>, NO<sub>x</sub>, gibi zararlı egzoz gaz emisyonlarının tayin edilmesi ve konsantrasyonlarının sensör sistemleri ile ölçülmesi, insan sağlığı, ekolojik denge, iş yeri güvenliği ve yanma performanslarının tanımlanması açısından çok önemlidir. Sensörlerin maliyet, performans ve işlevsellikleri üzerinde en etkili parametreler sensörün seçiciliği ve duyarlılığı, uzun süreli kararlılığı, yanıt verme ve toparlanma süreleridir. Teknolojik gelişmeler ile birlikte gerekliliği artan sensörlerin bu özelliklerinin geliştirilmesi konusu uzun yıllardır üzerinde çalışılan ve yeni gelişmelerin sık sık ortaya konduğu bir çalışma alanıdır.

Egzoz gaz emisyonlarına en duyarlı sensör çeşidi yarı iletken oksit tabanlı sensörleridir (kemiresistif sensörler). Hidrojen diğer egzoz gaz emisyonları ile birlikte bulunduğu ortamda, redükleyici gazlar ile girişim yapabilmektedir ve bu yüzden bu tür gazları algılamada ayrı ayrı seçiciliği ve duyarlılığı yüksek olan sensörlerin kullanılması gereklidir ancak mevcut sensörler ile bu henüz sağlıklı olarak başarılamamaktadır. Yarı iletken sensör malzemesi olarak TiO<sub>2</sub> yüksek sıcaklıktaki termal kararlılığı, zor çevre şartlarına toleransı, düşük maliyeti ile ve bilinen toksik bir özelliği olmamasından dolayı günümüzde yanma ve egzoz gazı emisyonlarını tayin etmede ve bu emisyonlardaki hidrojene karşı seçiciliği arttırılmış sensörlerde önemli bir algılayıcı malzeme haline gelmiştir. Bu yapıların daha sonra uygulanan elektrolitik proseslerle hem oksitlenebilme hem de nanotüpler halinde oluşturabilme özelliğinde olması da hem duyarlılıklarının hem de seçiciliklerinin arttırılması açısından yeni ufuklar açmaktadır.

TiO<sub>2</sub> tabanlı sensör malzemesinin seramik karakterli bir altlık üzerinde üretilmesi bu sensör malzemesinin değişik uygulamalarda kullanılan ve farklı gereksinimlere ihtiyaç duyan cihazlarda kullanılabilmesine olanak sağlamaktadır. TiO<sub>2</sub> ince filmini veya metalik Ti ince filmini bir altlık üzerinde üretme aşamasında literatürde en çok kullanılan 2 yöntem manyetik alanda sıçratma ve e-demeti buharlaştırma FBB teknikleridir. Ancak bu konudaki en büyük sıkıntı bu teknikler ile altlık malzeme yüzeyine iyi yapışan, yoğun, aynı zamanda daha sonra uygulanan elektrolitik işleme dayanıklı kaplamaların üretilmemesidir.

Bu çalışmada katodik ark tekniği ile altlık malzemeye çok iyi yapışan, yoğun, eş eksenli ve anodizasyon esnasında kullanılan elektrolite dayanıklı metalik Ti ve TiAl ince filmler üretilmiştir. Bu çalışmada kullanılan katodik ark kaplama ve alaşımlandırma yaklaşımı titanyum tabanlı sensör malzemesi üretiminde ilk defa bu çalışma kapsamında kullanılmıştır. Kaplama işleminden önce altlık malzemeler ön işleme tabi tutulmuştur. Uygulanan bu ön işleme sırasında yüksek enerjili iyonların etkisi ile altlık malzemenin yüzey sıcaklığı artırılarak altlık malzeme ile kaplama

arasında iyi bir yapışma sağlanmıştır. Kaplama bias voltajının üretilen kaplama morfolojisi ve mikroyapısal özellikleri üzerindeki etkileri incelenmiştir. Kaplama bias voltajı arttıkça daha yoğun yapıda kaplamalar elde edildiği için Ti ve TiAl kaplamaların kalınlıklarında azalma gözlenmiştir. TiAl kaplamalarda Al içeriği bias voltajına bağlı olarak değişim göstermiştir. Bazı kaplamalara, kaplama sonrasında yüksek bias voltajı uygulanmış ve bu işlemin üretilen kaplamalar üzerindeki etkileri incelenmiştir. Uygulanan yüksek bias voltajı kaplama yüzey sıcaklığının artmasını sağlamıştır. Bu işlem uygulandığında, daha yoğun kaplama yapısı elde edilmekle birlikte kaplamanın kolonsal yapısı eşeksensli bir yapıya dönüşmektedir. Ayrıca bu işlem sayesinde kaplamaların yüzey morfolojilerinde farkedilir derecede iyileşme gözlenmiştir. TiAl kaplamalarda, kaplama sonrası uygulanan yüksek bias voltajı hızlı bir ısıtıl işlem etkisi yarattığı için Al miktarının fazla olduğu kaplamalarda yarı kararlı  $Ti_3Al$  fazının kararlı hale gelmiştir. Katodik ark metodu ile üretilen tüm kaplamalar yüzeylerinde dökülme olmaksızın anodize edilebilmiştir. Bu sonuç, katodik ark yönteminin, elektrolitik proseslere dayanıklı kaplamaların üretiminde kullanılmaya elverişli bir metot olduğunu göstermiştir. Yapılan anodizasyon işlemi ile üretilen kaplamaların hem oksit formuna dönüştürülmesi hem de yüzeyinde gaz algılama özelliğini fark edilir derecede arttıracak nanotüplerden oluşan genişletilmiş bir yüzey elde edilmesi sağlanmıştır.

Anodizasyon optimizasyon çalışmalarında kullanılmak üzere iki farklı Ti ve TiAl kaplama türü seçilmiştir. Bunlar; -100 bias voltajında üretilmiş kaplamalar ve yine aynı bias voltajında üretildikten sonra yüksek bias voltajına maruz bırakılmış kaplamalardır. Bu iki farklı Ti ve TiAl kaplama yapılarının anodizasyon prosesi açısından uygunluğu ve dayanıklılığı test edilmiştir. Ayrıca uygulanan yüksek bias uygulamasının elde edilen nanoyapılar üzerindeki olası etkileri incelenmiştir. Her iki farklı kaplama yapısı da düzenli dizilime sahip nanogözenekli ve nanotübüler yapıların oluşmasını sağlamıştır. Ancak yüksek bias uygulanmış kaplamalarda iç gerilme oluşmasında dolayı anodize edilmiş yüzeylerde çatlaklar gözlenmiştir. Bu yüzden, anodizasyon prosesi için yüksek bias uygulanmamış kaplamaların kullanılmasının daha uygun olacağı düşünülmüştür. Literatürde TiAl alaşım kaplamaların anodizasyonu ile ilgili çalışma olmadığı için daha çok TiAl kaplamalarının anodizasyon parametrelerinin optimizasyonu üzerinde yoğunlaşmıştır. Ti ve TiAl ince film kaplamaların anodizasyon parametrelerinin optimizasyon çalışmalarında, anodizasyon voltajının, elektrolit konsantrasyonun, anodizasyon sıcaklığının, karıştırma türünün ve anodizasyon sürelerinin üretilen nanoyapıların üzerindeki etkileri incelenmiştir. Düzenli dizilime sahip nanotüp yapıları ile uzun nanotüp yapıları içeren anodik oksitler elde etmek için gerekli optimum anodizasyon parametreleri belirlenmiştir. Uzun nanotüp yapısına sahip anodik oksitler sensör malzemesi olarak kullanıldığında, platin elektrotlar ile nanotüplü yapının altında kalan metalik film arasında oluşabilecek kısa devrenin oluşmasını engellemektedir.

Nanoyüzeyli Ti ve TiAl anodik oksitlerin kristalizasyon davranışları, ısıtıl işlemler sonrasında yapılan faz analiz çalışmaları ile belirlenmiştir. Isıtıl işlemler 280 °C ile 720 °C arasında sistematik olarak gerçekleştirilmiştir. Nanoyüzeyli Ti anodik oksitlerde anatas-rutil faz dönüşümü 720 °C civarında görülmüştür. Ancak, TiAl anodik oksitlerde anatas-rutil dönüşümü Al dopantının katkısından dolayı kinetik olarak geciktirilmiştir. Anodik oksit yapısında nanotüplerin altında oksitlenmemiş metalik filmin varlığının da faz dönüşümü üzerinde önemli etkisi olduğu tespit

edilmiştir. Isıl işlem uygulanmış TiAl anodik oksitlerde, bazı anatas pik pozisyonlarında kaymalar görülmüştür. Titanyuma kıyasla daha küçük iyonik yarıçapa sahip alüminyum iyonun anatas kristal yapısına girerek düzlemler arası mesafenin azalmasına ve dolayısı ile anatas pik pozisyonlarının daha yüksek açılara doğru kaymasına neden olmuştur. Pik pozisyonlarında kayma görülen düzlemlerin “c” kafes parametresindeki değişimlerden etkilenen düzlemler olduğu yapılan simulasyon çalışmaları neticesinde belirlenmiştir. Tane boyutu hesaplamaları neticesinde, ısıtma işlemi uygulanmış TiAl anodik oksitlerin nispeten daha küçük tane boyutuna sahip olduğu görülmüştür. Tüm yapılan ısıtma işlem çalışmaları sonucunda, anatas-rutil faz dönüşümü üzerinde genel olarak 3 parametrenin etkili olduğu düşünülmüştür. Bunlar; yapının nanoboyutta oluşu, nanotüp yapısının altında metalik filmin varlığı ve Al ile katkılandırılmasıdır.

Son olarak, üretilen nanoyüzeyli TiAl oksitler sensör malzemesi olarak kullanılmıştır. Bu malzemelerin hidrojen algılama özellikleri farklı sıcaklıklarda ve farklı hidrojen gaz konsantrasyonunda test edilmiştir. Al katkısı sensörün başlangıç direnç değerini Ti oksit sensörlere kıyasla azaltarak sensörün algılama özelliklerini iyileştirmiş ve konsantrasyona bağlı ölçümlerde sensörün kullanılmasına olanak sağlamıştır. 100°C üzerinde yapılan sensör testlerinde, hidrojenin kimyasal adsorpsiyonu için gerekli aktivasyon enerjisi sağlandığı için sensörün hidrojene karşı duyarlılığında artış meydana gelmiştir. Duyarlılık 100 °C ile 200 °C arasında hızlı bir artış gösterir iken, 200°C ile 350° C arasında duyarlılık artış hızı yavaşlamaya ve belli bir limit değere ulaşmaya başlamıştır. Hidrojen atomlarının sensör yüzeyine kimyasal olarak adsorpsiyonun tek katman halinde gerçekleştiği için sensörün bu şekilde bir davranış gösterdiği düşünülmüştür. Üretilen sensör, genişletilmiş yüzey alanına ve yüksek yüzey/hacim oranına sahip olduğu için, oda sıcaklığında ve 100°C’de yapılan testlerde de tüm hidrojen konsantrasyonlarını algılayabilmiştir ancak duyarlılık değerleri yüksek sıcaklıklarda elde edilen değerler kadar yüksek değildir. Nanoyüzeyli TiAl oksit sensörün hidrojen gaz konsantrasyonundaki değişimlere duyarlı olduğu ve 50 ppm kadar düşük konsantrasyonlardaki hidrojen gazını bile algılayabildiği tespit edilmiştir. Test sıcaklığının artması ile diğer sensör parametrelerinde de iyileşme gözlemlenmiştir. 200°C’nin üzerinde yapılan testlerde, hesaplanan cevap süreleri 30-100 saniye ve toparlanma süreleri 3-10 saniye aralığında değişim göstermektedir. Üretilen nanoyüzeyli TiAl oksit sensör için optimum çalışma sıcaklığı ise 300°C olarak belirlenmiştir.





## 1. INTRODUCTION

### 1.1 Gas Sensors and Their Operating Principles

The gas sensor is designed to convert a chemical information (concentration) of a particular gas in the ambient into an electrical signal. The main components of gas sensor are receptor and transducer. Some interactions such as adsorption, electrochemical reactions etc occur between gas molecules and a material acting as a receptor and these interactions create some physical or chemical effects (formation of reaction products or reaction heat, change in mass, size or surface properties of receptors) on receptors. The transducer converts these effects to an electrical signal. While the diagnosis of gas is a chemical based process, conversion of a chemical information of a gas to an electrical signal is physical based process (Figure 1.1).

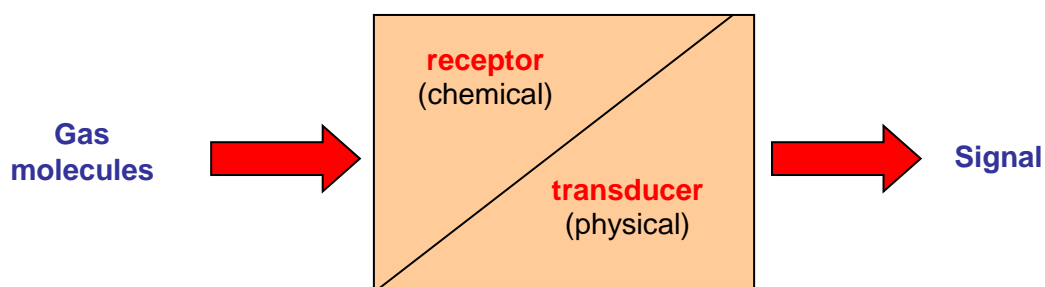


**Figure 1.1 :** Operation principle of gas sensor [1].

### 1.2 Types of Gas Sensors

Semiconductors, ionic conductors (solid electrolytes), piezoelectric crystals, catalytic combustion catalysts, optic fibers and many other functional materials have been used in gas sensor fabrication [1].

There are different types of gas sensors such as solid state sensors, mass and optical sensitive sensors. Table 1.1 presents different types of gas sensors and their detection principles. Among these sensors, according to their detection principles solid-state sensors can be classified as follows; chemiresistive, chemical field effect transistor, calorimetric, potentiometric, amperometric sensors.

In this thesis, chemiresistive type gas sensor has been fabricated. In these sensors, the resistance change in semiconductor oxide sensor material is measured during the analyte gas interact with the semiconductor oxide sensor material [1,2].

**Table 1.1** : A list of gas sensors and their detection principles [1].

Type of Sensor	Gas Sensor	Detection Principle
Solid State Sensors	Chemiresistive	A change in conductivity of semiconductor is measured when it interacts with the analyzing gas.
	Chemical field effect transistors (chemFET)	Current-Voltage (I-V) curves of a field effect transistor are sensitive to a gas when it interacts with gate.
	Calorimetric	The concentration of combustible gas is measured by detecting the temperature rise resulting from the oxidation process on a catalytic element.
	Potentiometric	The signal is measured as the potential difference (voltage) between the working electrode and the reference electrode. The working electrode's potential must depend on the concentration of the analyte in the gas phase.
	Amperometric	Diffusion limited current of an ionic conductor is proportional to the gas concentration.
Mass Sensitive Sensors	Acoustic	Change in frequency of surface-acoustic waves excited on a quartz or piezoelectric substrate upon adsorption or absorption of gas in a suitable sorption layer (e.g. metals, polymers).
	Microelectromechanical systems based sensors	Change in mechanical bending of micro or nanocantilevers upon adsorption of gas.
Optical Sensors	Surface Plasmon Resonance	Change in surface plasmon resonance signals is proportional to the refractive index close to the sensor surface and, is therefore, related to the amount of bound gas molecules.
	Optodes	The change of optical properties measured can base on absorbance, reflectance, luminescence, light polarization, Raman and others.

### 1.3 Semiconductor Based Chemiresistive Sensors

Semiconductor based chemiresistive sensors are sensitive to atmospheric polluting gases [3,4]. This sensor type is frequently used in determination of exhaust gas emission due their low-cost, small size and relatively simple to use. Chemiresistive materials include metal oxide and non-oxides (such as carbon nanotubes, polymers). Some of the chemiresistive materials are given in a representative list in Table 1.2. Among these chemiresistive materials, semiconductor metal oxides are mostly used

as chemiresistive sensor materials [1]. Semiconductive metal oxides have potential interest in gas sensor applications due their higher reactivity against the surrounding gas atmosphere [5].

**Table 1.2 :** The representative list of some of the chemiresistive materials [1].

<b>Chemiresistive Materials</b>	<b>Base Material</b>	<b>Additives</b>	<b>Analyzing Gas</b>
Metal-oxides	Al <sub>2</sub> O <sub>3</sub>	Al, SiO <sub>2</sub> /Si	Humidity, CH <sub>4</sub> , NH <sub>3</sub>
	Bi <sub>2</sub> O <sub>3</sub>	Sb <sub>2</sub> O <sub>3</sub>	Smoke, CO, NO
	CdO	ZnFe <sub>2</sub> O <sub>4</sub>	Ethanol
	CeO <sub>2</sub>	SnO <sub>2</sub>	O <sub>2</sub> , H <sub>2</sub> S
	Cr <sub>2</sub> O <sub>3</sub>	TiO <sub>2</sub>	NO <sub>2</sub> , O <sub>2</sub> , NH <sub>3</sub> , Humidity
	Co <sub>3</sub> O <sub>4</sub>	SiO <sub>2</sub>	NH <sub>3</sub> , CO, CH <sub>4</sub> , C <sub>3</sub> H <sub>8</sub> , H <sub>2</sub> , NO <sub>2</sub> , Cl <sub>2</sub>
	CuO	SnO <sub>2</sub>	CO, ethanol, H <sub>2</sub> S
	Fe <sub>2</sub> O <sub>3</sub>	Au, Zn (Pt, Pd, RuO <sub>2</sub> )	Methane, propane, Benzene, Toluene CO, NO <sub>2</sub> , Methanol, Acetone
	Ga <sub>2</sub> O <sub>3</sub>	SnO <sub>2</sub> , Pd, Ta <sub>2</sub> O <sub>5</sub> , WO <sub>3</sub> , NiO	O <sub>2</sub> , CO, CH <sub>4</sub> , NO, NH <sub>3</sub>
	In <sub>2</sub> O <sub>3</sub>	MoO <sub>3</sub> , Au, Al, SnO <sub>2</sub>	O <sub>3</sub> , NO <sub>2</sub> , H <sub>2</sub> , CO, C <sub>3</sub> H <sub>8</sub> , H <sub>2</sub> S, Cl <sub>2</sub> , CO <sub>2</sub> , SO <sub>2</sub> , NH <sub>3</sub> , ethanol, acetone
	MoO <sub>3</sub>	Ti	NH <sub>3</sub> , CO, NO <sub>2</sub>
	Nb <sub>2</sub> O <sub>5</sub>	SnO <sub>2</sub>	NH <sub>3</sub> , CO, C <sub>2</sub> H <sub>5</sub> OH, H <sub>2</sub>
	NiO	Li, TiO <sub>x</sub>	H <sub>2</sub> , HCHO, CH <sub>4</sub> , CH <sub>3</sub> COOH, CO, NO <sub>2</sub>
	Ta <sub>2</sub> O <sub>5</sub>	-	Humidity
	SnO <sub>2</sub>	Pt, Ag, Pd, Os, Fe, Au, In, Ru, Bi <sub>2</sub> O <sub>3</sub> , CeO <sub>2</sub> , CuO	CO, CH <sub>4</sub> , SO <sub>2</sub> , N <sub>2</sub> O, CO <sub>2</sub> , NO <sub>2</sub> , CH <sub>3</sub> OH, C <sub>2</sub> H <sub>5</sub> OH, C <sub>3</sub> H <sub>8</sub> , H <sub>2</sub> , LPG, H <sub>2</sub> S, NH <sub>3</sub> , C <sub>n</sub> H <sub>2n+2</sub>
	TiO <sub>2</sub>	La, Pt, Cr <sub>2</sub> O <sub>3</sub> , WO <sub>3</sub>	CH <sub>3</sub> OH, C <sub>2</sub> H <sub>5</sub> OH, C <sub>3</sub> H <sub>7</sub> OH, O <sub>2</sub> , H <sub>2</sub> , NH <sub>3</sub> , NO <sub>2</sub>
	WO <sub>3</sub>	Mg, Zn, Mo, Re, Au, Pd	NO <sub>2</sub> , NH <sub>3</sub> , H <sub>2</sub> S, O <sub>2</sub>
	V <sub>2</sub> O <sub>5</sub>	Fe <sub>2</sub> O <sub>3</sub> , SnO <sub>2</sub> , TiO <sub>2</sub>	NO <sub>2</sub> , NH <sub>3</sub> , C <sub>2</sub> H <sub>5</sub> OH, Butylamines, Propanol, Toluene
	ZnO	Al, Sn, Cu, Pd, Fe <sub>2</sub> O <sub>3</sub>	NH <sub>3</sub> , H <sub>2</sub> , NO <sub>2</sub> , LPG, CH <sub>4</sub> , CO, H <sub>2</sub> S, CH <sub>3</sub> OH, C <sub>2</sub> H <sub>5</sub> OH, C <sub>3</sub> H <sub>7</sub> OH
Non-oxides	Te	Nil	H <sub>2</sub> S, NH <sub>3</sub> , CO, NO <sub>2</sub>
	Porous-Si	Nil	Humidity, NO <sub>2</sub>
	CuBr	Nil	NH <sub>3</sub>
	Carbon Nanotube		
	Polymers		

### 1.3.1 The characteristics of semiconductor based chemiresistive sensors

The electrical resistance of chemiresistive sensors can be decreased or increased depending on the analyte gas molecules. The increase or decrease in resistance depends on the type of sensor material (n or p type semiconductor) and analyte gas

(reductant or oxidant) [1]. In semiconductive metal oxides, the surface of oxide is receptor, grain boundaries are transducer and the change in resistance is signal. Transducer converts the change in work function of grains into electrical resistance. For this reason, grain size, surface properties, the kinetic factor determined by diffusion and surface reactions are effective parameters in terms of gas sensor sensitivity [1,2]. In order to record the gas sensor response curve, the resistance of sensor element is measured by a multimeter or electrometer. The resistance measurement is performed first in air (or only in the presence of carrier gas such as N<sub>2</sub>) and then in a certain amount of analyte gas mixed with carrier gas. Gases are fed to the sensor system with mass flow controllers. In addition, a heater can be used to increase the temperature of sensor element in sensor system since the sensing characteristics are a function of temperature. [1,2].

The response curve of a gas sensor which is schematically depicted in Figure 1.2 can be characterized by 5 parameters. These are [1]:

**a) Sensitivity (S):** Sensitivity is the ratio of resistivity in the air to the resistivity in the analyte gas. Sensitivity can be defined by two formulas:

**i)  $S = R_{\text{air}} / R_{\text{gas}}$**  (Higher S value for a particular gas indicates that the material is good for sensor fabrication.)

**ii)  $S (\%) = 100 \times (R_{\text{air}} / R_{\text{gas}}) / R_{\text{air}}$**  (Positive S value indicates that the resistivity of gas sensor exposed to analyte gas is decreased.)

**b) Response time:** The time interval that the resistivity of sensor reaches 90% of its constant value after the sensor is exposed to analyte gas concentration. The minimum response time is a good indication for gas sensor.

**c) Recovery time:** It is the time required for a sensor to switch back its resistance to the 10 % of the saturation value. If a sensor has a small recovery time, it can be used repeatedly.

**d) Selectivity:** It is defined as the ratio of sensitivity towards interfering gas to the sensitivity for desired gas.

**e) Long term stability:** The ability of the sensor to keep its properties constant when operated continuously for a long-term.

These 5 parameters are dependent on sensor material, the interaction between gas and sensor and operation conditions of sensor. In addition, since the adsorption and desorption of gas molecules are temperature dependent processes, the sensitivity, selectivity and response time are not dependent only the type of receptor, but also dependent on operation temperature. Moreover, the gas reactivity (rate constant) and its molecular weight affect the sensor response time. The rate constant ( $k$ ) determines the approximate temperature at which the sensor will operate effectively. In order to modify rate constant, foreign receptors (Pd) can be used [1].

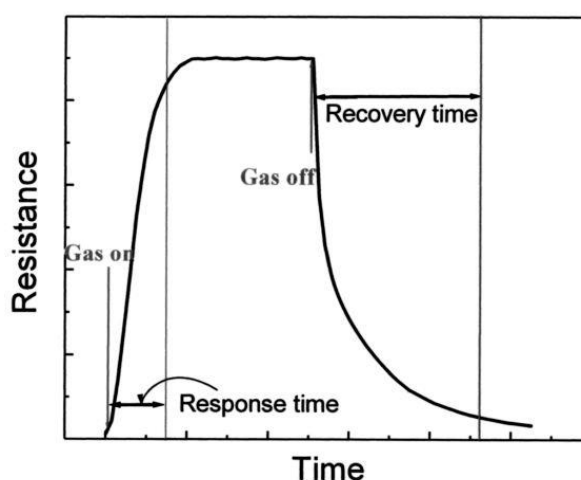


**Figure 1.2 :** The schematic representation of response curve of a chemiresistive sensors [1].

### 1.3.2 Problems associated with metal oxide sensors

Metal oxides have a lack of selectivity property and this constitutes a disadvantage for chemiresistor sensor. However, in order to increase the selectivity property of this type of sensors against target gases, suitable dopant elements (Pd, Pt, In, Cu, Nb, Mn), noble metals or transition metals, binary oxides, complex multi component oxides can be added to metal oxides or the operation temperature of sensor can be increased. Dopants are added for exhibiting catalyst effect in a selective reaction. By adding dopants to metal oxides, the charge carrier concentration, surface potential, barriers between crystals, chemical composition, phase composition and crystal size can be changed. Thus the surface reaction rates are increased and the selectivity of sensor material towards analyte gas types is provided. For instance,  $\text{TiO}_2$  is doped with  $\text{Cr}_2\text{O}_3$  to become sensitive to  $\text{NO}_2$  gas [1,2].

Metal oxide sensors used today are as follows: SnO<sub>2</sub>, TiO<sub>2</sub>, WO<sub>3</sub>, V<sub>2</sub>O<sub>5</sub>, ZnO, Al<sub>2</sub>O<sub>3</sub>, Bi<sub>2</sub>O<sub>3</sub>, CdO, CeO<sub>2</sub>, Cr<sub>2</sub>O<sub>3</sub>, CoO, Co<sub>3</sub>O<sub>4</sub>, CuO, FeO, Fe<sub>3</sub>O<sub>4</sub>, Fe<sub>2</sub>O<sub>3</sub>, Ga<sub>2</sub>O<sub>3</sub>, In<sub>2</sub>O<sub>3</sub>, MoO<sub>3</sub>, Nb<sub>2</sub>O<sub>5</sub>, NiO, Ta<sub>2</sub>O<sub>5</sub>. Among these semiconductor oxides, SnO<sub>2</sub>, TiO<sub>2</sub>, WO<sub>3</sub>, ZnO have been the most widely used ones in sensor applications [1,2].

## **1.4 TiO<sub>2</sub> Based Gas Sensors**

TiO<sub>2</sub> has many properties such as good optical properties, high photocatalytic activity, high oxidizing properties, etc. owing to these properties, TiO<sub>2</sub> has a wide range of application areas such as solar cells [6,7], lithium battery, photochromic switching [6], photovoltaic cell [8], photocatalytic areas [9,10,11]. Moreover, TiO<sub>2</sub> has high thermal stability at elevated temperature and thus it can exhibit high performance as a high temperature sensor material. Although SnO<sub>2</sub> based sensors are widely used in chemiresistive sensor applications, they show poor gas sensitivity above 250 °C. So TiO<sub>2</sub> can be utilized in high temperature sensor applications. TiO<sub>2</sub> has also high tolerance to harsh environment conditions, good catalytic activity, lack of toxicity and low cost. These properties provide TiO<sub>2</sub> to become an important sensor material to detect combustion and exhaust gas emissions and also hydrogen gas that interfere with other reductant gases existing in environment [11,12].

### **1.4.1 *n*-type and *p*-type behavior of TiO<sub>2</sub> based gas sensors**

*n*-type and *p*-type TiO<sub>2</sub> exhibit different behavior against oxidizing and reducing gases and therefore an increase or decrease in resistance can be observed depending on the type of TiO<sub>2</sub> sensor material. When *n*-type TiO<sub>2</sub> is exposed to oxidizing gas, the resistance increases due to the oxidizing gas that takes the electrons of *n*-type TiO<sub>2</sub>. On the contrary the resistance of *p*-type TiO<sub>2</sub> decreases. (since the condition is kept as follows;  $pn=\text{constant}$ , *n* decreases and *p* increases) In the case of exposure of reducing gases, *n*-type and *p*-type TiO<sub>2</sub> show exactly opposite response compared to oxidizing gases [13,14]. It is also possible to alter the electronic carrier from *p* type to *n* type. For instance, in the case of *p*-type doped TiO<sub>2</sub> with Nb (%10 at.), it was assumed that *n* decreased and *p* increased, however complicated behavior was observed in the slightly doped TiO<sub>2</sub> [13-15]. Sharma and his group reported that Cr-doped TiO<sub>2</sub> showed *n* to *p* type transition at higher oxygen partial pressures. At low oxygen partial pressure the material showed *n* type behavior and the resistivity of

sensor material was increased as the oxygen concentration increased. However, at higher oxygen pressure, the material acts as a p type material and the resistivity of sensor decreased. This result indicates that the oxygen molecule gets adsorbed on  $\text{TiO}_2$  surface and then it traps the electrons from the conduction band of  $\text{TiO}_2$ , thereby the conductivity of Cr-doped  $\text{TiO}_2$  is decreased. In the case of oxygen concentration is increased, the number of electrons in conduction band decreases further and conduction is governed by holes. Therefore, the Cr-doped  $\text{TiO}_2$  starts to behave as a p type material [13,15]. There are also other example of transition from n- to p-type behavior in Cr doped  $\text{TiO}_2$  [16]. In some studies, it was found that the metal oxide sensor material can exhibit n to p type transition depending on temperature and analyte gas concentration. For instance,  $\text{SnWO}_4$  material was tested against CO gas and a variation in resistances was observed in the tests that are conducted at 200 °C and 300°C. The same tendency was also observed in the material as the concentration of CO gas increased. All these variations in resistance arised from the n to p type transitions that occurred in the sensor material [17].

#### **1.4.2 Doped $\text{TiO}_2$ Based Gas Sensors**

$\text{TiO}_2$  is highly resistive n type semiconductor and due to its low conductivity it is generally adapted to analyze oxidant gases [18]. However,  $\text{TiO}_2$  has been frequently used as a reductant gas sensor material after differentiation of the microstructure and crystal phase, increasing the surface area, alloying or surface functionalization [1,12,19]. In order to improve the sensor properties of  $\text{TiO}_2$  based sensors, binary metal oxide semiconductor materials have been formed such as  $\text{TiO}_2\text{-MoO}_3$ ,  $\text{TiO}_2\text{-WO}_3$ ,  $\text{TiO}_2\text{-Cr}_2\text{O}_3$ ,  $\text{TiO}_2\text{-V}_2\text{O}_5$ ,  $\text{Ga}_2\text{O}_3\text{-TiO}_2$ ,  $\text{TiO}_2\text{-ErO}_3$ ,  $\text{TiO}_2\text{-Ta}_2\text{O}_5$  [20,21].

In literature, Cr [22-25] and Nb [12,26-28] dopants are added to  $\text{TiO}_2$  for CO,  $\text{O}_2$ ,  $\text{NO}_2$  sensitivity,  $\text{WO}_3$  [29-31] and V [3] dopants are added for  $\text{NO}_2$  gas sensitivity, Fe [32], Ta [33],  $\text{Y}_2\text{O}_3$  [32] are added for CO sensitivity,  $\text{NiO}_x$  is added for reducing gases at 300-400 °C [34], Al dopant is added for  $\text{O}_2$ , CO gas sensitivities [35] and  $\text{Al}_2\text{O}_3$  is added for  $\text{H}_2$  or  $\text{H}_2\text{S}$  gas sensitivities [36].

It should be pointed out that the content and the amount of these dopants constitute an importance for sensor material. In the case of altering the amount of dopant element, the sensitivity of sensor can be increased or decreased and the sensor may become sensitive to different gases.

### 1.4.3 The effects of adding dopant elements into TiO<sub>2</sub>

In order to improve the sensitivity of titania sensors, some dopants are added to titania such as Nb, Cr, Sn, Pt, Zn, Al, La, Y, etc. [35]. These dopants can be added to the titania lattice according to Hume-Rothery Rule and this rule indicates that metal ion dopants whose ionic radius are within 15% of that of the host lattice can show appreciable solubility [37]. Incorporation of dopants can reduce the band gap in TiO<sub>2</sub>, introduce mid-gap states and improve the charge carrier separation [37]. The most important effects of addition of dopant into titania are [35];

**-Delay in anatase-rutile transformation:** The anatase phase is more preferable in sensor applications owing to its higher electron mobility and sensitivity to reducing environment compared to rutile phase. Therefore, the retardation in anatase-rutile transformation can increase the sensitivity of gas sensor towards the analyte gas [38]. The effects of various cations on the phase transition temperatures in titania were shown in Figure 1.3.

**-Inhibition in grain growth:** The small grain structures create more active sites for the adsorption of gas molecules [27]. In addition, in the case of the diameter of grain is less or comparable than the space charge region, the sensitivity of gas sensor towards target gas is increased. When the grain size of titania is less than 80-100 nm, chemisorption becomes effective in these grain sizes and the sensing property of titania is increased. Therefore, the inhibition in grain growth can cause an increased the stability and the sensitivity of the sensing element [39].

**-An increase in conductivity:** The electrical conductivity provided by the dopant element can cause an increment in carrier concentration and thereby sensor stability and sensitivity can be improved.

### 1.4.4 The anatase-rutile phase transition temperatures of TiO<sub>2</sub>

The anatase-rutile transformation takes place in the temperature range 600-700°C; however, the reported temperatures for the transformation can vary from 400°C to 1200°C. The wide temperature range can arise from -the type and amount of additives, - impurities,- processing methods and conditions used in sample preparation, -the thermal treatment atmosphere and conditions, -the sample geometry (bulk, film, etc.) and use of different methods of determining the transition



temperatures [37,16,40-44]. Some of the reported anatase-rutile transition temperatures for titania depending on their process methods were summarized in Table 1.3. These parameters significantly affect and alter the transformation rate and activation energy. Therefore, anatase-rutile transformation occurs at a transition temperature either higher or lower than that of pure titania [43].

**Table 1.3 :** Some of the reported anatase-rutile transition temperatures for titania depending on their process methods [1].

Temperature (°C)	Fabrication Details
610	Highly pure powder
1190, 1138, 1115	Powders from three different suppliers
610	Commercially available reagent grade powder
390	Sol-gel synthesized powder
675	Sol-gel synthesized powder
787, 720	Sol-gel synthesized powder
465	4-6 nm particles prepared through a sol-gel method
616	Sol-gel synthesized powder
680, 600	Sol-gel synthesized powder
600	Sol-gel synthesized powder
700, 600	Sol-gel synthesized powder
600-700	Highly pure nanocrystals synthesized from $\text{TiCl}_4$ sol-gel
900	Sol-gel synthesized powder

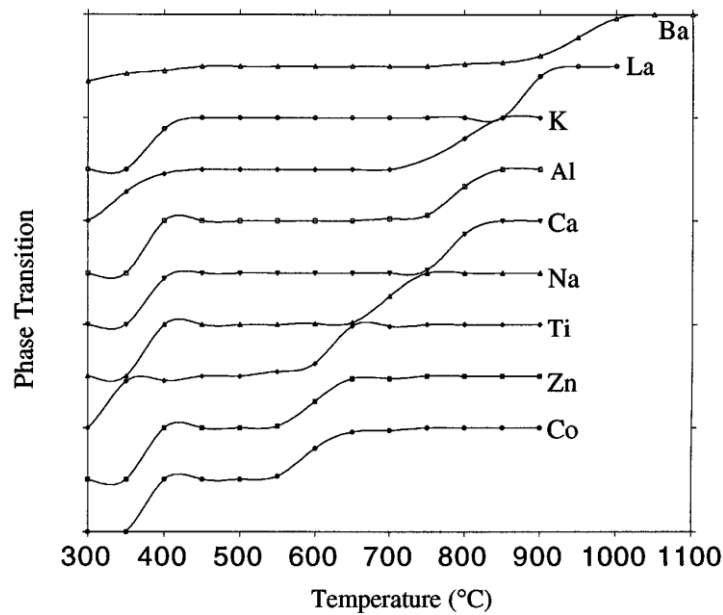


**Figure 1.3 :** The effects of various cations on the phase transition temperatures in titania [40].

### 1.4.5 The inhibiting and promoting dopants for TiO<sub>2</sub>

The dopant elements acting as an inhibitor in anatase-rutile phase transformation of TiO<sub>2</sub> were shown in periodic table given in Figure 1.4. These inhibiting and promoting dopant elements are also categorized depending on their ionic radius and valence in Figure 1.5.

Dopant experimentally observed to inhibit the transformation of anatase to rutile

Dopant experimentally observed to inhibit the phase transformation under certain conditions (mixed effect)

Dopant predicted to inhibit the transformation of anatase to rutile

H																	He
Li	Be											B	C	N	O	F	Ne
Na	Mg											Al	Si	P	S	Cl	Ar
K	Ca	Sc	Ti	V	Cr	Mn	Fe	Co	Ni	Cu	Zn	Ga	Ge	As	Se	Br	Kr
Rb	Sr	Y	Zr	Nb	Mo	Tc	Ru	Rh	Pd	Ag	Cd	In	Sn	Sb	Te	I	Xe
Cs	Ba	La	Hf	Ta	W	Re	Os	Ir	Pt	Au	Hg	Tl	Pb	Bi	Po	At	Rn
Fr	Ra	Ac	Rf	Db	Sg	Bh	Hs	Mt									
Ce	Pr	Nd	Pm	Sm	Eu	Gd	Tb	Dy	Ho	Er	Tm	Yb	Lu				
Th	Pa	U	Np	Pu	Am	Cm	Bk	Cf	Es	Fm	Md	No	Lr				

**Figure 1.4 :** Experimental and predicted inhibition of anatase to rutile transformation[37].

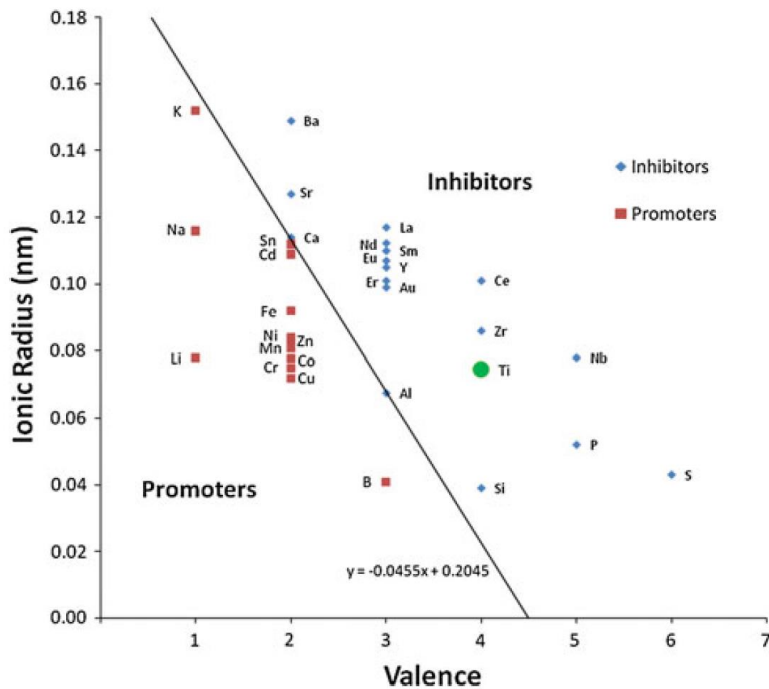


**Figure 1.5 :** The valence-radius plot of anatase to rutile transformation which is categorising inhibiting and promoting dopant elements [37].

#### **1.4.6 Modification of the anatase-rutile phase transition temperatures of TiO<sub>2</sub> with various dopant elements**

The ionic radius and the valence of dopant are the most important parameters that explain the change in anatase-rutile transformation temperature [40]. The relation established between anatase-rutile transition temperatures and ionic radius of dopant elements was shown in Figure 1.6. According to this graph;

-If the dopant size is smaller than titanium like Al, the presence of the dopant produces some empty space in the form of a lattice deformation; this deformation energy has to be released before the phase transition takes place. Thereby, the anatase phase is stabilized. The anatase phase is less stabilized when the size of the dopant is closer to the size of titanium

-If the dopant size is between titanium and oxygen, a parabolic correlation is occurred between the anatase-rutile phase transition temperature and the size of dopants. This dopant can be introduced substitutionally into the matrix, producing some deformation of the lattice structure; this deformation energy has to be released such that the anatase-rutile phase transition takes place, producing a stabilization of the anatase phase.

-If the dopant size is bigger than the oxygen, a large local lattice deformation is occurred. The anatase-rutile phase transition temperature is much smaller than those values that should be obtained if it would follow the same tendency as all the others.

Depending on the valence and ionic radius of the dopant ion, substitutional solid solution or interstitial solid solution can be formed. In literature, there are some assumptions about the resulting effects of substitutional or interstitial solid solution formation. These are;

**Substitutional solid solution formation;** The incorporation of dopant ions into the anatase lattice may either increase or decrease the level of oxygen vacancies through valence effects and thereby promote or inhibit the anatase-rutile transformation. If Ti<sup>4+</sup> ion substituted by a cation of low valence than 4, charge neutrality is required and thus the concentration of oxygen vacancies and/or the formation of Ti interstitials of lower valence are increased. The increase in the level of oxygen vacancies favors the anatase-rutile transformation. However, if the dopant cation has a valence higher than 4, the formation of Ti interstitials of the same or lower valence

is increased whereas the level of existing oxygen vacancies is decreased. This results in inhibiting the anatase-rutile transformation [37,43,44].

In literature, there are many controversial explanations on the anatase-rutile transformation mechanism showing that the process is complex and not fully understood yet [43]. For instance, although  $V^{5+}$  has a valence higher than 4, it accelerates the anatase-rutile transformation [44]. This contradicting and differing results may arise from the different production methods and conditions [44].

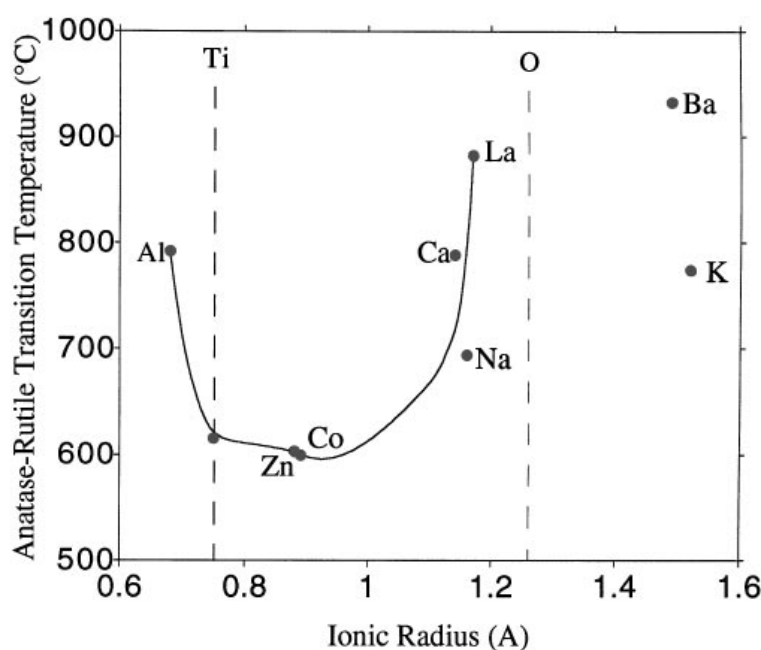


**Figure 1.6 :** The transition temperature of anatase-rutile is plotted as a function of the ionic radius of the dopants [40].

**Interstitial solid solution:** In this case, lattice constraint occurs and this may result in destabilisation or stabilisation of anatase phase, depending on size, valence, and content effects. The presence of interstitial ions in lattice has no apparent effect on the charge neutrality. In literature, it was reported that the presence of interstitial ions stabilize the titania lattice and consequently inhibit the rutile transformation. This assumption was supported by many findings and there is no report of destabilization (from structural instability) and consequent promotion of the transformation [37].

The amount of the dopant added to titania is also important as much as the ionic radius and the valence of the dopant. If the excess dopant is added to titania, phase transformation can be accelerated owing the lattice stress or the excess dopant can precipitate as a second heterogeneous phase [24,25,45,35].

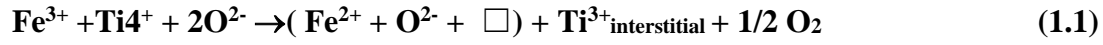
The reported effects of some dopant elements on TiO<sub>2</sub> structure and its anatase-rutile transformation were summarized below:

**Nb Dopant Element:** When certain amount of Nb<sup>5+</sup> is doped into titania, the ions can go into the lattice as substitutional metal dopant owing to their similar ionic sizes. The pentavalent Nb acts as an donor and it leads to decrease in the level of oxygen vacancies and thereby the phase transformation to rutile is hindered or delayed [25,46,38]. However, it was also assumed that the incorporation of Nb<sup>5+</sup> ions into TiO<sub>2</sub> structure interstitially causes a lattice stress due to the ionic size of Nb<sup>5+</sup> ions is slightly higher than Ti<sup>4+</sup> ions. This lattice stress gives rise to a hindering in the phase transformation to rutile [46,47]. Similar effects was observed in the case of Ta ions are incorporated to TiO<sub>2</sub> structure, whereas, Ga ions displayed opposite behavior in the same case [46].

**Cr Dopant Element:** The ionic size of Cr<sup>+3</sup> and Ti<sup>+4</sup> are very close to each other, therefore Cr<sup>+3</sup> may occupy the substitutional positions in TiO<sub>2</sub> lattice without affecting the the crystallography and an increase in the oxygen vacancy concentration in TiO<sub>2</sub> is expected. This might be the cause of accelaration of anatase-rutil transformation and the grain growth [15,47]. On the contrary, some conflicting assumptions about the consequent effect of Cr dopant in TiO<sub>2</sub> lattice were reported in literature. For instance, at lower Cr contents (5-10 at % Cr) TiO<sub>2</sub> rutile transformation is retarded up to 700 °C, however, the phase transformation can not be inhibited effectively at higher Cr contents (20-30 at % Cr) due to the increase in lattice stress [16]. Literature also proposed that the incorporation of certain amount of trivalent Cr dopant may inhibit the grain growth and delay the anatase-rutile transformation up to 900 °C [18].

Certain cationic dopants may exhibit more than one valence and this can result in; an increase in the level of oxygen vacancies and/or the formation of Ti<sup>3+</sup> interstitial. An increase in the concentration of oxygen vacancies favors the phase transformation through increase in lattice relaxation. On the other hand, the formation of Ti<sup>3+</sup> interstitial hinders the phase transformation through lattice constraint) [37]. In the case of TiO<sub>2</sub> which is doped with Fe<sub>2</sub>O<sub>3</sub> in reducing atmosphere it is assumed that Ti<sup>4+</sup> is substituted by Fe<sup>3+</sup> and the concentration of oxygen vacancies is increased according to following reaction (1.1). This result arises from three potential mechanism [37]:

- (1) the maintenance of charge balance;
- (2) spontaneous reduction  $\text{Fe}_2\text{O}_3$  to  $\text{Fe}_3\text{O}_4$  or  $\text{FeO}$
- (3) reduction of  $\text{TiO}_2$  to  $\text{TiO}_{2-x}$



( $\square$  denotes an oxygen vacancy) [37].

The increment in the level of oxygen vacancy by the reduction of  $\text{Fe}^{+3}$  promotes the  $\text{TiO}_2$  rutile phase transformation. In the case of  $\text{MnO}_2$  is used as a dopant, it is thought that doping  $\text{MnO}_2$  has no effect on creating oxygen vacancies. However,  $\text{MnO}_2$  exhibits similar behavior as  $\text{Fe}_2\text{O}_3$  since  $\text{Mn}^{4+}$  is reduced to  $\text{Mn}^{3+}$  and  $\text{Mn}^{2+}$  spontaneously in air ambient [37].

#### 1.4.7 The effects of adding Al dopant on gas sensing properties of $\text{TiO}_2$ based gas sensors

The addition of certain amount of Al dopant to titania can cause changes in its microstructural and electrical properties. Literature reported that the presence of suitable amount of Al dopant ion in titania can retard the anatase-rutile phase transformation and inhibit the grain growth [35,48-53].

In literature, 5 wt%  $\text{Al}_2\text{O}_3$  (with 0.5 wt % Pd) was incorporated to titania for  $\text{H}_2\text{S}$  gas sensing [50], 10 wt%  $\text{Al}_2\text{O}_3$  was doped for  $\text{H}_2$  selectivity in reducing gas mixture ( $\text{CO}$ ,  $\text{CO}_2$ ,  $\text{H}_2$ ) containing ambient [36], 7.5 wt.% Al was added for  $\text{O}_2$  and  $\text{CO}$  sensitivity [35]. In addition, Ti-Ti-2wt% Al thin film was coated on Ti substrate and then subjected to potentiostatic electrochemical etching process for removing Al. The obtained porous titania was used as a sensor material for hydrogen detection [49]. In another study,  $\text{TiO}_2$  was doped with 20mol%  $\text{Al}_2\text{O}_3$  for phase retardation and a porous structure was formed in  $\text{TiO}_2$  material, however, this produced material is not suitable to use as a sensor material [54].

#### 1.4.8 The effects of Al doping on $\text{TiO}_2$ structure

In addition, since the fully oxidized Ti and Al ions are not isovalent and have different radii and therefore, bulk rutile  $\text{TiO}_2$  and  $\text{Al}_2\text{O}_3$  have no common lattice structure at any temperature or pressure and do not form a solid solution as seen in phase diagram (Figure 1.7). However,  $\text{Al}_2\text{O}_3$  can form a solid solution with anatase.

The defect structure of titania is complex as oxygen vacancies, interstitial or substitutional  $\text{Ti}^{3+}$  ions, and interstitial  $\text{Ti}^{4+}$  ions exist in the anatase form [55]. Since the ionic radius of  $\text{Al}^{+3}$  ion is smaller than  $\text{Ti}^{+4}$  ion,  $\text{Ti}^{+4}$  ion can be substituted by  $\text{Al}^{+3}$  ion. However, in literature there are many controversial results and assumptions about the location of Al ion in titania lattice [35,43,48-50]. This case was discussed in the result and discussion section.

The literature proposed the mechanism that phase transformation of  $\text{TiO}_2$  might start at the interfaces of contacting anatase particles [56]. It is also believed that Al doping stabilizes the anatase phase and thereby inhibits the anatase-to-rutile transformation kinetically [44]. The uniform distribution of alumina phase in titania matrix causes the reduction in the anatase-anatase contact points and thereby leading an increase in thermal stability. Thus, the activation energy for rutile nucleation is increased and rutile nucleation is suppressed. Consequently, this situation is considered as retarding effect on anatase-rutile transformation [42,43,56,57]. In addition, the literature proposed that the presence of dopant having smaller size than titanium can cause a lattice deformation and thereby the anatase phase is stabilized due to this deformation energy that is released before the phase transition [40].

Moreover, the electrical conductivity of Al doped  $\text{TiO}_2$  is higher than pure  $\text{TiO}_2$  [58] due to the presence of Al species in  $\text{TiO}_2$  lattice leads to band gap narrowing [59,60]. It was suggested that Al doping leads to a compression in the lattice constant and an increase in carrier concentration and consequently increases the electrical conductivity in the  $\text{TiO}_2$  [61]. It was also reported that the diffusion rate of oxygen ions is faster in Al-doped  $\text{TiO}_2$  lattice. The electrical conductivity provided by Al-doping can cause increase in sensor stability and sensitivity [52].

Al dopant restricts the grain growth [35,44,59] and as well as particle growth [35,58,62] depending on amount of dopant. However, in the case of the amount of dopant is exceeded, the retarding effect of dopant is disappeared [35,48-50]. The excess amount of dopant can precipitate as a second phase or form a complete layer of  $\text{Al}_2\text{O}_3$  on  $\text{TiO}_2$   $\text{Al}_2\text{O}_3$  on  $\text{TiO}_2$  [35,48-50,63].

On the other hand, in a few studies, it was reported that presence of Al ions in titania lattice increases the rate of phase transformation from anatase to rutile [43,55,64]. Yamaguchi and his group formed solid solution of  $\text{Al}_2\text{O}_3$  in anatase and they did not

observe any inhibitory effect of alumina on the transformation of anatase to rutile [43]. It was also assumed that the presence of Al was responsible for reducing particle agglomeration and increasing the rate of anatase-rutile transformation during the chloride process [55,64]. These differences might arise from different raw materials and preparation methods [43]. It was also determined that depending on the type of precursor used for Al doping a inhibiting ( $\text{AlOOH}$ ,  $\text{Al}(\text{OC}_4\text{H}_9)_3$ ,  $\text{AlCl}_3$ ,  $\text{Al}(\text{NO}_3)_3$ ) or promoting ( $\text{AlCl}_3(\text{g})$ ) effect in anatase-rutile transformation may be observed [37].

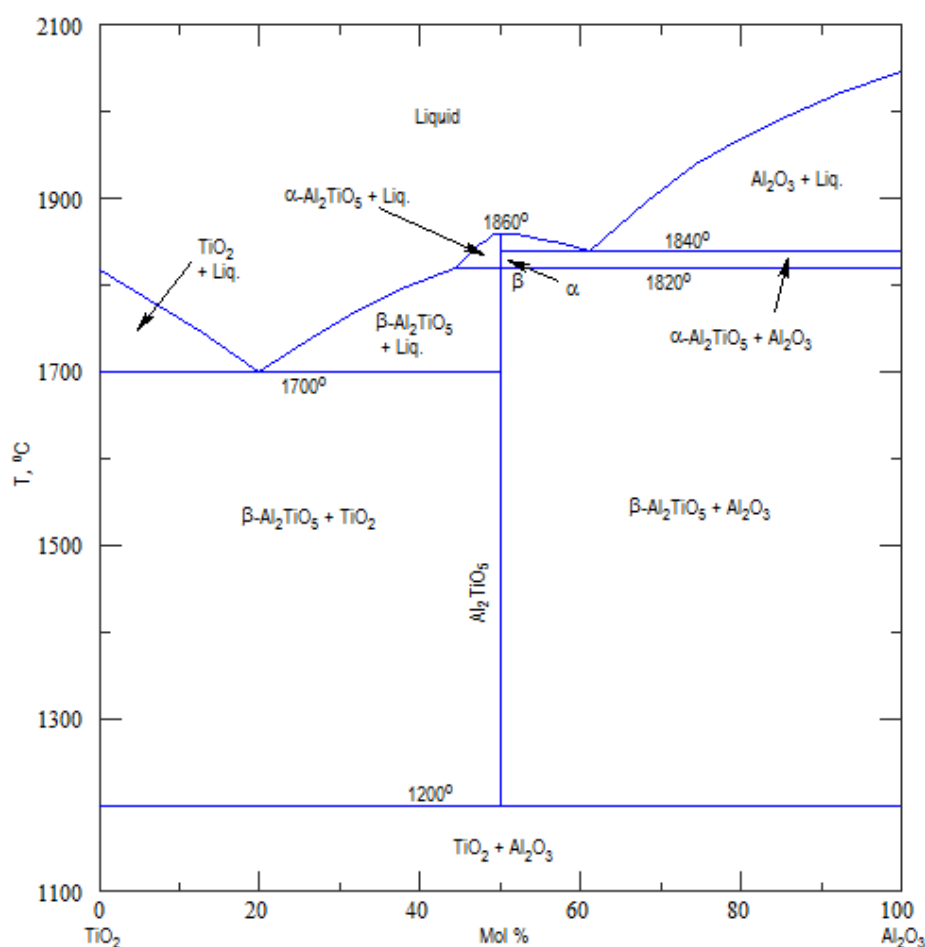


**Figure 1.7 :** The binary  $\text{TiO}_2$ - $\text{Al}_2\text{O}_3$  phase diagram [65].

## 1.5 Hydrogen Gas Sensors

Hydrogen gas has growing importance in many areas like fuel cells, cryogenic cooling, transformer oils, rocket fuel, oil distillation. However, a leakage of hydrogen may occur during many industrial processes and lead to explosion. In addition, hydrogen gas can make interference with other reductant gases. These



problems increase the demand of hydrogen sensors with high sensitivity and selectivity [18].

Literature reported various types of sensor technologies such as Schottky junction, fiber optic, catalytic, electrochemical, field effect transistor, oxide semiconductor, and combinations of these. Among these technologies, semiconductor oxide technology is relatively simple and also cheap [66]. In addition, the semiconductor oxide  $\text{TiO}_2$  has the continued and growing importance in the development of hydrogen gas sensors [11,12].

## **1.6 The Sensing Mechanism of $\text{TiO}_2$ Based Gas Sensors**

In doped semiconductor oxides, there are two types of detection mechanisms, namely, chemical sensitization and electronic sensitization.

In chemical sensitization, analyte gas molecules adsorbed on the surface of sensor and then these gas molecules are dissociated or activated with the help of dopant. These dissociated molecules interact with semiconductor oxide and this cause a change in conductivity of sensor surface. In electronic sensing, direct electron exchange electron occurs between the dopant and semiconductor surface. When the analyte gas contact with the dopant, a change in the oxidation state of dopant occurs due to the electron from dopant to oxygen. This results in a change in the conductivity of the sensor surface [50].

Some reducing gases can donate electrons to the conduction band of insulating oxides and thereby increase their conductivity. For instance, according to gas sensing mechanism of CO gas, CO molecules adsorb on the sensor surface and then they ionize. This results in releasing a free electron and a subsequent decrease in the resistivity of sensor. Since the reactions are surface dominated in CO gas sensing mechanism, the reversibility of reactions is better than diffusion controlled reactions (such as hydrogen gas) [36].

### **1.6.1 $\text{H}_2$ sensing mechanism of $\text{TiO}_2$ based gas sensors**

The periodicity of the crystal structure is broken at the surface of  $\text{TiO}_2$  and this causes the formation of unsaturated sites and these sites lead to creation of new energy levels (surface states) in the band gap, which act as a donor or acceptor.

These surface states have an important role in gas sensing mechanism and they contribute electron exchange with bulk. In air ambient, TiO<sub>2</sub> conductivity is low since the conduction electrons are bound to surface oxygen. When the atmospheric oxygen adsorbed on the surface of TiO<sub>2</sub>, the charge transfer occurs between TiO<sub>2</sub> and oxygen molecule as in the below reaction. As a result of this reaction (1.2), the oxygen molecule dissociates in the form of negatively charged oxygen species (O<sup>-</sup>, O<sup>2-</sup>, O<sub>2</sub><sup>-</sup>) by trapping the electrons in the conduction band of TiO<sub>2</sub>.



S=denotes sites on TiO<sub>2</sub> surface (space charge layer is created)

The negatively charged chemisorbed oxygen species cause an upward band bending of n-type TiO<sub>2</sub> as shown in Figure 1.8 and alter the band structure and also its Fermi level. Thus the transfer of electrons from TiO<sub>2</sub> conduction band to oxygen (surface states) leads to the formation of a depletion layer (electron depletion zone) or space charge layer in the near surface region. In this depletion layer, the charge carrier concentration is reduced and only ionized donor or acceptor impurities are left. The creation of depletion layer increases the work function of grains and this causes formation of Schottky barriers at the grain boundaries (seen in Figure 1.9). During the free charge exchange, electrons have to overcome these potential barriers which are generated between the surface and the inside of TiO<sub>2</sub>. These barriers are responsible for a very high resistance of TiO<sub>2</sub> in air. The resistance changes with a change in the barrier height. The heights of these barriers are depending upon the oxygen partial pressure in the environment due to the concentration of adsorbed oxygen ionic species cause the formation of these barriers.

Upon exposure to H<sub>2</sub> reducing gas, H<sub>2</sub> reacts with chemisorbed oxygen species as in the below reaction. As a result of this reaction water is formed and the electrons are no longer bound to the surface states and the trapped electrons are released back into the conduction band of the TiO<sub>2</sub>. Thereby, the adsorbed oxygen is consumed and decreased down to a steady state level depending on concentration of H<sub>2</sub>, resulting in a corresponding decrease in work function and the potential barrier and a sharp reduction in the electrical resistance [1].



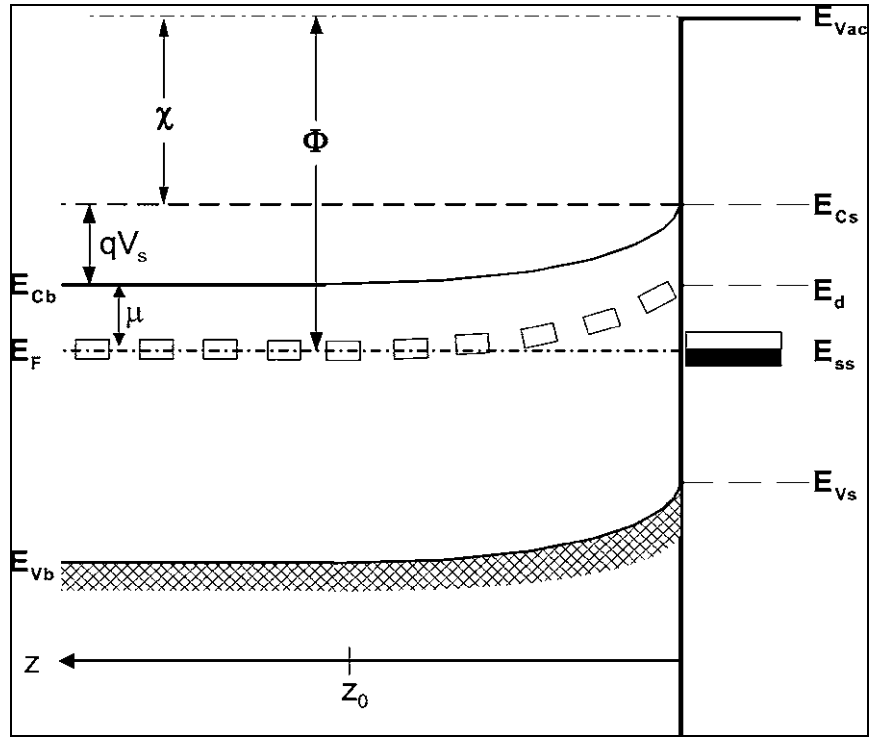


**Figure 1.8 :** Band bending after chemisorption of charged species (here ionosorption of oxygen on  $E_{ss}$  levels).  $\phi$  denotes the work function,  $\chi$  is the electron affinity, and  $\mu$  the electrochemical potential,  $qV_s$  is the band bending and  $z_0$  is the depth of depleted layer.  $E_{vac}$ ,  $E_{cb}$ ,  $E_{vb}$ ,  $E_F$  are the vacuum energy level, bottom of the conductive band, top of the valence band and Fermi level energies, respectively.  $E_{cs}$ ,  $E_{vs}$  are the values of conductive and valence band borders at the surface,  $E_d$  and  $E_{ss}$  are the levels of donors and surface states. [67].

Depletion layer is characterized by its thickness ( $L_s$ ) and surface/schottky potential ( $V_s$ ). In the thickness of space charge layer ( $L_s$ ), charge carrier concentration is decreased. Typical values of  $L_s$  are usually in the range 1-100 nm. The relationship between the magnitude of crystallite size ( $D$ ) and  $L_s$  determines the control mechanism of conductivity and it can be controlled either by of the three different cases; grain boundaries, necks or grains. The effect of grain size on gas sensitivity is schematically illustrated in Figure 1.10. The highest gas sensitivity value has been achieved when the conductivity mechanism is grain size controlled and this situation occur when  $D < 2L_s$ . In these grain size ranges, chemisorption becomes more effective [1,39]. In this case, grains are fully depleted of mobile charge carriers and thus every grain is fully involved in space charge region. The energy bands are nearly flat throughout the whole structure of the interconnected grains. Due to there are no significant barriers for intercrystallite charge transport, the conductivity is essentially grain controlled. So, the decreasing in grain size leads to increase in the sensitivity.

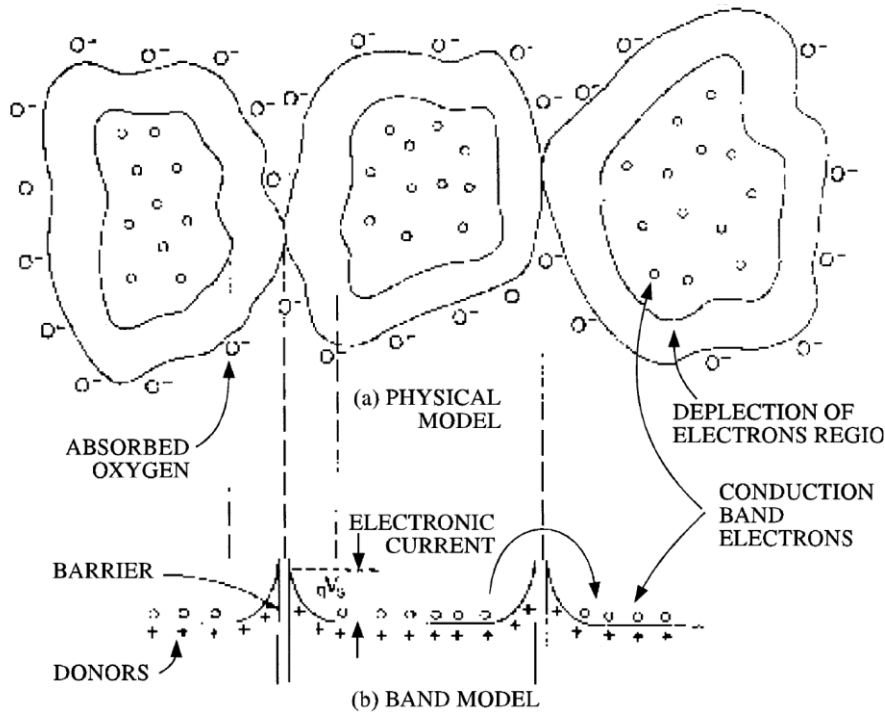


**Figure 1.9 :** Energy barriers formation at the grain boundaries due to the formation of space charge layer [67].

Particularly for the case of  $D \gg 2L$ , the crystallographic orientation of the plane strongly affects the gas sensing properties. This is because different crystallographic orientations have different atomic arrangements and therefore different electronic properties, such as, surface state density, adsorption/desorption energies of interacted gas molecules, concentration of adsorption surface states, etc. This leads to the different chemisorption characteristics of the crystal surfaces. While some crystal faces are highly reactive due to the high number of unsaturated bonds on their surface, surface atoms of the other crystal faces are bound to each other strongly and this leads to decrease in their reactivity [1].

## 1.7 Nanostructured Gas Sensors

The sensitivity and selectivity of sensors can be improved by adding catalysts and/or dopants. However, the most important development in performance of sensors was observed when the crystal size is reduced to nanometer level to get extended specific surface area [3]. This is because nanocrystalline metal oxide films show gas sensing properties when their crystal sizes approach the Debye length [68,69].

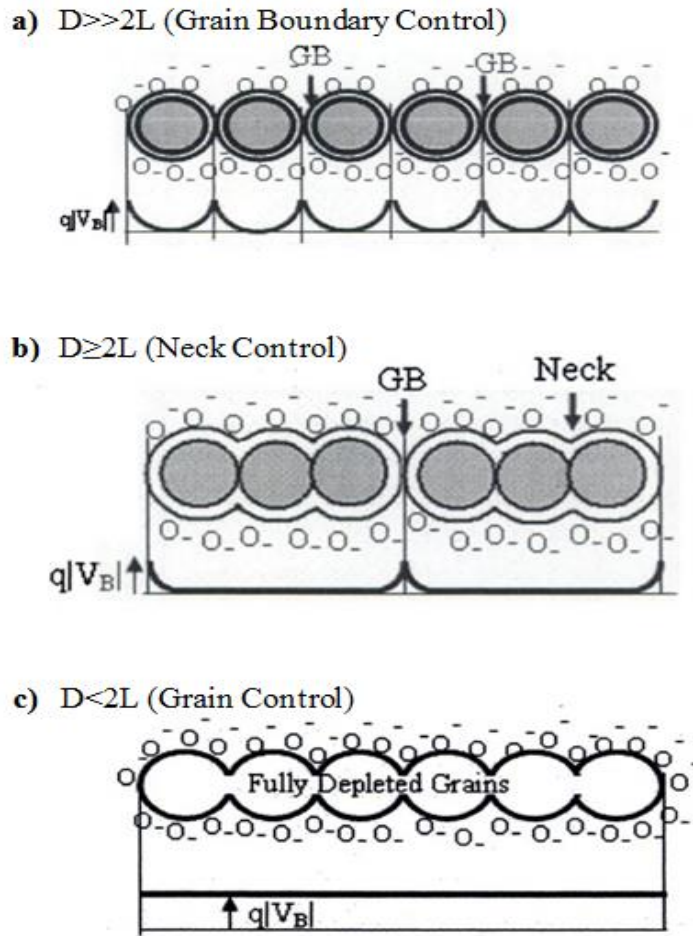


**Figure 1.10 :** The schematic illustration of grain size effect on gas sensitivity [1].

### 1.7.1 Nanostructured TiO<sub>2</sub> based gas sensors

Some surface reactions such as adsorption, chemisorption, reduction/oxidation etc occur between gas molecules and a surface of material acting as a receptor. Since the surface reactions govern the gas detection, surface of gas sensor material play a a distinctive role in detection of analyte gas [70]. In TiO<sub>2</sub> based sensors having surface/volume ratio nanoporous/nanotubular structure are the promising sensor type. In these sensors, charge transfer is provided by the crystallized nanotube walls and the tube connecting points and the current passage from one nanotube to the other is easier due to the very low resistance during this transition [71,72]. In addition, their nanoporous/nanotubular structure make easier to diffusion of analyte gas to the bottom of sensing element and allow for better interaction [73]. This type of sensors exhibit higher sensitivity towards analyte gas and an improvement is observed in their response and recovery times [73,74]. In literature, many reports are available about nanostructured TiO<sub>2</sub> based gas sensors [71,72].

### **1.7.2 Nanostructured TiO<sub>2</sub> based thin film gas sensors**

In a variety of studies in literature, formation of nanotubular structure on the surface of Ti foil sensor material increase the sensitivity of TiO<sub>2</sub> sensor material towards the hydrogen gas [71,72]. Also, most of the nanotubes and nanopores are formed on the surface of Ti foil, this material is restricted in the application of thin film based sensor [74]. There are only few studies in literature about nanostructured thin film sensor. Such as, Sadek and his group formed nanostructures on Ti thin film coating deposited on gold inter-digital transducer and tested this material as a hydrogen sensor material [74]. Chu and his group coated ITO with aluminium and formed nanopores on aluminium and they deposited TiO<sub>2</sub> inside the pores with sol-gel method [75]. Grimes and his group produced TiO<sub>2</sub> nanotubular structure on thin film and used this material for hydrogen sensing [68].

### **1.7.3 H<sub>2</sub> sensing mechanism in nanotubular TiO<sub>2</sub> based sensors**

The hydrogen sensing mechanism in nanotubular structure is the same as in the bulk TiO<sub>2</sub>, with a few differences. When one dimensional nanostructures are used for gas sensing, the effects of bulk are eliminated and the depletion layer extends throughout the thickness of the nanostructures. Since the nanotubes are small enough for the adsorption of redox species, a nanotube can change the bulk electronic structure of the entire nanotube not merely its surface [1]. In TiO<sub>2</sub> nanotubular structure, the crystallized nanotube walls and the tube connecting points provide more easier charge transfer (current passage) from one nanotube to the other due to the very low resistance during this transition[1,71,72]. At these regions, the chemisorption of oxygen species leading to formation of depletion layer by trapping the electrons in the conduction band of TiO<sub>2</sub>. In this depletion layer, the charge carrier concentration is reduced and only ionized donor or acceptor impurities are left. The creation of depletion layer increases the work function of grains and this causes formation of Schottky barriers at the grain boundaries. During the free charge exchange, electrons have to overcome these potential barriers and the resistance changes with a change in the barrier height [1].

The width of the depletion layer in which electron exchange occurs between the bulk and surface states is comparable to the diameter of the nanotubes itself. If the half-thickness of nanotube wall ( $t/2$ ) is comparable or less than the depletion region ( $t/2 \leq$

$L_s$ ), as shown in Figure 1.11, tremendous resistance change can be observed on exposure to hydrogen. (flat band condition). The small wall thickness may result in the overlap of neighbouring depletion regions, thus the entire volume of the intertubular region may experience low resistivity. In literature, it was mentioned that nanotube arrays with smaller diameter and thin walled nanotubes showed more higher hydrogen sensitivity [66].  $\text{TiO}_2$  nanotubes having a wall thickness of  $\sim 13$  nm demonstrated remarkable resistance change [68]. In the case of  $t/2 \gg L_s$ , oxygen removal by hydrogen and subsequent hydrogen chemisorption will have little effect on resistance and therefore high gas detection cannot be expected [1,66].

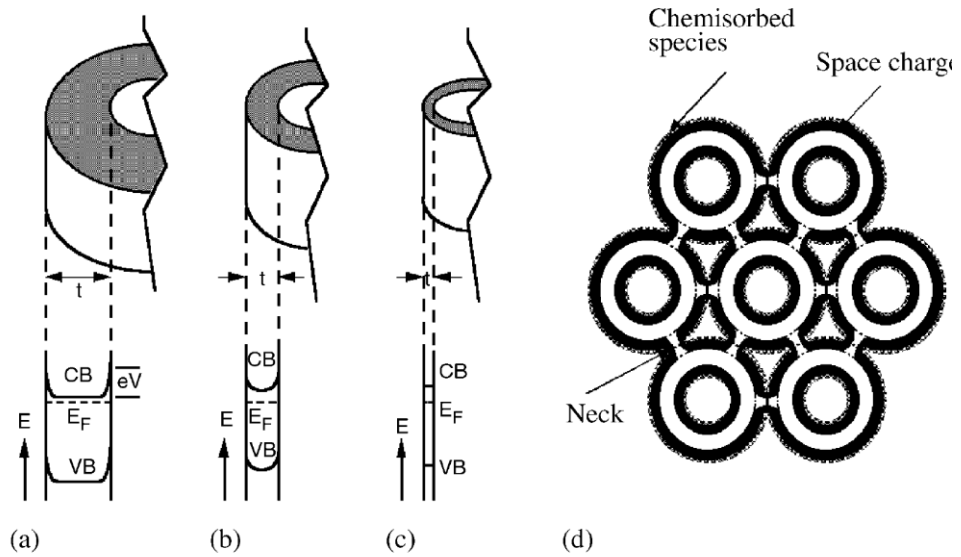


**Figure 1.11 :** The influence of nanotube wall thickness on band bending due to oxygen chemisorption: (a) when nanotube wall half-thickness ( $t/2$ ) is much greater than the space charge layer, (b) when comparable, and (c) when  $t/2$  is less than the width of the space charge region. (d) Schematic illustration of nanotubes, top view, and the tube-to-tube connecting points corresponding to case shown in (a). [66].

When the nanotubular structures are exposed to  $\text{H}_2$  analyte gas,  $\text{H}_2$  reacts with chemisorbed oxygen species as in the following reaction. Thereby, the adsorbed oxygen species are removed by hydrogen atoms and subsequently chemisorption of hydrogen atoms occurred [1,75]. Consequently, water is formed, the trapped electrons are released back into the conduction band of the  $\text{TiO}_2$  and an electron-rich region within the nanotube walls forms [1].

This resulting in a corresponding decrease in work function and the potential barrier and a sharp reduction in the electrical resistance [1].



#### **1.7.4 The Effects of crystallographic structure of TiO<sub>2</sub> nanotubes on sensing properties**

Bulk reactions take place at 700-1000°C and therefore the rutile phase which is stable at high temperatures is used for these reactions. Since the surface reactions do not occur at high temperatures (They take place at 400-500°C), the meta-stable anatase phase can be used for surface reactions [27]. TiO<sub>2</sub> can be prepared as an anatase or rutile phase form depending on the analyte gas that will be detected [27]. Literature proposed that the anatase phase of TiO<sub>2</sub> is sensitive to H<sub>2</sub> gas and also to the other reducing gases [35].

In all temperature and pressure ranges, the bulk rutile is thermodynamically more stable compared to anatase phase due to its lower free energy. However, the anatase phase becomes more stable in extremely small crystallite size (11-45 nm) and high surface areas since the planes of anatase phase have lower surface energy. This case indicates that the surface energy considerations outweigh those of bulk thermodynamics and so, for crystallites below a critical size (11-45 nm), anatase has a lower total (bulk and surface) free energy [37].

In general, the morphology and the structure of porous layers are affected strongly by the electrochemical conditions (particularly the anodization voltage) and the solution parameters (in particular the HF concentration, the pH and the water content in the electrolyte). After the anodization process, the amorphous TiO<sub>2</sub> nanotubular structure is obtained [6]. Crystallinity is essential when biocompatible, photocatalytic or semiconducting membrane properties are desired or for any application involving electrical charge carrier generation and transport/transfer [76]. The nanotubes are exposed to thermal annealing at different temperatures to induce crystallinity. The annealed TiO<sub>2</sub> nanotubular structures retain their tubular morphology [6,7,77]. The tubes can be converted to anatase at temperatures higher than approximately 280°C in air [69,77]. The fabricated Ti nanotube structures consist of significant amounts of F<sup>-</sup> (~1–5 at.%) and a minor contents of hydroxides on the surface of the tube walls. Annealing at 300°, the content of fluorides is almost lost and the amount of surface hydroxides is reduced [6]. After annealing at temperatures higher than approximately 450°C, a mixture of anatase and rutile is formed. The structures are completely transformed to rutile phase at a temperature range of 620-680°C [69,77].



It should be also pointed out that in gas sensor applications, anatase TiO<sub>2</sub> phase is more preferable compared to rutile phase owing to its low resistance and fast response properties [12].

### 1.7.5 The effects of TiO<sub>2</sub> nanotube sizes on gas sensing properties

Nanotubular TiO<sub>2</sub> sensor demonstrate higher gas sensitivity compared to TiO<sub>2</sub> thin film sensors due to their large sensing surface area [69]. In literature, there are few reports about the effects of nanotube sizes on gas sensing properties of a sensor.

It is assumed that the diameter of nanotube has a significant influence on gas sensing and a smaller nanotube diameter was found to be more sensitive to hydrogen gas [78]. The thickness of nanotube wall is also proposed as a significant parameter in gas sensing mechanism. It was reported that if the nanotube wall half-thickness  $t/2$  is comparable to or less than the space charge region, the sensitivity of sensor can be improved. The highest sensitivity was obtained when the wall thickness and nanotube diameter were  $\approx 13$  nm and 30 nm, respectively. The inter- connecting points also has an important role in gas sensing since the current passing from nanotube to nanotube is more easier at these constricted points. It was also proposed that the length of nanotubes mainly affected the response and recovery times of sensor [72].

## 1.8 TiO<sub>2</sub> Nanotubular Structures

### 1.8.1 The nanotube growth mechanism on the surface of Ti metal

The formation of TiO<sub>2</sub> nanotube arrays is a direct consequence of competition between three processes. These processes are:

- i) Electrochemical oxidation of Ti into TiO<sub>2</sub>  

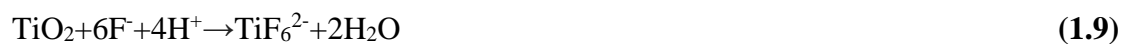
$$\text{Me} + 2\text{H}_2\text{O} \rightarrow \text{MeO}^{+2} + 4\text{H}^+ + 4\text{e}^- \quad (1.5)$$
- ii) The electrical field induced dissolution of TiO<sub>2</sub>
- iii) The chemical dissolution of TiO<sub>2</sub> by fluorine ion. [6,77]  

$$\text{MeO}^{+2} + 6\text{F}^- \rightarrow [\text{MeF}_6]^{-2} \quad (1.6)$$

In anodization of Ti, the presence or absence of fluoride ions changes the oxide growth mechanism (Figure 1.12). In the electrochemical oxidation stage, Ti metal interacts with O<sup>-2</sup> ions in the water and the initial oxide layer is growth at the surface.

Then  $O^{2-}$  anions transport through the oxide layer and react with Ti metal at the metal/oxide interface.  $Ti^{4+}$  cations are ejected from the metal/oxide interface by the electric field and migrate towards the oxide/electrolyte interface. Thus, the growth of oxide layer is continued by the transportation of  $O^{2-}$  ve  $Ti^{4+}$  ions through the growing oxide under the electric field (**1.7** and **1.8**) [6,66,79]. Since the Ti–O bonds are polarized and are weakened under the applied electric field, field-assisted dissolution of  $TiO_2$  is occurred at the oxide/electrolyte interface and the metal  $Ti^{4+}$  cations dissolve into the electrolyte [79].

In the presence of fluoride ions,  $TiO_2$  reacts with fluoride ions and they form water soluble  $TiF_6^{2-}$  complex (**1.9**). This complex formation prevent the precipitation of hydroxide layer at the oxide/electrolyte interface by providing a continuous chemical dissolution of  $TiO_2$  . Moreover fluoride ion with small ionic radius can enter the growing  $TiO_2$  lattice and move towards the oxide layer by the electrical field and can compete with the  $O^{2-}$  transport [6].



If  $Ti^{4+}$  ions arriving at the oxide/electrolyte interface are not ‘made soluble’ by complexation, a hydroxide layer will precipitate in most electrolytes [6]. The complex formation ability leads to a permanent chemical dissolution of formed  $TiO_2$  and prevents hydroxide layer precipitation as  $Ti^{4+}$  ions arriving at the oxide/solution interface [6].

In anodization of Ti, the layer thickness and the current density reach a limiting value after a certain polarization time and this behavior can be explained by a steady state situation. During Ti anodization, oxide growth occurs continually at the inner interface and simultaneously chemical dissolution of oxide layer is occurred. Steady state is established when the pore growth rate at the metal oxide interface is identical to the thickness reducing dissolution rate of the oxide film at the outer interface. It should be pointed out that the chemical dissolution of  $TiO_2$  occurs over the entire tube length, thus the tubes with extended time become increasingly v-shaped in morphology. Therefore, after a long duration of anodization process, more thinner walls can be obtained at the tops of the tubes compared to their bottoms [7].

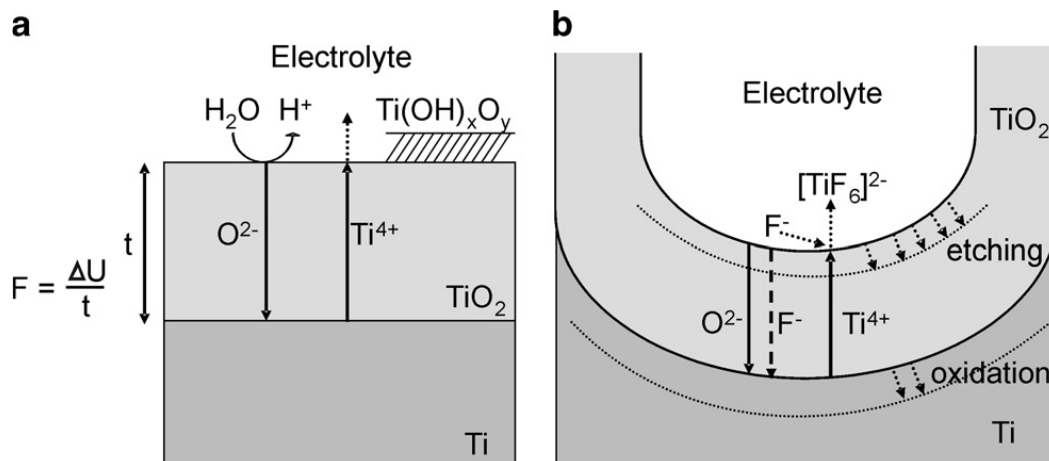


**Figure 1.12 :** Schematic representation of the Ti anodization (a) in absence of fluorides (results in flat layers), and (b) in presence of fluorides (results in the tube growth) [6].

### 1.8.2 Anodization parameters influencing the nanotube morphology

Several factors strongly influence the morphology of nanotubes and also the degree of their ordering. These are; the anodization voltage, the type and composition of electrolyte, anodization duration, anodization temperature, the purity of the material, stirring, etc. Proper selection of these parameters has enabled to form anodic oxide membranes with various variation of pore sizes, outer diameters, wall thicknesses, tube-to-tube spacing, lengths [6,66,76].

#### The influence of anodization voltage:

The tube diameter is controlled by changing the anodization voltage. The highest possible voltage just below dielectric breakdown seems most convenient to improve the ordering [2]. It was demonstrated that the sample of 5V presents a nanoporous structure and no tubular structure is formed. As the voltage is increased, the porous appearance is lost and with discrete, tubelike features appearing. When the voltage was further increased, only a spongelike porous structure was formed at 35V and the nanotube structure was destroyed completely. At higher voltages, under the effects of electric field, the Ti–O bond undergoes polarization and is weakened, promoting dissolution of the metal oxide. Therefore, no nanotube structure can be obtained [77].

Ge et al. produced highly ordered titania nanotube arrays at anodization voltages ranges between 10 V to 25 V ( using fluoride containing acetic acid solution for temperatures from 0 °C to 35 °C) As they increased the voltage, the pore diameter and the length increased but the wall thickness decreased [36].

### **The influence of electrolyte:**

Electrochemical oxidation of titanium has been studied in sulfuric acid, phosphoric acid, acetic acid with or without HF solution [6]. At lower pH, the length of the nano-tube was limited by higher dissolution rate [80]. The nanotubes grown in HF electrolytes or acidic HF mixtures showed limited thickness 500–600 nm [6]. By using buffered neutral electrolytes containing NaF or NH<sub>4</sub>F and taking into account the importance of the pH gradient within the tube, Ti nanotubes with higher than 2  $\mu\text{m}$  thickness could be grown. In addition, Schmuki and co-workers reported formation of longer nano-tubes during anodization of Ti in neutral fluoride solutions. They achieved nano-porous structure by controlling electrochemical parameters to induce acidification at the pore bottom [19].

Nonaqueous electrolytes (e.g., glycerol, ethylene glycol, etc.) containing fluorine ion was used to form TiO<sub>2</sub> nanotube arrays with significantly increased film thickness (100  $\mu\text{m}$  in length). This is because, in the nonaqueous electrolyte, the mobility of the fluorine ion was largely suppressed; thus, the chemical dissolution of TiO<sub>2</sub> was decreased. According to Wang et al. study, in aqueous electrolyte, the anodization potential exhibited significant influence on the formation of highly ordered TiO<sub>2</sub> nanotube arrays, while little effect from the electrolyte temperature was observed. In nonaqueous electrolyte, the electrolyte temperature markedly affected the TiO<sub>2</sub> nanotube dimensions, while, unlike in the aqueous electrolyte, anodization potential exhibited slight influence [7].

The Ti nanotubes grown in glycerol electrolytes had extremely smooth walls, while using CH<sub>3</sub>COOH electrolytes remarkably small tube diameters could be obtained. Meanwhile, in aged ethylene glycol electrolytes and by a further optimization of parameters, the length of nanotubes having an almost ideal hexagonal arrangement has reached 260  $\mu\text{m}$  [6].

In 2006, Grimes and co-workers reported the first use of polar organic solvents such as dimethyl sulfoxide (DMSO), ethylene glycol, formamide, and *N*-methylformamide to achieve nanotube array lengths of several hundred microns. Recently Paulose et al. reported the fabrication of nanotube reached to 1005  $\mu\text{m}$  in length to use in bio-diffusion [76].

### 1.8.3 The nano structures grown on Ti alloys

Other than pure Ti, its alloys that can be anodized: Ti-8Mn, Ti-Nb, TiZr, Ti45Nb, Ti-28Zr-8Nb, Ti-29Nb-13Ta-4.6Zr, Ti-2Al-1.5Mn, Ti-6Al-4V, Ti-6Al-7Nb [81]. For instance, nanoporous or nanotubular structures are grown on the surface of Ti-6Al-4V and Ti-6Al-Nb alloys in order to use in bio-medical applications [82]. There are few studies about the nanostructure formation on TiAl. Such as, Bayoumi and his group dealloyed TiAl alloy and formed TiO<sub>2</sub> nanotubes [83]. Tsuchiya and his group produced TiAl alloy including 50at%Al and try to obtain nanoporous structure on TiAl alloy [84]. However, these produced nanostructures on TiAl alloys consist excess amount of Al and therefore they are not suitable for sensor applications.

The growth of nanotubes on various alloys increases the potential functionality of the tubes (by e.g. incorporation of doping species in the oxide structure). For instance, if a binary Ti-Nb alloy, rather than pure Ti, was used as a substrate the range of achievable diameters and lengths of TiO<sub>2</sub>-based nanotubes can be significantly expanded. In addition, the morphology of the tubes differs significantly from that of the nanostructures grown under the same conditions on pure Ti or Nb substrates: only considerably shorter tubes grow on Ti, whereas irregular porous structures grow on Nb. Another interesting example is that, if the anodic nanotubes formed on TiZr alloys, the oxide nanotubes exhibits a morphology between those of titanium oxide and zirconium oxide nanotubes. These nanotubes show a largely expanded structural flexibility compared with nanotubes formed on the individual elements [6].

Moreover, the attempts have been maintained to grow nanostructures on the surface of various Ti alloys. However, compared to pure Ti, many titanium alloys exhibit binary phases ( $\alpha$ - $\beta$ ) which are chemically different from each other. Therefore, formation of nanotubular structure on alloy coatings is mainly suffered from two problems [81];

- i) the selective dissolution of less stable elements,
- ii) the different reaction rates on different phases of an alloy.

Therefore the creation of nanotube structures on Ti alloys is still challenging task. Despite these problems, if the formation of nanotube structures on various Ti alloys is achieved successfully, the functionality of nanotubes will be increased and thus these structures will find important application areas [81].

## 1.9 The Deposition Techniques for Producing Ti or TiO<sub>2</sub> Thin Film Coatings

The most significant characteristics of gas sensing materials are sensitivity, selectivity and their stability. An ideal gas sensor gives response to very low analyze gas concentrations, it is not affected by interfering gases in the ambient and it has long term stability. The important bottlenecks in the development of an ideal gas sensors are the insufficient understanding of gas-film interactions and sensing mechanism, and a lack of control on film deposition parameters. For instance, the deposition parameters of thin films can affect the microstructure, composition and the morphology of semiconductor metal oxide. In order to develop gas sensor with high sensitivity and selectivity, it is necessary to improve the production methods of gas sensor materials [5].

TiO<sub>2</sub> based semiconductor oxide gas sensor materials can be produced using two routes;

1. It can be deposited on substrate in the oxide form using sol gel, physical vapor deposition (PVD) and chemical vapor deposition (CVD) [30,31,34,85-88].
2. It can be deposited on substrate in the metal form using CVD technique and subsequently subjected to an oxidation process [70]

The production of TiO<sub>2</sub> thin films on different substrates can increase their potential applications in many functional devices. In literature, TiO<sub>2</sub> thin films deposited on substrates such as glass, sapphire, Si [86,87] and metallic Ti thin films deposited on Si, ITO, nanoporous AAO, quartz [69].

In production and applications of sensor platforms of functional sensor devices that are used in harsh environments the sensor material is generally deposited on ceramic substrates. In literature, RF sputtering and e-beam evaporation PVD are two commonly used techniques to deposit TiO<sub>2</sub> or metallic Ti thin films on different substrates [85-87]. However, it is difficult to produce dense and well-adherent and thin film coatings on substrates using these techniques. The deposited thin film coatings are not well-adherent to substrates and spall of the surface during the electrolytic process (anodization process).

In Figure 1.13, the surface SEM image of Ti thin film coating produced by RF sputtering technique is shown [31]. The grain structure and surface morphology of

this produced coating are not suitable to form uniform nanostructures. In the case of anodization of the granular surface, because of the large curvatures in the boundary of the connected grains, this level of roughness generates inhomogeneous electric field distributions on the surface which results in preferential nanopore growths in these parts, and randomly distributed nanopores are formed eventually [23].

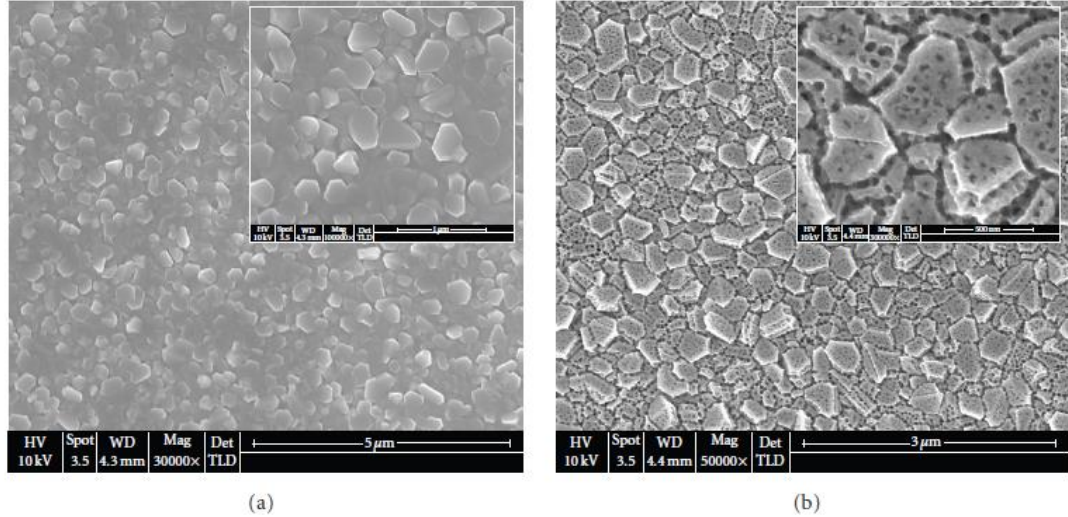


**Figure 1.13** The surface SEM images of a) Ti thin film produced by Rf sputtering technique b) the as-anodized surface of Ti thin film by RF sputtering technique [31].

Therefore, there is a continued demand for developing methods to produce thin film coatings with an equiaxed grain structure that will give well ordered nanotubular structure during anodization. In the present study, cathodic arc technique is suggested for producing dense, well-adherent and equiaxed grained metallic Ti thin films on ceramic and metallic substrates. It is also possible to produce Ti-Al coatings possessing the appropriate structure and desired composition using the cathodic arc method. In literature, there is only one study that suggests using cathodic arc technique for producing Ti film coating. In this study, filtered cathodic vacuum arc deposition technique was used to deposit Ti thin film with a thickness of 300 nm on quartz substrate. However, there is no details about this study [69].





## 2. EXPERIMENTAL DETAILS

Ti and TiAl coatings were produced by cathodic arc based technique using a DC cathodic arc Physical Vapor Deposition (PVD) instrument (Novatech-SIE, Model: NVT-12). Ti and TiAl coatings were deposited on both alumina substrates (Kyocera) and pure metallic Ti substrates (50mm x 25mm in size). For TiAl coatings TiAl (25 at % Al) cathode was used. Prior to the deposition process, the substrates were preheated and also cleaned by applying DC bias voltages of -600 V, -800 V, -1000 V. During pretreatment, 600 V and 800 V were applied to substrates for 1 min then 1000 V was applied for 15-45 sec and the substrates were heated until 850-950°C. After the pretreatment, Ti and TiAl coatings were deposited on substrates at different bias voltages and durations ( the details were given in the corresponding section). All Ti and TiAl coatings were produced in direct current (DC) mode, using a cathode current of 60 A and 20 sccm argon gas flow rate.

Nanotubular structures were created on the surface of these coatings via anodization process. In anodization process Ti and TiAl layers were anodically oxidized in ethylene glycol based electrolyte using various anodization parameters. ( the details were given in the corresponding section). Before anodization process, Ti and TiAl coating surfaces were chemically polished for 5 sec in a mixed solution of HF, H<sub>2</sub>O and HNO<sub>3</sub>.

Surface investigations of the specimens were characterized using JEOL JSM\_7000F field emission gun scanning electron microscopy (FEG-SEM). Al contents were determined by an energy dispersive spectrometer (EDS) attached to FEG-SEM. The phase structure of coatings were analyzed using Philips PW 3710 X-ray diffractometer (XRD) and a micro-Raman spectroscope (LabRam 800, Horiba Scientific, Jobin Yvon, France). In XRD analysis, Cu K $\alpha$  was used as the radiation source (incident angles 2°). Both power X-ray diffraction (PXRD) and glancing angle X-ray diffraction (GAXRD) were performed. The incident angles taken as 2° for GAXRD analyses. In micro-Raman analysis, the excitation source was a He-Ne laser with 632.8 nm line and 50 $\times$  objective was used to focus the laser beam. The

beam diameter was approximately 1  $\mu\text{m}$  and the laser power on the sample surface was 3 mW.

The heat treatments were done in tube furnace (Lenton) at 280°C, 350°C, 420°C, 485°C, 550°C, 600°C, 650°C and 720°C. These heat treatments were made under atmospheric conditions for 1 hour and a separate sample was used for each heat treatment temperature. For heat treatment Simulation study was performed In order to reveal the anatase  $\text{TiO}_2$  planes that are affected from “c” lattice parameter, a simulation study was performed. The simulation study was performed using Mercury 3.0 software and the Least Square Regression method.

In order to complete sensor fabrication two parallel Pt contact pads (13mmx2mm) were deposited on the surface of masked nanotubes using magnetron sputtering technique. The spacing between two Pt contact pads is 2 mm. The Pt pads were deposited at 100W during 1 min. These samples were used as sensor electrode materials.



**Figure 2.1 :** The image of the sensor measuring system.

The hydrogen sensing performance of nanotubular TiAl oxide sensors were tested using the measuring system shown in Figure 2.1. The results of these sensor tests were given and also evaluated in the Section 6. In this sensor measuring system, a tube furnace was used as a test chamber and a stainless steel spiral tube was placed in this furnace. The fabricated sensor was attached to the stainless steel spiral tube placed in the test chamber as shown in Figure 2.2.



**Figure 2.2 :** The fabricated sensor was attached to the spiral stainless steel tube placed in the test chamber.

The furnace temperature was fixed to the operating temperature and the gases were fed to the system using mass flow controllers. The target gas was heated inside the spiral shaped stainless steel tube which provides a long path to heat the target gas. The temperature in the test chamber was measured by using an additional K- type thermocouple that was placed close to the samples. During the sensor tests, the resistances of sensor elements were measured by computer-controlled high resistance electrometer (Keithly 6517B). A constant bias voltage of 1 V was applied to the sensors. The resistances of sensor electrodes were measured first under air ambient and then in a mixture of predetermined amount of hydrogen gas and carrier gas argon (Ar). MKS Mass flow controllers were used to regulate gas flows through the test chamber. In every step, the flow rate of carrier gas and gas mixture was 400 ml/min and duration was 30 minutes. The test gas hydrogen was mixed in appropriate ratios with argon to create the desired test gas ambient. The concentrations of hydrogen gas in carrier gas were 50 ppm, 100 ppm, 300 ppm, 500 ppm, 1000 ppm and 2500 ppm. The changes in resistance were recorded in commercial software program supplied by Keithley.



### 3. INVESTIGATION OF THE CAPVD PROCESS PARAMETERS FOR THE DEPOSITION OF WELL ADHERENT AND DENSE Ti AND TiAl COATINGS

RF sputtering and e-beam evaporation PVD are the two commonly used techniques to deposit  $\text{TiO}_2$  or metallic Ti thin films on different substrates [5-7]. However, these techniques are insufficient to produce coatings that are well-adherent, dense and resistant to the electrolytic processes used for producing nanotubular structures.

In our previous preliminary studies the same observations were verified for Ti and TiAl coatings that were produced using magnetron sputtering. It was determined that Ti and TiAl coatings produced by magnetron sputtering were not suitable for use in the fabrication of nanostructured sensor materials. These coatings were not well-adherent to substrates and spalled off the surface in the electrolyte used for the anodization process. The coatings that spalled off surface partially and completely during anodization process were shown in Figure 3.1 and Figure 3.2, respectively.

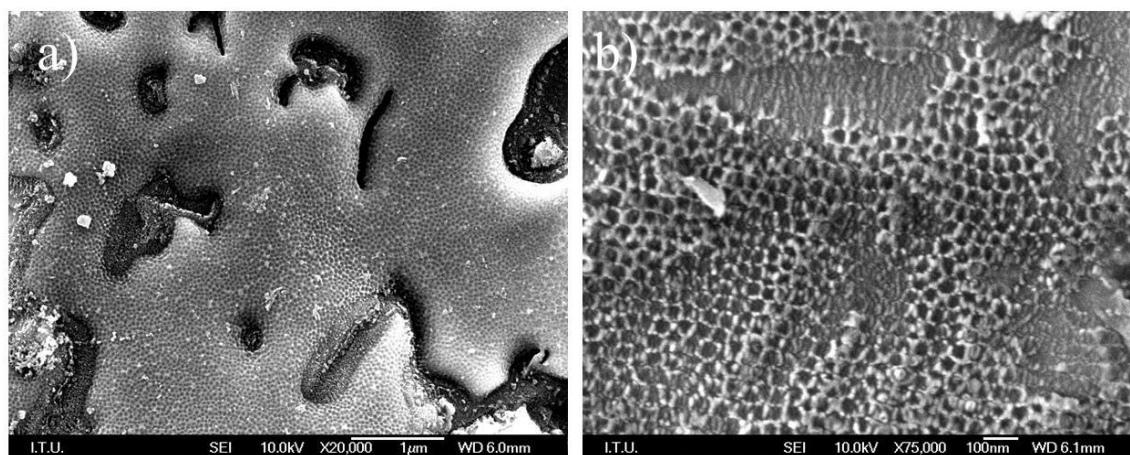


**Figure 3.1 :** The surface SEM images of Ti deposited alumina produced by magnetron sputtering after anodization process.

Therefore, it is decided to use cathodic arc PVD method for producing well-adherent and durable Ti and TiAl coatings possessing the appropriate structure and desired composition. Compared to other PVD methods, the high degree of ionization in arc plasma can be provided using cathodic arc PVD method. In pretreatment stage, the

heating of the substrates by the effect of energetic ions also provide good adhesion of coatings to the substrates. Hence, it becomes possible to deposit dense and well-adherent metallic thin films, with denser structure on ceramic and metallic substrates with this technique. In addition to that we also used a high bias voltage post treatment for producing denser coatings with equiaxed structure (similar to wrought titanium). Therefore Ti and TiAl films were produced with CAPVD by utilizing different bias voltages and also by post treatment with high bias voltages for testing their suitability for porous anodizing.

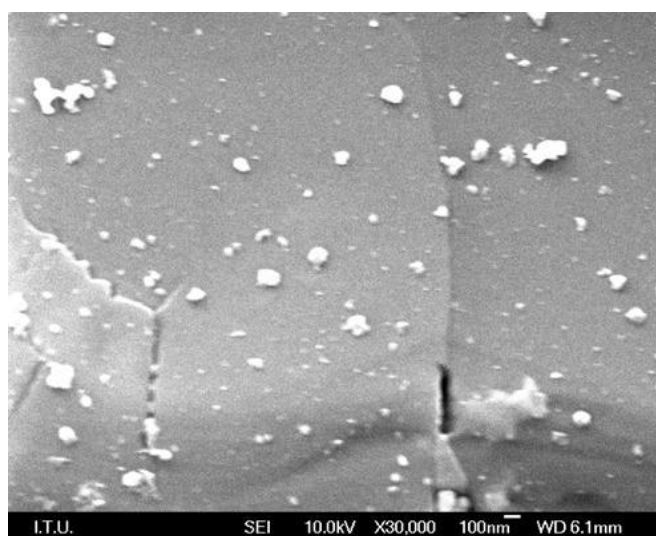


**Figure 3.2 :** The SEM image of TiAl deposited alumina produced by magnetron sputtering after anodization process.

### **3.1 Investigation of the CAPVD Process Parameters for the Deposition of Ti Coatings**

For optimization of the CAPVD process, the main parameter used in the experiments was selected as the bias voltage since this voltage exerts the main effect on the structure of the deposited coatings. Namely utilization of high bias voltages led to denser coatings. After deposition, coatings were characterized with respect to their structure and composition by using SEM and XRD investigations.

#### **3.1.1 The effects of bias voltage on microstructural properties of Ti coating**

Ti coatings were produced at different bias voltages in order to examine the effect of bias voltage on the resulting microstructural properties of the produced coatings. Before the deposition process, the substrate surfaces were subjected to the effects

created by high bias voltages for heating the substrates. This was done by applying 600 V- 800V- 1000 V sequentially. By this process, substrates were cleaned and heated by sputtering and ion bombardment effects. During pretreatment, 600 V and 800 V were applied to alumina for 1 min then 1000 V was applied for 15-45 sec and thereby substrates were heated until 850-950°C. By this way, good adhesion of coatings to the substrates was provided.

Ti coatings were produced on alumina substrates at 0, 100, 200 V bias voltages. Pure titanium targets were used as cathodes during the deposition process. All Ti coatings were produced using direct current (DC) bias mode, using a cathode current of 60 A and 20 sccm argon gas flow rate. The duration of deposition process is 20 min. The SEM images of Ti coatings deposited at 0 V, 100 V, 200 V bias voltages were given in Figure 3.3, Figure 3.4 and Figure 3.5, respectively. Among the Ti coatings produced at different bias voltages, the smoothest surface was obtained from the Ti coating deposited at 0 V. However, in all Ti coating surfaces 1-8 micron sizes spherical features were also observed which is typical to CAPVD coatings [89].

The cross sectional SEM images of Ti coatings deposited at 0 V, 100 V and 200 V illustrated in Figure 3.6, Figure 3.7, and Figure 3.8, respectively. As the deposition bias voltage was increased, the thickness of coating decreased from 7.1 micron to 2.8 micron. Increase of bias during deposition is well known to decrease the deposition rate due to re-sputtering effects induced by higher bias voltages. The increase in bias voltage led to the conversion of coating to more dense structure and decreased thickness of coating.

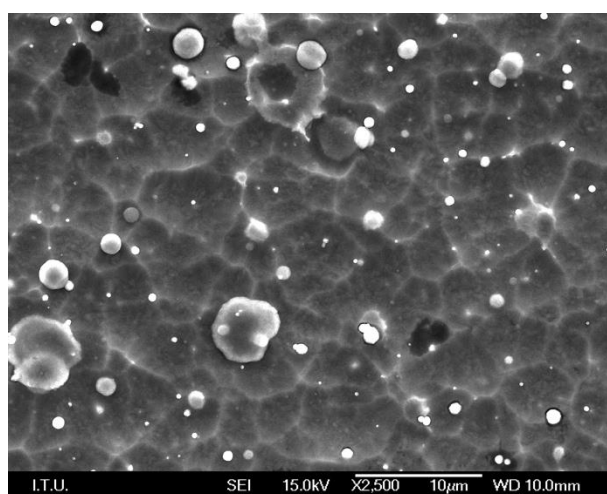


**Figure 3.3 :** The surface SEM image of Ti coating deposited on alumina at 0 V bias voltage using CAPVD technique.

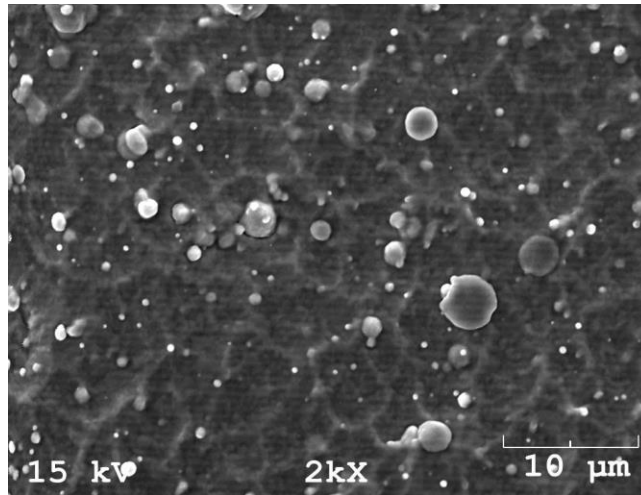


**Figure 3.4 :** The surface SEM image of Ti coating deposited on alumina at 100 V bias voltage using CAPVD technique.

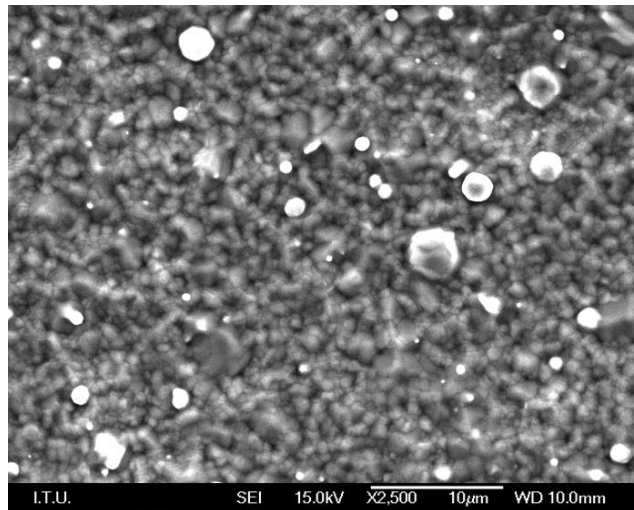


**Figure 3.5 :** The surface SEM image of Ti coating deposited on alumina at 200 V bias voltage using CAPVD technique.

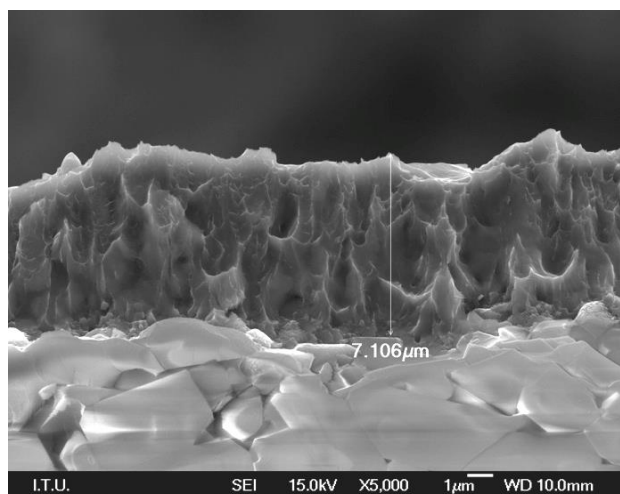


**Figure 3.6 :** The cross sectional SEM image of Ti coating deposited on alumina at 0 V bias voltage using CAPVD technique.



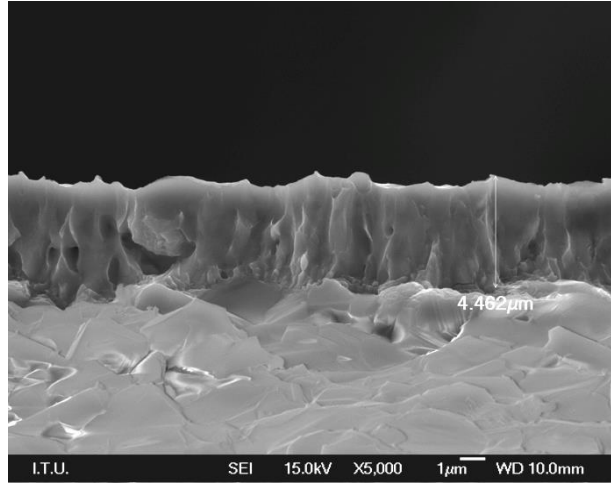


**Figure 3.7 :** The cross sectional SEM image of Ti coating deposited on alumina at 100 V bias voltage using CAPVD technique.

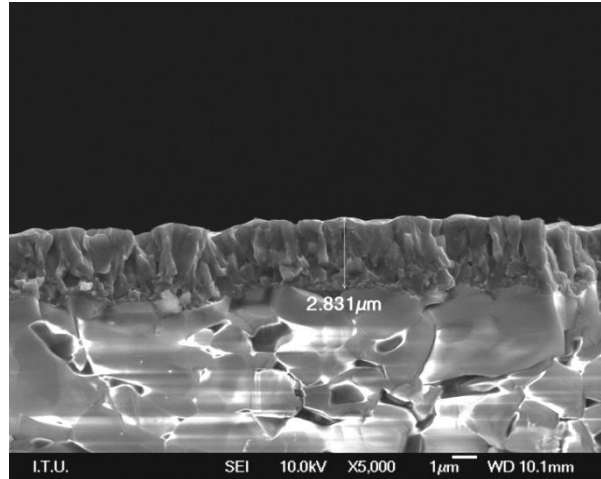


**Figure 3.8 :** The cross sectional SEM image of Ti coating deposited on alumina at 200 V bias voltage using CAPVD technique.

### **3.1.2 The effects of post treatment with high bias voltage on microstructural properties of Ti coating**

At low bias voltages (50-300 V) the deposition process is dominant but at higher bias voltages the deposition process is prevented and the substrate is heated rapidly due to the momentum transfer processes occur during the collision of the accelerated ions to the surface. In order to determine the effect of high bias voltage application on Ti coatings, Ti coatings deposited at 0 V, 100 V, 200 V were exposed to -1000 V for 4 min after the deposition process was completed. High bias voltage application caused heating the materials up to 1300 °C. The heat generated on the surface of coating resulted in the transformation of coating into a more dense structure. The surface SEM images of Ti coatings deposited at 0 V, 100 V, 200 V and successively

subjected to 1000 V were given in Figure 3.9, Figure 3.10, and Figure 3.11, respectively. In 1000 V applied Ti coatings surface smoothness increased compared to the Ti coatings without high voltage application. In addition coating was converted into a equiaxed structure and became much more denser when compared to the ones produced without the application of high voltages. The amount of droplets on the surfaces also decreased with the application of this high bias voltage post treatments.

As it is seen in cross sectional SEM images of Ti coatings deposited at 0 V, 100 V, 200 V, the columnar structure was dissappeared and the structure similar to metallic materials was observed (Figure 3.12, Figure 3.13 and Figure 3.14).

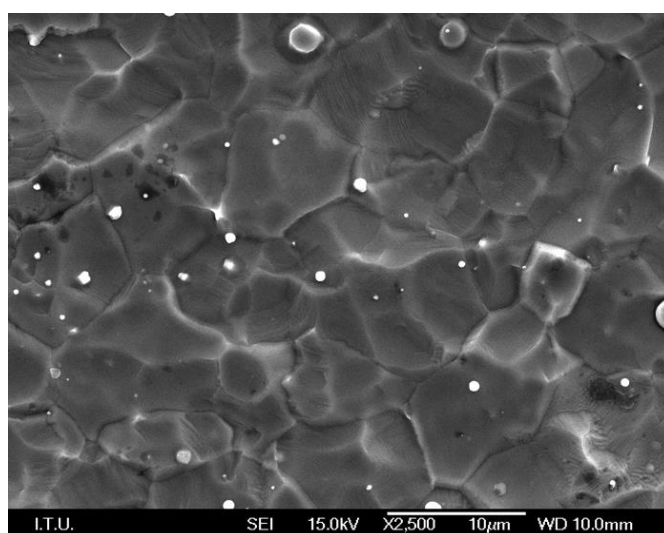


**Figure 3.9 :** SEM image of Ti coating which was deposited on alumina at 0 V bias voltage and then exposed to 1000 V high voltage.

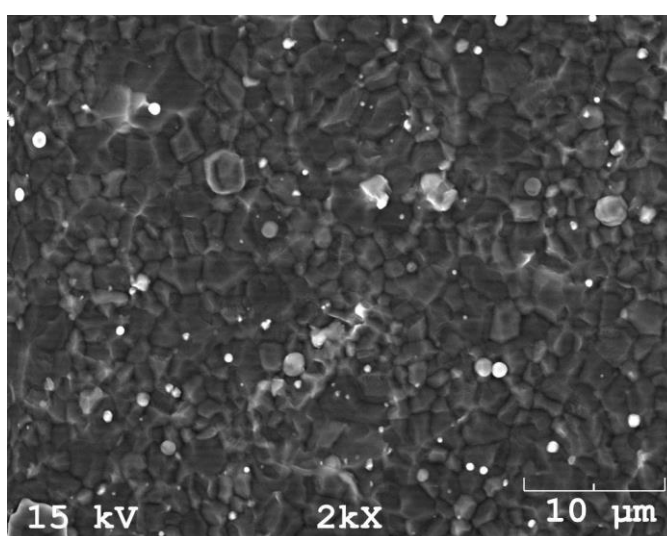


**Figure 3.10 :** SEM image of Ti coating which was deposited on alumina at 100 V bias voltage and then exposed to 1000 V high voltage.

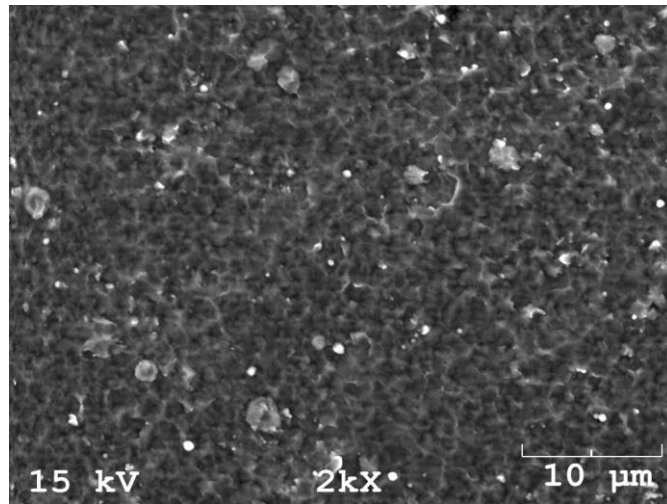


**Figure 3.11 :** SEM image of Ti coating which was deposited on alumina at 200 V bias voltage and then exposed to 1000 V high voltage.

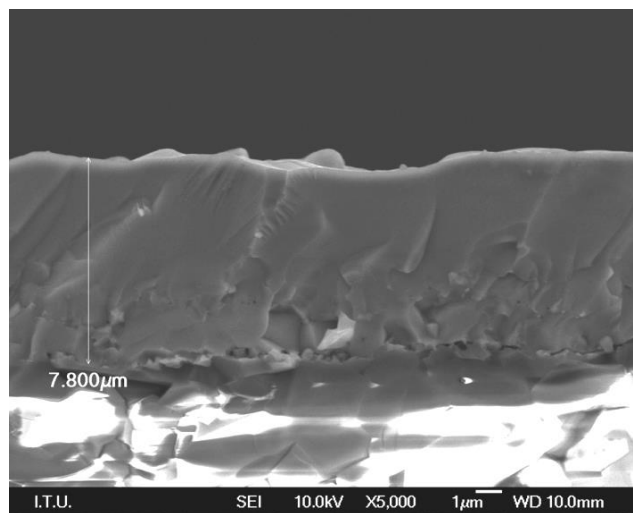


**Figure 3.12 :** Cross sectional SEM image of Ti coating which was deposited on alumina at 0 V bias voltage and then exposed to 1000 V high voltage.

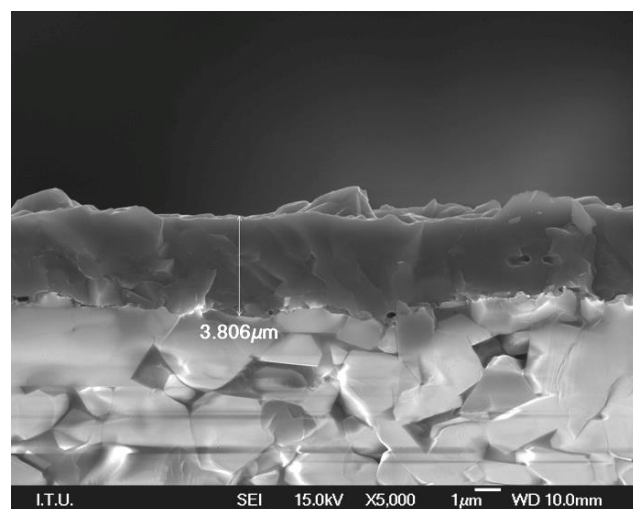


**Figure 3.13 :** Cross sectional SEM image of Ti coating which was deposited on alumina at 100 V bias voltage and then exposed to 1000 V high voltage.

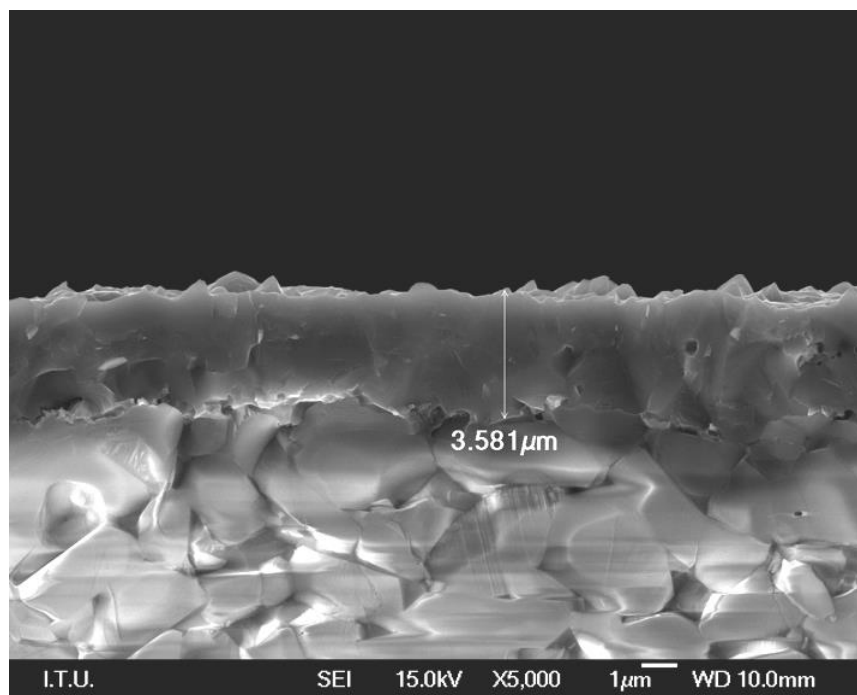


**Figure 3.14 :** Cross sectional SEM image of Ti coating which was deposited on alumina at 200 V bias voltage and then exposed to 1000 V high voltage.

### 3.1.3 The effects of bias voltage on structural properties of Ti coating

In order to determine the structural properties of produced Ti coatings, XRD analyses were performed. By utilizing these analyses, the effects of deposition bias voltage on structures of coatings were examined. The normalized XRD patterns of Ti coatings deposited on alumina at 0, 100, 200 V were compared in Figure 3. 15. The XRD patterns of Ti coatings deposited at 0, 100, 200 V were nearly identical to each other. All these coatings showed completely  $\alpha$ -Ti structure (hexagonal) and without any appreciable shift in their original XRD peak positions. The substrate peaks were indicated by 's' in the patterns.

### 3.1.4 The effects of post treatment with high bias voltage on the structural properties of Ti coating

In order to evaluate the effect of high bias voltage after deposition, the Ti coatings produced at 0 V, 100 V, 200 V were exposed to 1000 V during 4 min and the normalized X-ray diffraction patterns of these coatings were given in Figure 3. 16. All of the coatings subjected to high bias application exhibited similar diffraction patterns. These patterns indicate that the structures were completely  $\alpha$ -Ti. However, in these coatings, the peaks shifted towards lower angles from original  $\alpha$ -Ti peak

positions as seen in Figure 3.17. The most three intense peaks of Ti coatings deposited at 100 V with and without post treatment were compared in Figure 3.18 in high magnification and the measured shift values were about  $0.5^\circ$ . The reason behind this difference aroused from the internal stress formation in high bias voltage applied Ti coatings.

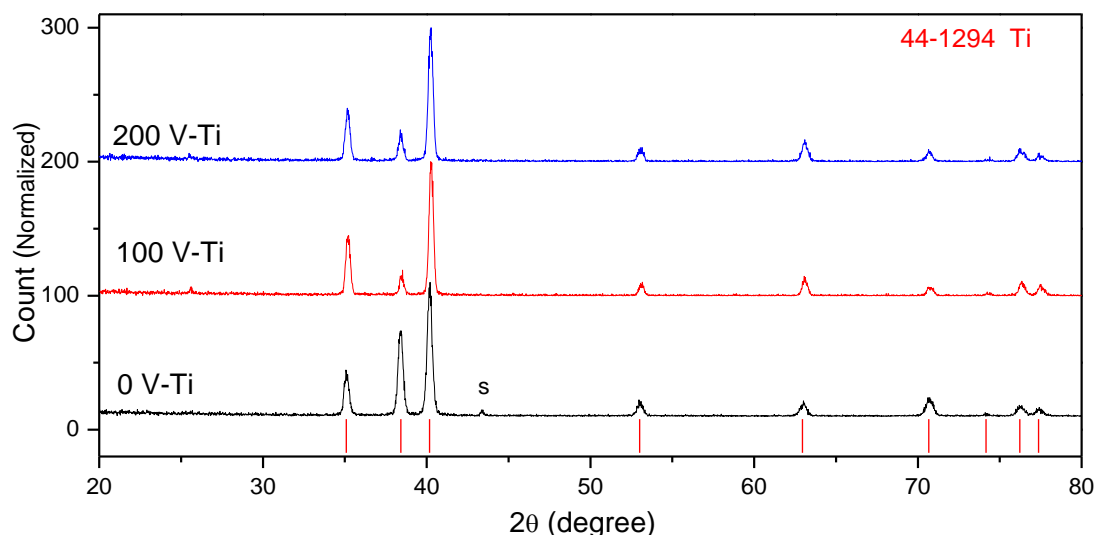


**Figure 3. 15 :** The comparison of normalized XRD patterns of Ti coatings deposited on alumina at 0 V, 100 V and 200 V bias voltage using CAPVD technique. Red lines denote the XRD peak positions taken from PCPDF file 44-1294

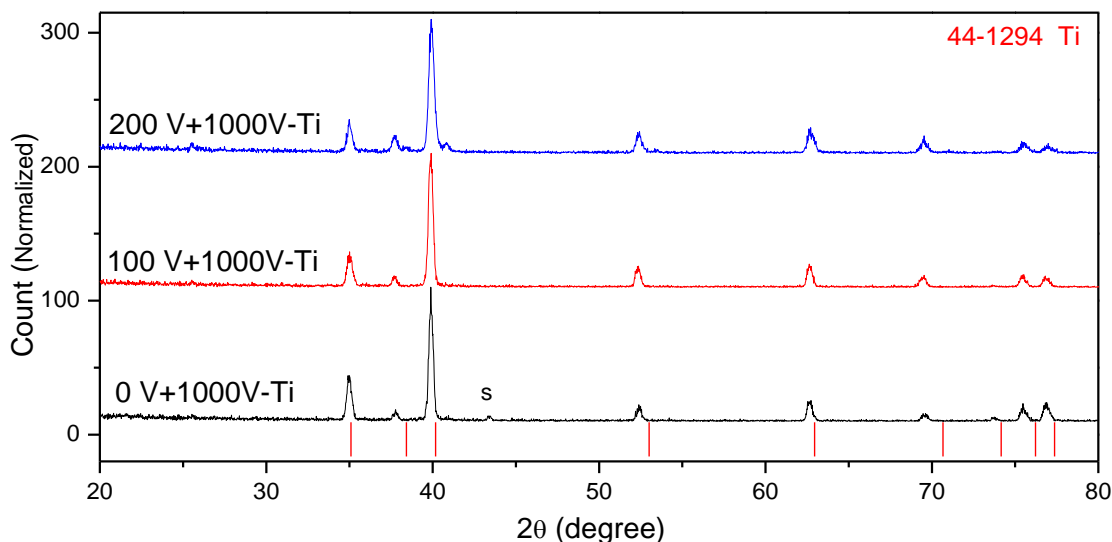


**Figure 3. 16 :** The comparison of normalized XRD patterns of Ti coatings deposited on alumina at 0 V, 100 V and 200 V bias voltage and successively subjected to 1000 V. Red lines denote the XRD peak positions taken from PCPDF file 44-1294

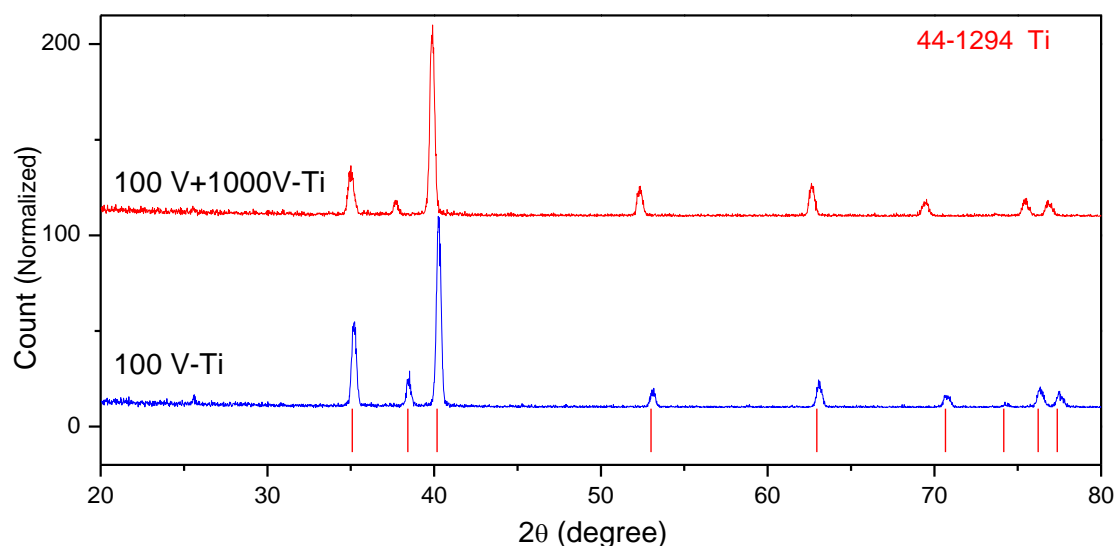


**Figure 3.17 :** Comparison of normalized XRD patterns of Ti coating deposited on alumina at 100 V and 1000 V high bias voltage applied Ti coating deposited at 100 V. Red lines denote the XRD peak positions taken from PCPDF file 44-1294

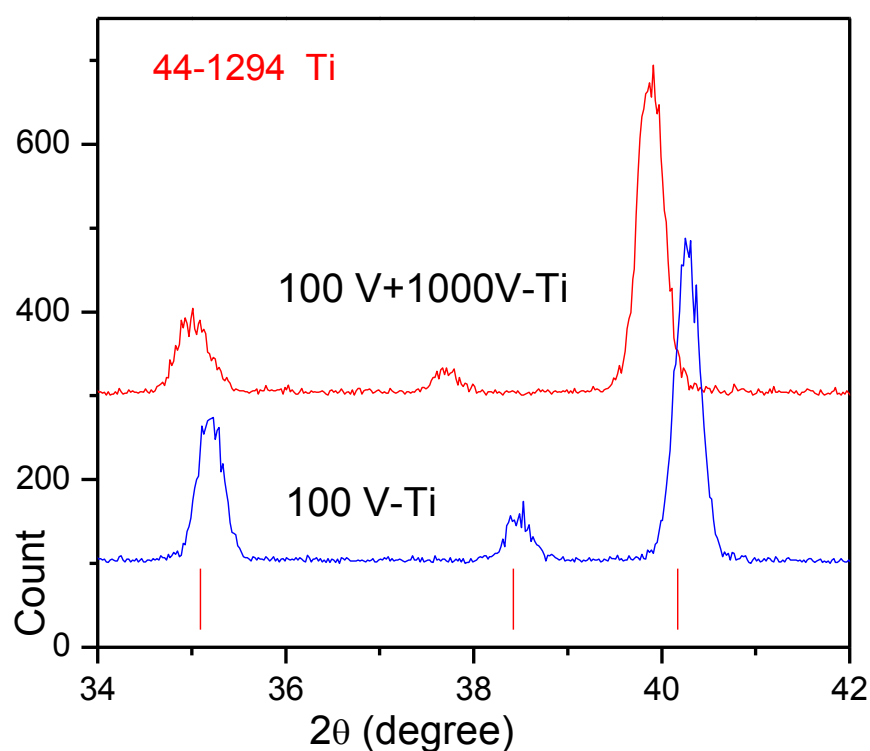


**Figure 3.18 :** Comparison of normalized XRD patterns of Ti coating deposited on alumina at 100 V and 1000 V high bias voltage applied Ti coating deposited at 100 V in high magnification. Red lines denote the XRD peak positions taken from PCPDF file 44-1294

## 3.2 Investigation of the CAPVD Process Parameters for the Deposition of Ti-Al Coatings

### 3.2.1 The effects of bias voltage on microstructural properties TiAl coating

As in Ti coatings, a similar pretreatment process was conducted in the initial stage of TiAl coating in order to heat and clean the surface of substrate. After pretreatment process, the coatings with different properties were produced at 0, 100, 200 bias voltages. All coatings were performed in DC mode using 60 A cathode current for 20 min. During deposition 20 sccm Argon gas flow rate was given to the system. In production of TiAl coatings, a TiAl cathode consisting 25 at% Al was used. As seen SEM images in Figure 3.19, Figure 3.20, and Figure 3.21, surface morphology of the coatings changed depending on the bias voltage. In TiAl coatings deposited at 100V and 200 V bias voltages, a smoother surface morphology was obtained. However, in all TiAl coating surfaces 1-13 micron sizes droplets were also observed owing to the CAPVD method. The droplet amount in TiAl coatings were higher than the ones obtained for pure Ti. This can be attributed to the lower melting temperature of TiAl compared to pure Ti. It is very well known that the number and sizes of the droplets increase in lower melting point elements.

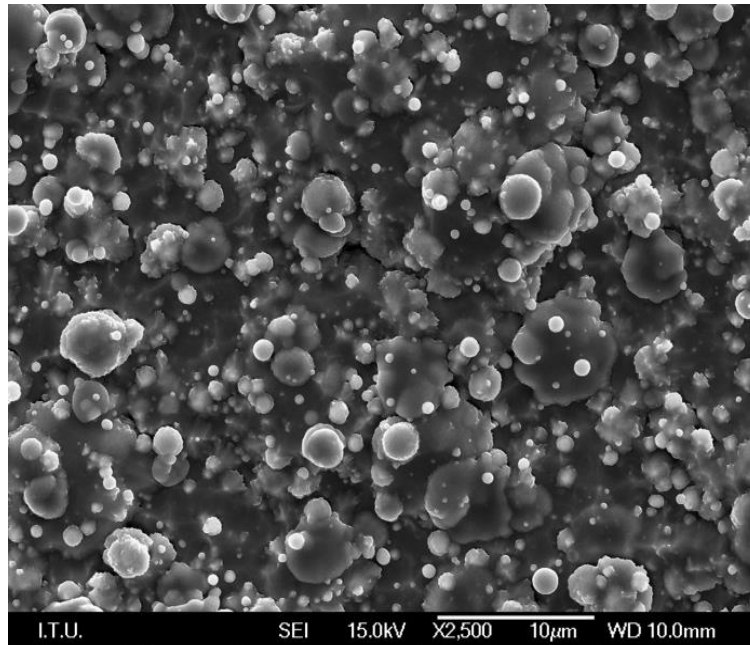


**Figure 3.19 :** The SEM image of TiAl coating deposited on alumina at 0 V using CAPVD technique.

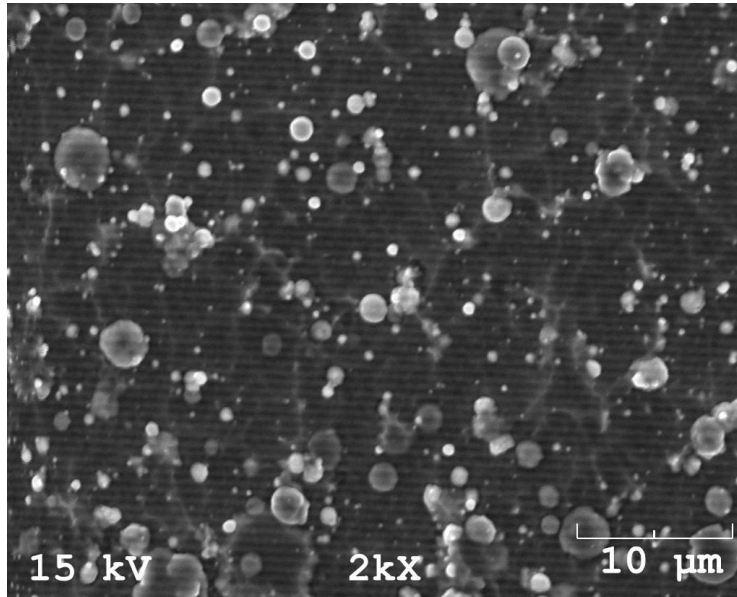


**Figure 3.20 :** The SEM image of TiAl coating deposited on alumina at 100 V using CAPVD technique.

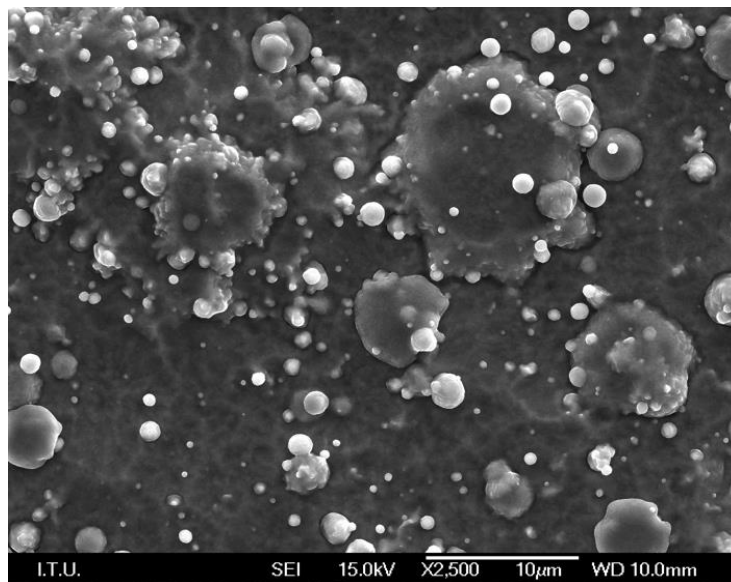


**Figure 3.21 :** The SEM image of TiAl coating deposited on alumina at 200 V using CAPVD technique.

The cross sectional SEM images of coatings deposited at 0 V, 100 V, 200 V were seen in Figure 3.22, Figure 3.23, and Figure 3. 24, respectively. According to these cross sectional SEM images, as the bias voltage was increased, the columnar structure of coating becomes more denser and smoother surfaces were obtained. Considering the relationship between the thickness of the coating with the bias voltage, a decrease in the thickness of coating was observed as the bias voltage was increased. Since the coating became more denser and the re-sputtering effect was increased by increasing the voltage, the thickness of coating was decreased.



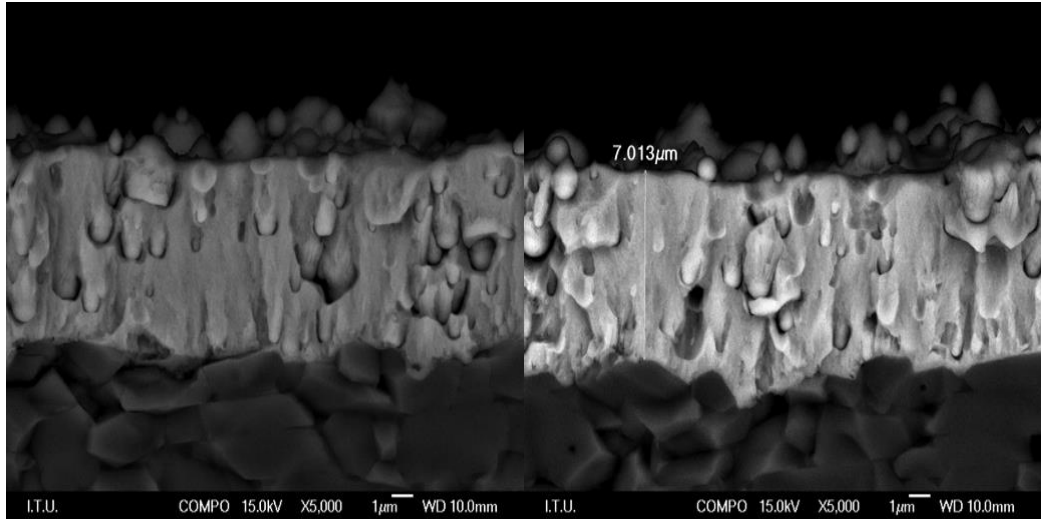


**Figure 3.22 :** The cross sectional SEM image of TiAl coating deposited on alumina at 0 V using CAPVD technique

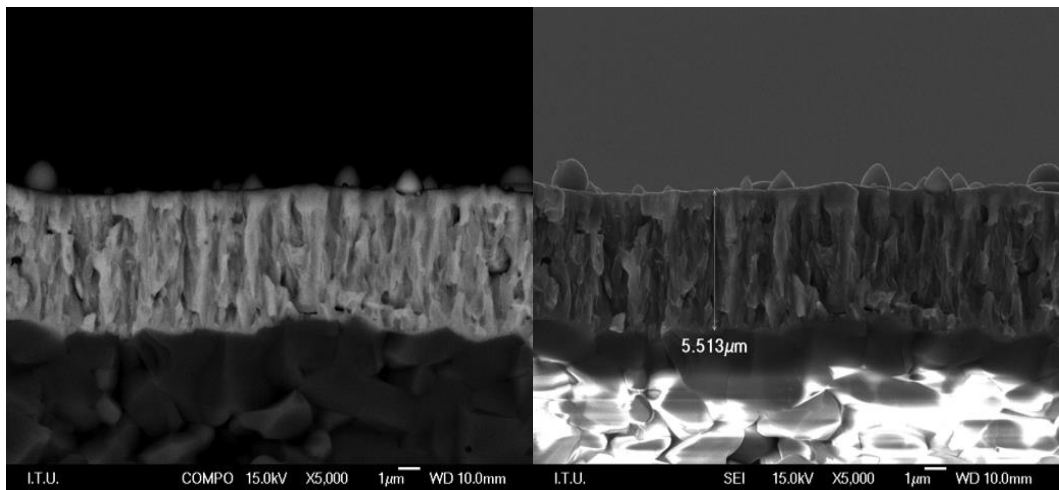


**Figure 3.23 :** The cross sectional SEM image of TiAl coating deposited on alumina at 100 V using CAPVD technique

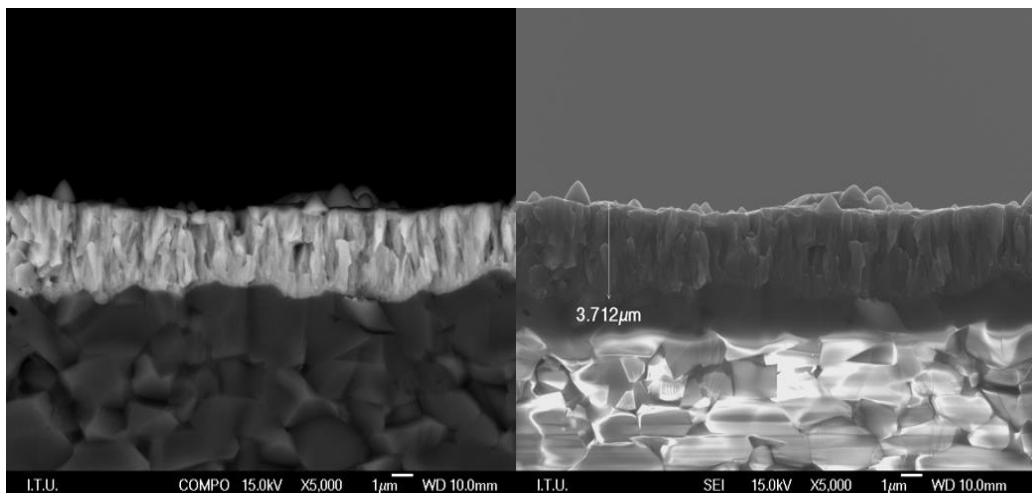


**Figure 3. 24 :** The cross sectional SEM image of TiAl coating deposited on alumina at 200 V using CAPVD technique

It was also determined that the applied bias voltage was effective on the coating composition. According to EDS analysis results given in Table 3.1, the amount of Al in TiAl coating varies inversely with the applied voltage. The amount of Al in TiAl coating deposited at 0 V and the content of the target material used are approximately similar. However, as the bias voltage increases the amount of Al in TiAl is decreased due to the higher sputtering rate of Al.

**Table 3.1 :** The EDS analyses of TiAl coatings deposited at 0 V, 100 V, 200 V bias voltages.

Coating	Atomic % Al	Atomic % Ti
TiAl coating deposited at 0 V bias voltage	23	77
TiAl coating deposited at 100 V bias voltage	15	85
TiAl coating deposited at 200 V bias voltage	11	89

### **3.2.2 The effects of post treatment with high bias voltage on microstructural properties TiAl coating**

In order to examine the effects of high bias voltage on produced coatings, TiAl coatings were deposited at 0, 100, 200 V bias voltages and 1000 V high voltage was applied to these coatings for 4 min at the end of deposition. The materials were heated up to 1300 °C when they were exposed to high bias voltage. The heating generated on the coating's surface allow the coating to turn into a more dense structure. In Figure 3.25, Figure 3.26, and Figure 3.27, the SEM images of TiAl coatings which were deposited at 0, 100, 200 V and successively exposed to high bias voltage were given respectively. In 1000 V bias voltage applied coatings surface morphologies were improved compared to the coatings without high voltage application.

The cross sectional SEM images of TiAl coating deposited at 0 V, 100 V, 200 V and successively subjected to 1000 V high bias voltage were given in Figure 3.28, Figure 3.29, and Figure 3.30, respectively. The structure of 1000 V applied coatings showed a similar structure with metallic materials.

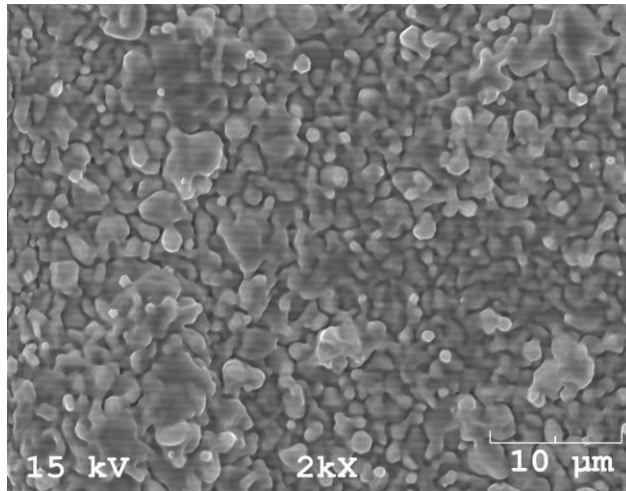


**Figure 3.25 :** The SEM image of TiAl coating deposited on alumina at 0 V and then subjected to 1000 V high bias voltage

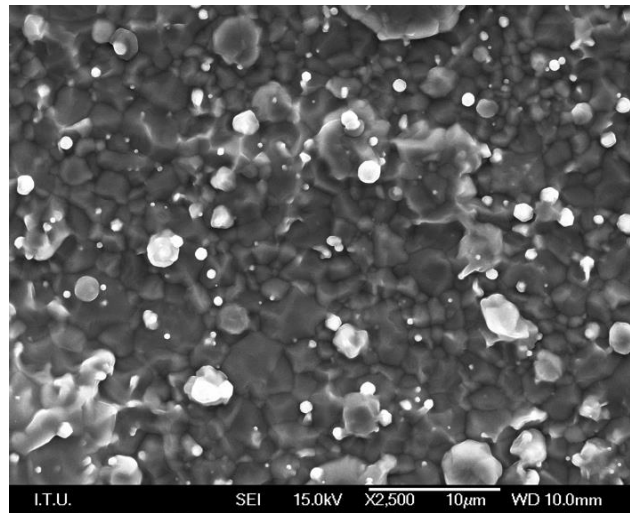


**Figure 3.26 :** The SEM image of TiAl coating deposited on alumina at 100 V and then exposed to 1000 V high bias voltage

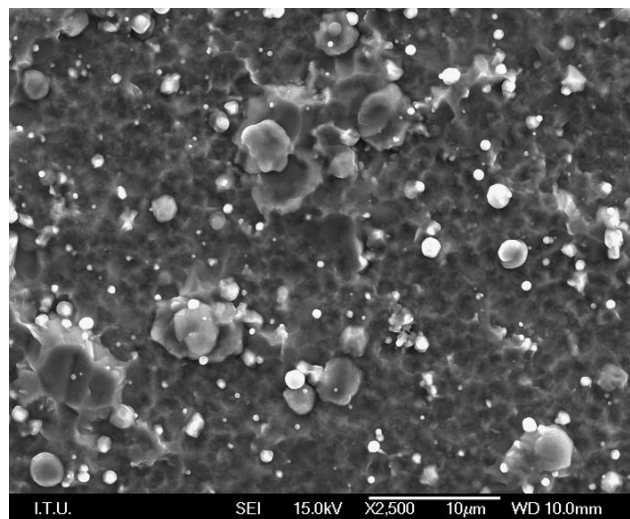


**Figure 3.27 :** The SEM image of TiAl coating deposited on alumina at 200 V and then subjected to 1000 V high bias voltage

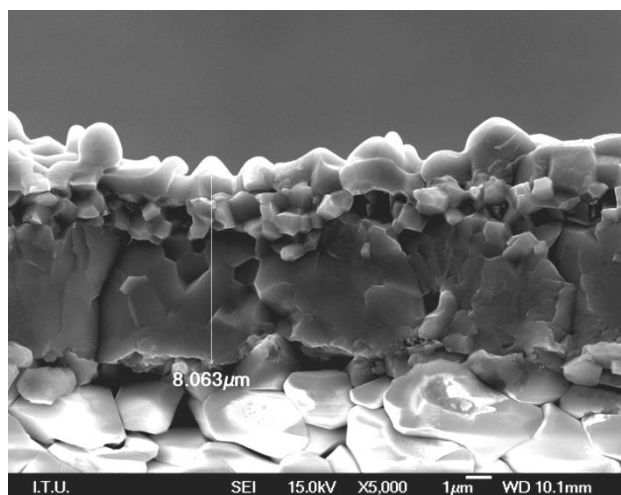


**Figure 3.28 :** The cross sectional SEM image of TiAl coating deposited on alumina at 0 V and then exposed to 1000 V high bias voltage

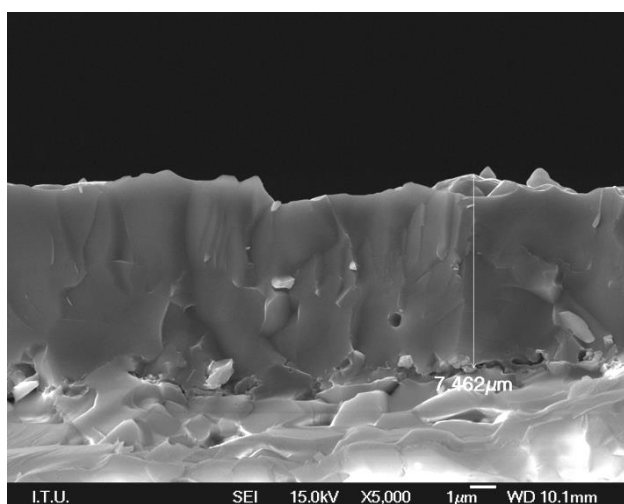


**Figure 3.29 :** The cross sectional SEM image of TiAl coating deposited on alumina at 100 V and then exposed to 1000 V high bias voltage

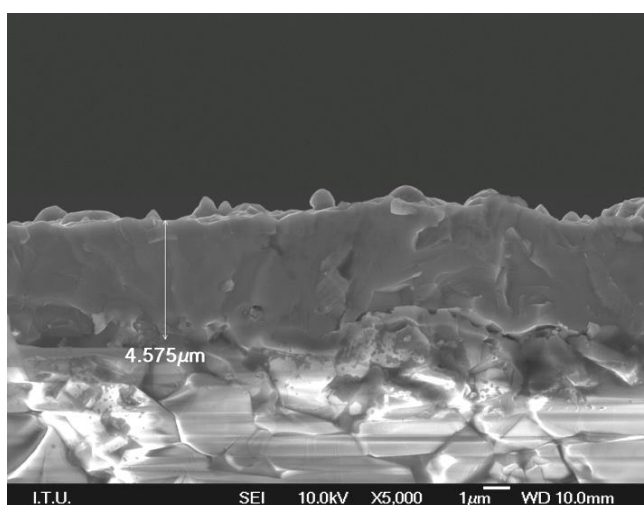


**Figure 3.30 :** The cross sectional SEM image of TiAl coating deposited on alumina at 200 V and then exposed to 1000 V high bias voltage

The influence of post treatment on the coating composition was also examined using EDS analysis. According to these results given in Table 3.2, the amount of Al in TiAl coating varies in the range between 12-15 at % depending on applied bias voltage before post treatment, highly probably due to the compositional homogenization effects through accelerated diffusion at high temperatures.

**Table 3.2 :** The surface EDS analyses of TiAl coatings deposited at 0 V, 100 V, 200 V bias voltage and successively subjected to post treatment with high bias voltage.

Coating	Atomic % Al	Atomic % Ti
After 1000 V application of TiAl coating deposited at 0 V bias voltage	19	85
After 1000 V application of TiAl coating deposited at 100 V bias voltage	12	88
After 1000 V application of TiAl coating deposited at 200 V bias voltage	15	85

### 3.2.3 The effects of bias voltage on structural properties TiAl coating

XRD analyses were performed in order to define the structural properties of TiAl coatings. By using these XRD analyses, the effects of deposition bias voltage and also the influence of Al alloying on the structure of Ti coating were investigated and evaluated. In the XRD spectra of the coatings that were produced with the application of 0 V and 100 V, the peaks are broader and additional small peaks belonging to  $Ti_3Al$  phase are present. In the XRD spectrum of the sample produced by the application of -200 V bias peaks are sharper and contribution of  $Ti_3Al$  peaks to the spectrum are not as pronounced as the ones produced by using lower bias voltages. According to the Ti-Al binary phase diagram there is 11 at % solubility of aluminum in titanium. Beyond this concentration  $Ti_3Al$  phase should appear in the structure under equilibrium conditions as seen in Al-Ti binary diagram (Figure 3.31). Samples produced under 0 and 100 V bias voltage have higher than 11 at % Al thus presence of  $Ti_3Al$  phase in their structure is expected. The broad peaks that appear in the range of  $35^\circ$ - $42^\circ$  are composed of diffraction belonging to both alpha Ti and  $Ti_3Al$  (Figure 3.32). We may conclude that the phases are not well crystallized since the peaks belonging to different phase are well-defined and broad. On the other hand in cathodic arc PVD deposited alloys the presence of segregation is a very well

known fact [62,90,91]. This segregation mainly arises from the droplets. Droplets are macro particles that are converted to vapor during CAPVD thus their composition is very close to the target material and not the same as the deposited film. Therefore, segregation presence of films with uneven composition should be expected for CAPVD metallic alloy films.

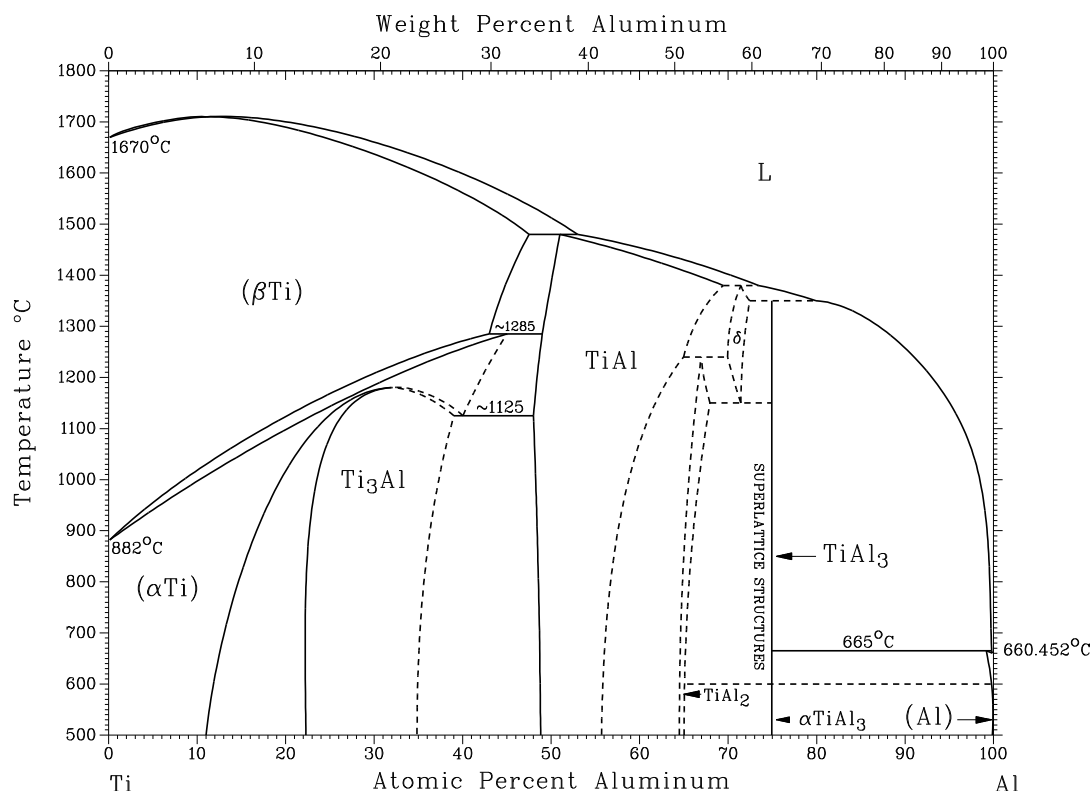


**Figure 3.31 :** Al-Ti binary phase diagram [92].

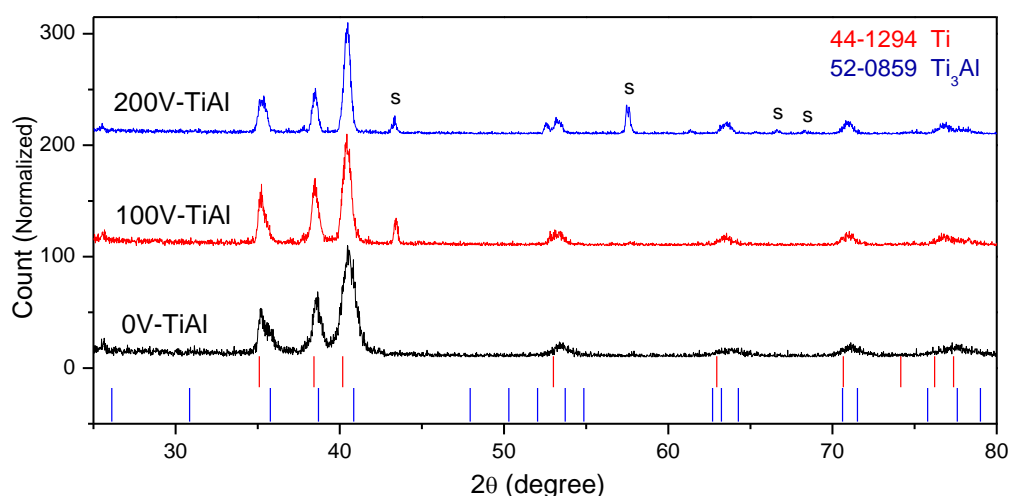


**Figure 3.32 :** The normalized XRD patterns of TiAl coatings deposited on alumina at 0 V, 100 V and 200 V bias voltage using cathodic arc method. Red lines and blue lines denote the XRD peak positions taken from PCPDF file 44-1294 and 52-0859, respectively.

### 3.2.4 The effects of post treatment with high bias voltage on structural properties TiAl coating

After post treatment of the coatings by the application of high bias voltage the crystallinity of the coatings increased and peaks belonging to alpha Ti and Ti<sub>3</sub>Al phases became well defined (Figure 3.33). Since the amount of Al concentration in TiAl coating produced at 0 V was higher than 22 at % Al, its structure completely transformed into Ti<sub>3</sub>Al after post treatment. In Figure 3.34, the normalized XRD patterns of post treated TiAl coatings deposited at 0 V and 200 V were compared in order to indicate Ti<sub>3</sub>Al phase formation in TiAl coating deposited at 0 V after post treatment. Other than that the differences observed in the Al content of untreated samples was not present in the post treated samples, since through the heating of the samples accelerated diffusion process not only densified the structure but also homogenized the chemical composition. The amount of Al in TiAl coatings deposited at 100 V and 200 V varies in the range between 12-15 at % after post treatment.

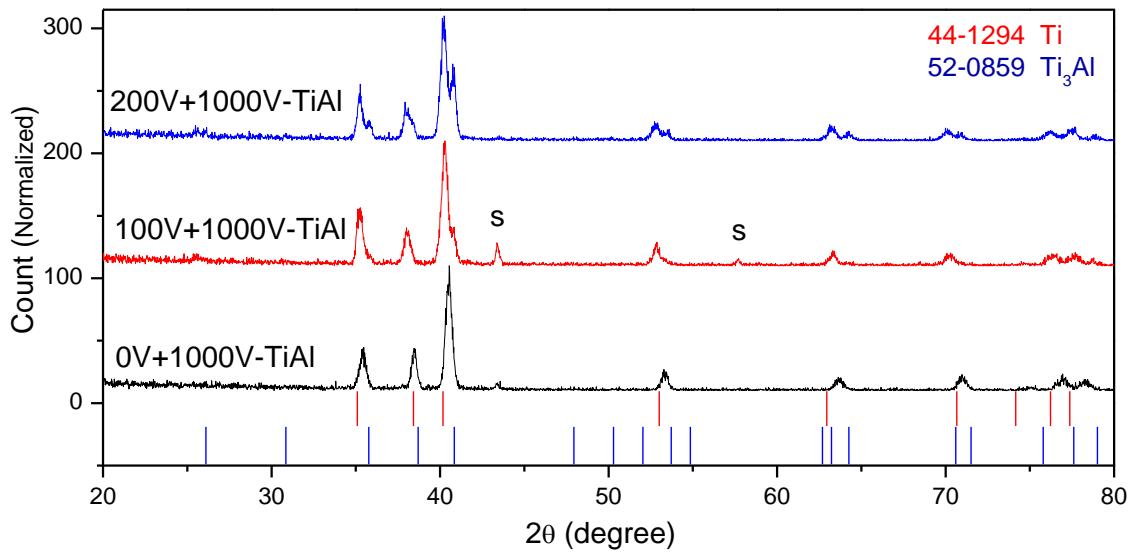


**Figure 3.33 :** The comparison of normalized XRD patterns of TiAl coatings deposited on alumina at 0 V, 100 V and 200 V bias voltage and successively subjected to 1000 V. Red lines and blue lines denote the XRD peak positions taken from PCPDF file 44-1294 and 52-0859, respectively.

In all produced TiAl coatings, the peaks shifted about 0.2°-0.3° towards higher angles from the original  $\alpha$ -Ti peak positions since addition of Al caused a decrease in lattice parameters. However, in post treatment applied TiAl coatings, there were also peak shifts towards lower angles due to the internal stress induced from high bias

voltage (Figure 3.35). The most three intense peaks of TiAl coatings deposited at 100 V with and without post treatment were compared in Figure 3.36 in high magnification. In post treatment applied TiAl coatings, the measured peak shift values were in the range of  $0.1^{\circ}$ - $0.5^{\circ}$  with respect to TiAl coating deposited at 100 V.

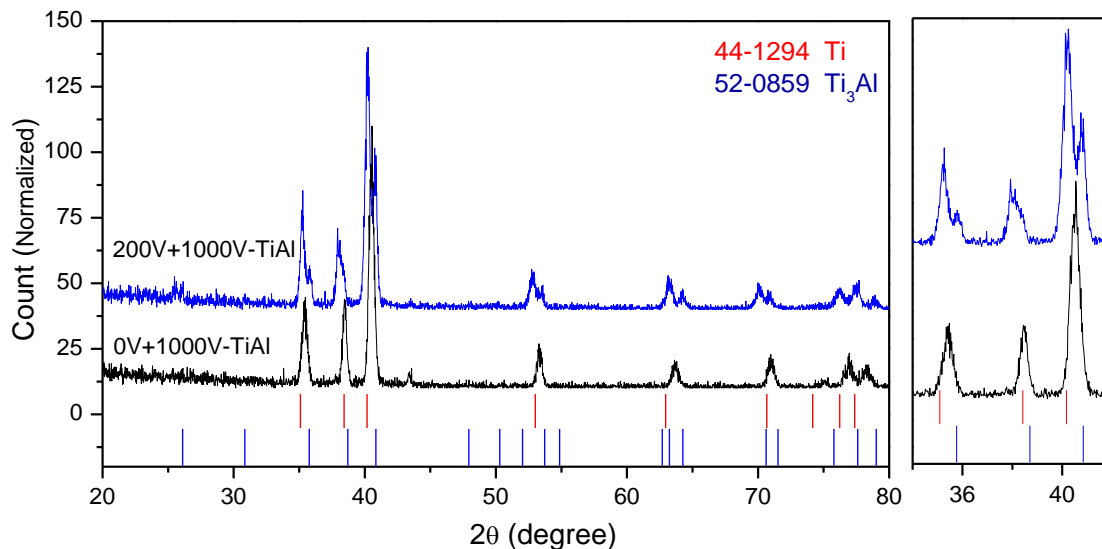


**Figure 3.34 :** The comparison of normalized XRD patterns of TiAl coatings deposited on alumina at 0 V and 200 V bias voltage and successively subjected to 1000 V. Red lines and blue lines denote the XRD peak positions taken from PCPDF file 44-1294 and 52-0859, respectively.

As a result of all these investigations, well-adherent and dense metallic Ti and TiAl thin films were deposited on alumina substrates using CAPVD method. In the pretreatment process, the heat that was generated on the surface of substrates by the effect of energetic ions and this heating provided good adhesion between substrate and coating. The main effects of different deposition bias voltage and post treatment applications on the resulting coating structures were summarized as in the below:

#### For Ti coatings:

- The surface morphologies of coatings altered with the increase in bias voltage. As the deposition bias voltage was increased, the columnar structure of coatings became more denser and a decrease in the thicknesses of Ti coatings was observed.



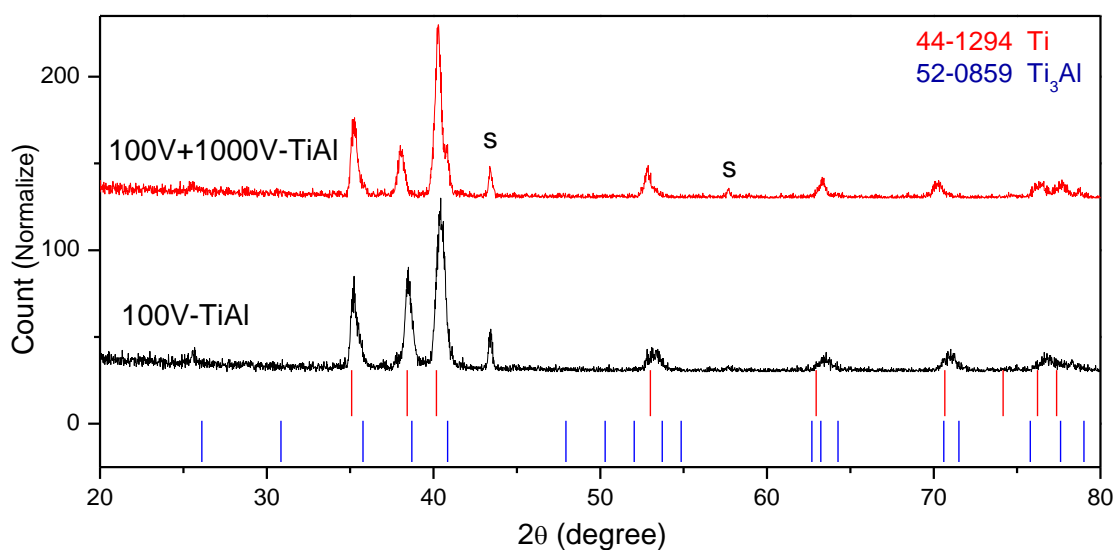


**Figure 3.35 :** Comparison of normalized XRD patterns of TiAl coating deposited at 100 V and TiAl coating deposited at 100 V successively applied 1000 V high voltage. Red lines and blue lines denote the XRD peak positions taken from PCPDF file 44-1294 and 52-0859, respectively.

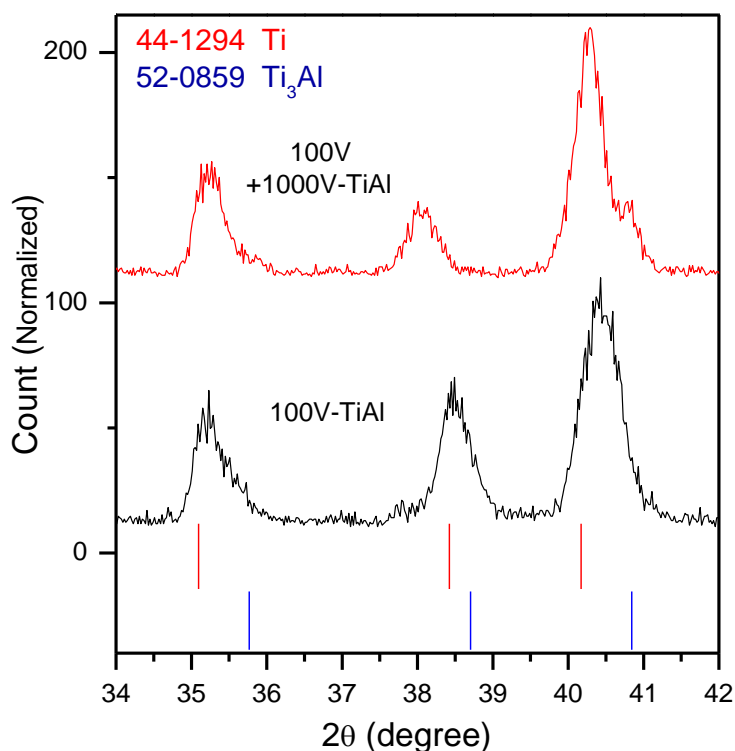


**Figure 3.36 :** Comparison of normalized XRD patterns of TiAl coating deposited on alumina at 100 V and 1000 V high bias voltage applied TiAl coating deposited at 100 V in high magnification. Red lines and blue lines denote the XRD peak positions taken from PCPDF file 44-1294 and 52-0859, respectively.

- There was no apparent effect of bias voltage increase on XRD patterns of Ti coatings.
- The high bias voltage applied during post treatment caused a heating on the surface of Ti. The columnar structure of coatings was converted into equiaxed structure by the effect of post treatment with high bias voltage. Surface morphologies of coatings were improved compared to the coatings without post treatment and smoother surfaces were obtained. However, droplet formation was observed on the coating surfaces induced from production method.
- After post treatment the peak positions of Ti shifted to lower angles indicating internal stress build up as a result of this treatment.

Among the coatings produced, two types of Ti coatings are selected for the optimization of anodization studies. As the first coating, we have selected coatings produced at -100V bias since among the coatings produced without post treatment these coatings gave an optimum coating thickness and relatively dense structure. As the second coating, we have selected the post treated version of the coating that was produced at -100 V. Although the post treated coatings had a denser structure similar to metallic titanium, we also wanted to check the possible effects induced by internal stresses on the quality of the porous anodized structures.

#### **For Ti-Al coatings:**

- The aluminum content of the films showed dependence on the bias voltage. Coatings produced with 0 V bias voltage had a similar Al content as the target material (25 at %). The aluminum content decreased to a level 11-15 at% by the increase of bias voltage.
- Similar to Ti coatings increase in bias voltage resulted in decrease in coating thickness.
- In the XRD patterns of these coatings presence of  $\text{Ti}_3\text{Al}$  phase was detected. The amount of this phase increased with the aluminum content. The rapid heat treatment supplied by the application of high bias voltage led to stabilize the meta-stable  $\text{Ti}_3\text{Al}$  phase in TiAl coatings.
- Post treatment of the coating resulted in the densification of the coating structure. TiAl coatings surface smoothness increased compared to the TiAl

coatings without post treatment. However, high bias voltage post treatment caused an internal stress formation in Ti and TiAl coatings.

Among the coatings produced, two types of Ti-Al coatings are selected for the optimization of anodization studies. As the first coating, we have selected coatings produced at -100V bias without post treatment since this coating gave an optimum coating thickness, relatively dense structure and also its structure mainly composed of alpha Ti (Ti-Al solid solution). Considering the volume expansion occurs during the anodization process, the relatively dense and columnar structure of this coating was thought to be better for nanoporous structure formation. As the second coating, we have selected the post treated version of the coating that was produced at -100 V. This post treated coating had a denser and equiaxed structure that favors the formation of highly ordered nanoporous structure, however, we also wanted to check the possible effects induced by internal stresses on the quality of the porous anodized structures.



#### **4. OPTIMIZATION OF PROCESS PARAMETERS FOR THE ANODIZATION OF Ti AND TiAl COATINGS**

As explained in section 3, two types of Ti and TiAl coatings were selected for using in the optimization experiments of anodization process parameters of Ti and TiAl films. These are the coatings produced at -100 V bias voltage with and without high bias voltage post treatment. It was considered that high voltage post treatment applied coatings would give well-ordered nanoporous structure due their equiaxed structure and smoother surfaces. On the other hand, the columnar structure was thought to be better for mechanical integrity of nanoporous structure formation since this structure may allow the volume expansion that may occur during the anodization process. Therefore, the suitability and durability of these two different Ti and TiAl coating structures were tested for anodization process. The influences of different coating structures on nanoporous structure formation were examined and the most appropriate coating structures for anodization process were determined.

The denser structure, well adhesion and morphology of the coatings produced by cathodic arc technique are expected to favour the homogenous electric field distribution on the surface and the formation of ordered nano tubular- porous structure [31, 69]. However, droplet formation on the coating surfaces, which is typical in CAPVD method, is a drawback for the formation of homogeneous nano tubular-porous structures. These defects present as asperities on the surface and effect the current distribution during anodization unfavourably leading to an uneven surface after anodization as seen in Figure 4.1.

For overcoming the detrimental effects of droplets on electrochemical reactions during anodization process, the coatings were subjected to pretreatments before anodization process. The surfaces of Ti and TiAl coatings were chemically polished for a few seconds in a mixed solution of HF, H<sub>2</sub>O and HNO<sub>3</sub>. This process was sufficient for the removal of droplets from Ti surfaces however additional mechanical polishing was required for TiAl coatings because of the higher amount of droplets on their surfaces. The surface of TiAl coated samples were mechanically

polished using 320, 500, 800, 1000, 1200, 2400, 4000 grid SiC sand papers sequentially.

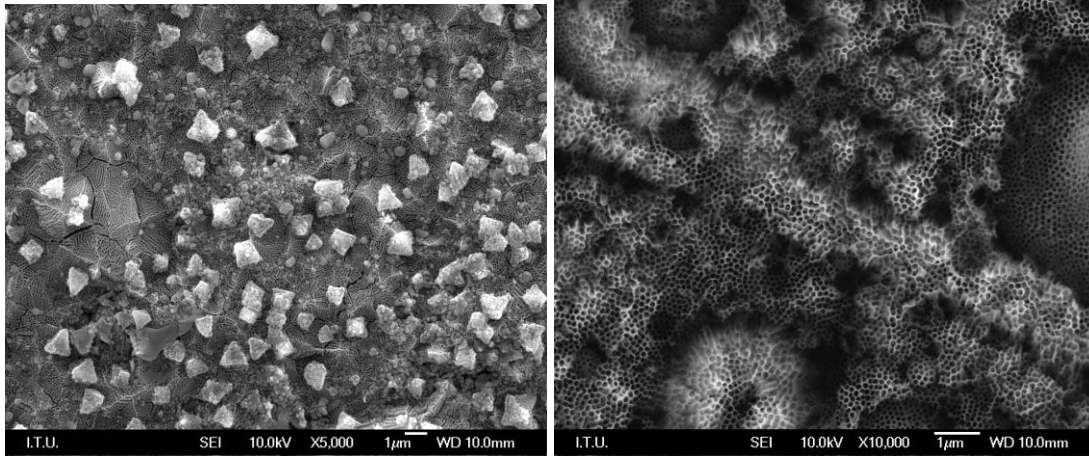


**Figure 4.1 :** The SEM image of anodically oxidized TiAl coatings which have higher amount of droplets on their surfaces.

After anodization process, the Pt is deposited on the surface of nanostructured sensor material to serve as electrical contacts. However, in the preliminary studies conducted in our group and other studies [68] revealed that Pt may diffuse through the nanotube structure and contact with the metallic thin film underneath the nanotubes which may lead to short circuits. Thus the optimization of anodization process mainly aimed to overcome this problem by:

1. Producing long nanotubular structures (above 10  $\mu\text{m}$ ) for preventing the diffusion of Pt to the bottom (barrier layer) of the nanotubes
2. Total anodization of the metallic films above alumina substrate in order to oxidize the metallic film that leads to short-circuiting by the diffusion of Pt.

#### **4.1 Optimization of Process Parameters for the Anodization of TiAl Coatings**

There are many studies in the literature on porous anodization of titanium (see section 1.5). By referring to these studies it is possible to tune the anodization parameters in accordance to the desired nanotubular structure. According to these studies and our previous experience, for obtaining long tubes usage of ethylene glycol based electrolytes is required. Thus for the anodization studies this electrolyte is selected. Again based on the available literature  $\text{NH}_4\text{F}$  and water content, duration, temperature and anodization voltages are the other parameters that show effect on the formation of nanoporous layers on titanium. However, there are no studies on the

literature on the anodization of Ti-Al alloy thin films. A few studies exist on the anodization of bulk TiAlV and TiAlNb alloys mainly considering the possible usage of these anodized materials for biomedical applications. For this purpose, the optimization studies are mainly conducted by using TiAl alloy coatings since there are no studies about the anodization of these coatings in the literature. In anodization of TiAl thin film coatings, various anodization voltages, electrolyte compositions, temperatures, agitation types and durations were attempted. The effects of these parameters on the morphologies and diameters of nanotubular structures were also investigated and evaluated. The optimal anodization parameters for obtaining high thickness of nanotube layer and well-aligned nanotube arrays were determined.

Before starting the optimization, our hypothesis on the durability of Ti based coatings produced by CAPVD in anodization electrolyte is tested by anodizing a Ti coated sample in ethylene glycol based electrolyte. The results revealed that it is possible to anodize titanium coated alumina in this electrolyte without any spalling. A continuous metallic film is obtained without any delamination as seen in cross sectional SEM image in Figure 4.2.

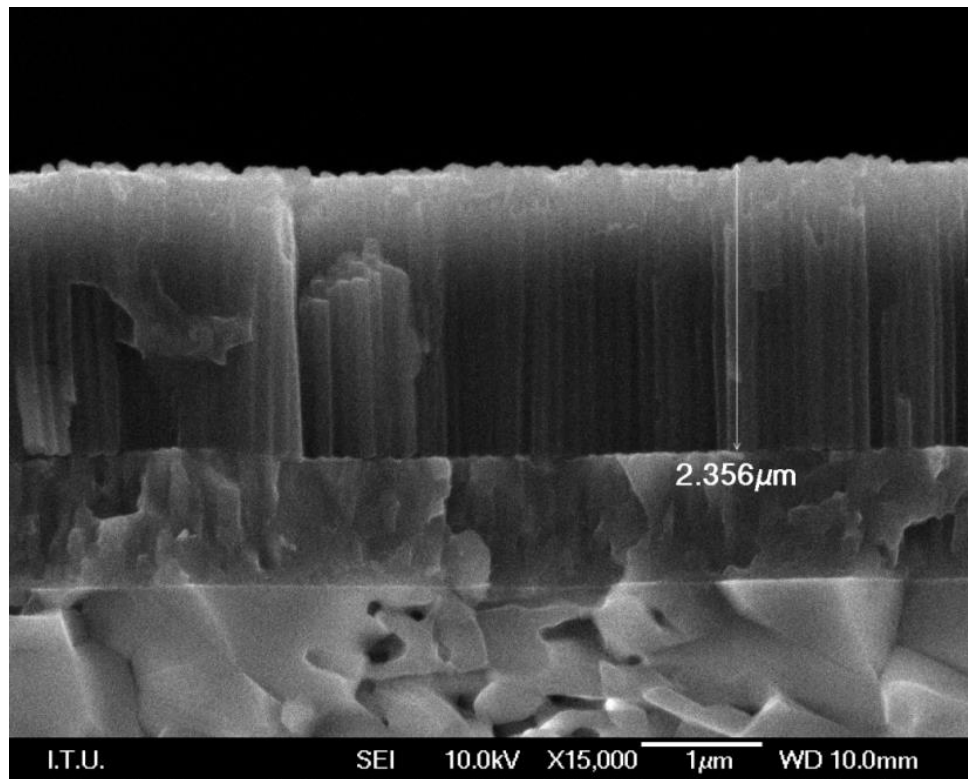


**Figure 4.2 :** The cross sectional image of anodically oxidized Ti coated alumina in ethylene glycol without any spalling.

#### 4.1.1 The effect of electrolyte composition

Ethylene glycol consisting  $\text{NH}_4\text{F}$  was selected as an anodization electrolyte for optimizing the anodization process parameters of TiAl coatings. By using this nonaqueous electrolyte, the thickness of  $\text{TiO}_2$  nanotube arrays can be significantly increased. This is because, in the nonaqueous electrolyte, the mobility of the fluorine ion was largely suppressed; thus, the chemical dissolution of  $\text{TiO}_2$  was decreased [7]. In literature, electrochemical oxidation of titanium has been studied in sulfuric acid, phosphoric acid, acetic acid with or without HF solution [6]. However, at lower pH (HF electrolytes or acidic HF mixtures), the length of the nanotube length was limited by higher dissolution rate [6, 80]. By using buffered neutral electrolytes containing NaF or  $\text{NH}_4\text{F}$  and taking into account the importance of the pH gradient within the tube, the thickness of grown Ti nanotubes can be increased [19].

Initially, electrolyte concentration experiments were conducted due to the most appropriate electrolyte compositions were required for growing well-ordered nanotubes and nanotubes with higher thickness. Since the fluoride concentration mainly determines the kinetics of nanotube growth, the ethylene glycol electrolytes including vol % 1  $\text{H}_2\text{O}$  and different amounts of  $\text{NH}_4\text{F}$  (0.18 wt % , 0.25 wt % , 0.32 wt % , 0.40 wt % , 0.47 wt % , 0.54 wt % , 0.61 wt %) were prepared. Then TiAl coated substrates were anodized by applying constant potential of 40 V at 13 °C for 120 minutes (In the preliminary studies, the suitable ranges of anodization parameters were determined for obtaining the nanotubular/nanoporous structures in the used electrolyte compositions). The resulting average nanotube lengths were 3.8, 4.5, 4, 3.1, 2.4, 1.9, 1.4 microns respectively for 0.18 wt % , 0.25 wt % , 0.32 wt % , 0.40 wt % , 0.47 wt % , 0.54 wt % , 0.61 wt %  $\text{NH}_4\text{F}$  containing ethylene glycol electrolytes. The relation between nanotube length and  $\text{NH}_4\text{F}$  concentration was also depicted in Figure 4.3. Among these concentrations, the highest thickness of nanotube layer was obtained in 0.25 wt %  $\text{NH}_4\text{F}$  containing electrolyte as shown in Figure 4.4. Above this concentration, the nanotube length began decrease since the rate of nanotubes dissolution was higher than their growth rate in high  $\text{NH}_4\text{F}$  concentration. Finally, the shortest nanotube length was formed in 0.61 wt %  $\text{NH}_4\text{F}$  containing electrolyte and the length of as-grown nanotubes were approximately 1-1.5 micron as seen in Figure 4.5.



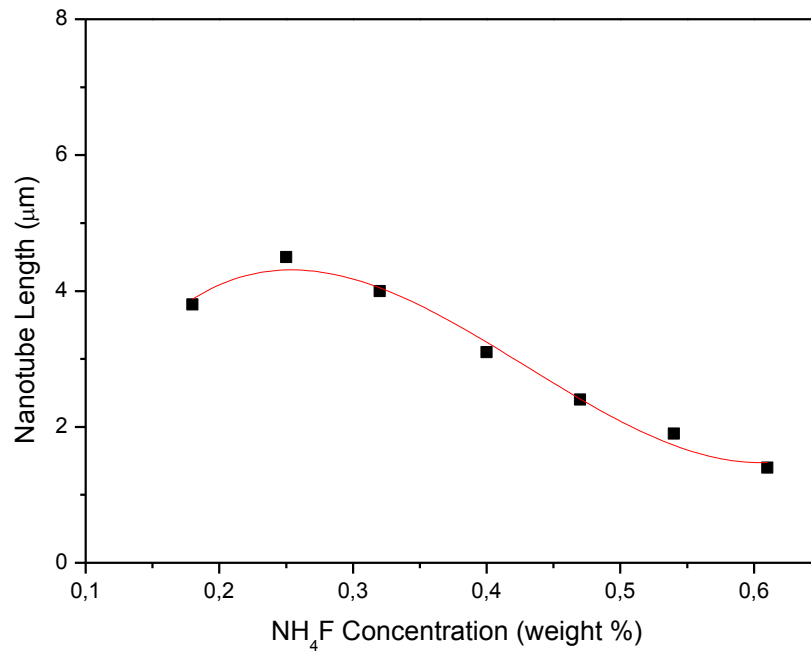


**Figure 4.3 :** The relationship between  $\text{NH}_4\text{F}$  concentration in ethylene glycol electrolyte and nanotube in anodization process conducted at 40 V and 13°C.

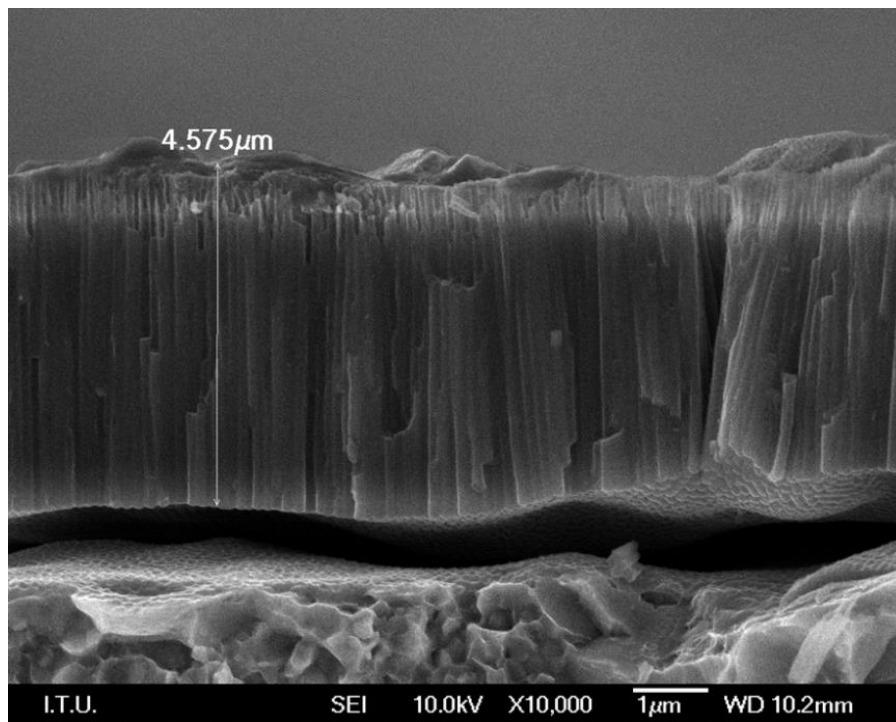


**Figure 4.4 :** The cross sectional SEM image of nanotubular structure formed on TiAl coating after the anodization process conducted at 40 V and 13 °C in ethylene glycol containing 0.25 wt %  $\text{NH}_4\text{F}$ .

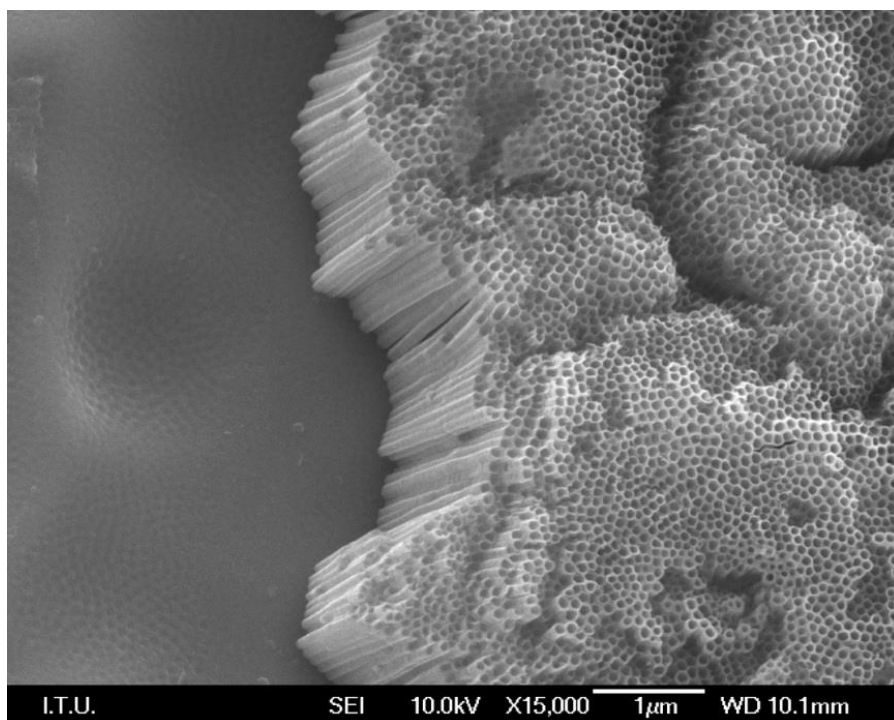


**Figure 4.5 :** The cross sectional SEM image of nanotubular structure formed on TiAl coating after the anodization process conducted at 40 V and 13 °C in ethylene glycol containing 0.61 wt %  $\text{NH}_4\text{F}$ .

The effects of electrolyte concentration on the surface morphology were also investigated. Nanoporous structure was dominant in ethylene glycol electrolytes consisting 0.18 wt %, 0.25 wt %, 0.32 wt %, 0.40 wt %  $\text{NH}_4\text{F}$  and 0.47 wt % whereas the structure was nanotubular in electrolytes consisting 0.54 wt % and 0.61 wt %  $\text{NH}_4\text{F}$ . Among these concentrations, well-aligned nanotubular structure was obtained on the surface of coatings in the electrolyte consisting 0.61 wt %  $\text{NH}_4\text{F}$  at 40 V as seen in Figure 4.6. The tube diameters and wall thickness of these structures were about 70-90nm and 13-15 nm, respectively. However, a porous layer was also formed on top of the grown nanotubes during the anodization of TiAl coating. This porous layer covered the surface of nanotubular structure partially or entirely depending on the parameters used in anodization process. In the beginning of anodization process, the initial anodic oxide forms at the surface of the metallic coating and then the oxide grows at the metal-oxide interface. Therefore, the porous initial oxide layer is the replica of coating surface morphology since the grain structure and grain boundaries of coating were obviously seen on the surface of this porous layer. After the formation of this porous initial layer, nanotubular layer forms underneath this porous layer. EDS analyses in Table 4.1. indicated that this porous layer has higher concentration of fluoride compared to nanotubular layer. This porous

layer formation can be attributed to the formation of  $\text{AlF}_3$  compound during anodization of TiAl coatings and this compound may have a hinderence effect on the progress of anodization process.

In order to remove this porous layer on the surfaces of nanotubes, second anodization was conducted using electrolytes with different HF concentrations and durations. The optimized conditions for second anodization were determined as 15 V in 0.6 v % HF containing electrolyte. By the application of second anodization for 30 sec, the porous layer was etched as in Figure 4.7 and the resulting surface shown in Figure 4.8 was obtained. However, 30 sec was insufficient to etch the porous layer formed on the surface of anodized coatings produced in 0.25 wt %  $\text{NH}_4\text{F}$  consisting electrolyte at 21 °C and also homogeneous nanotube length could not be obtained when the duration was increased.

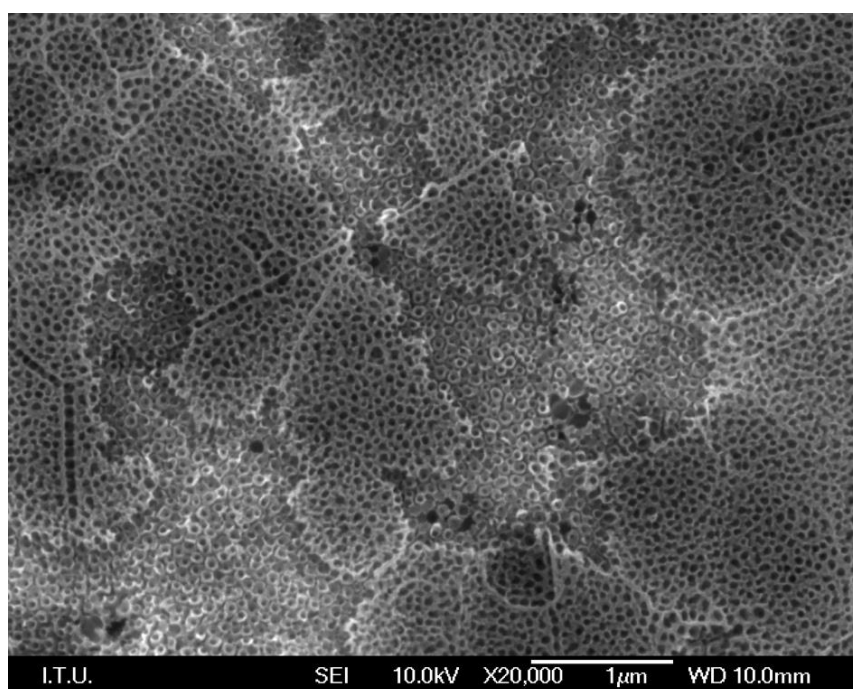


**Figure 4.6 :** The SEM image of nanotubular structure formed on TiAl coating after the first anodization process conducted at 40 V and 13 °C in ethylene glycol containing 0.61 wt %  $\text{NH}_4\text{F}$ .

Consequently, the optimal  $\text{NH}_4\text{F}$  concentration in etylene glycole was determined as 0.61 wt % and 0.25 wt % for well-aligned and high thickness of nanotubes, respectively. Therefore, these electrolyte concentrations were used in the following detailed investigations about anodization of Ti and TiAl thin film coatings.

**Table 4.1 :** EDS analyses of porous and nanotubular layer formed on the surface of TiAl coating after anodization process.

	Porous Layer		Nanotubular Layer	
	Weight %	Atomic %	Weight %	Atomic %
<b>Ti</b>	32	15	43	21
<b>O</b>	38	53	38	56
<b>F</b>	24	28	14	17
<b>Al</b>	4.2	3.5	4.1	3.6

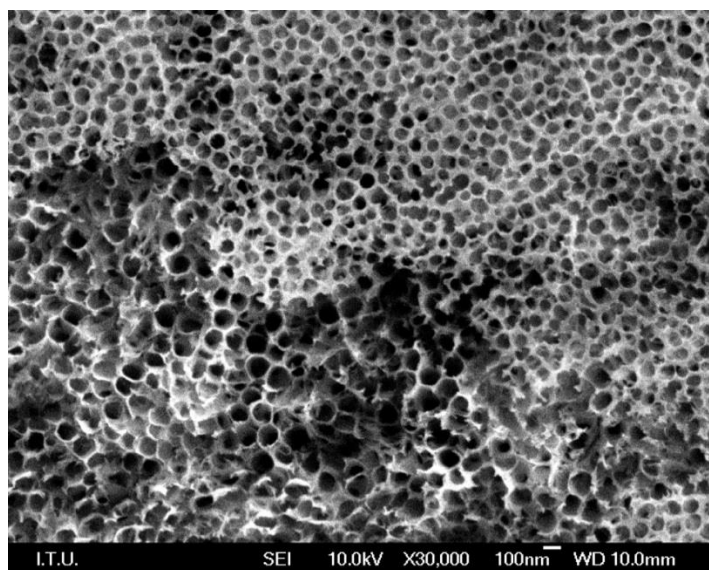


**Figure 4.7 :** The SEM image of etched nanoporous structure using second anodization process conducted at 40 V in 0.6 v % HF containing electrolyte.

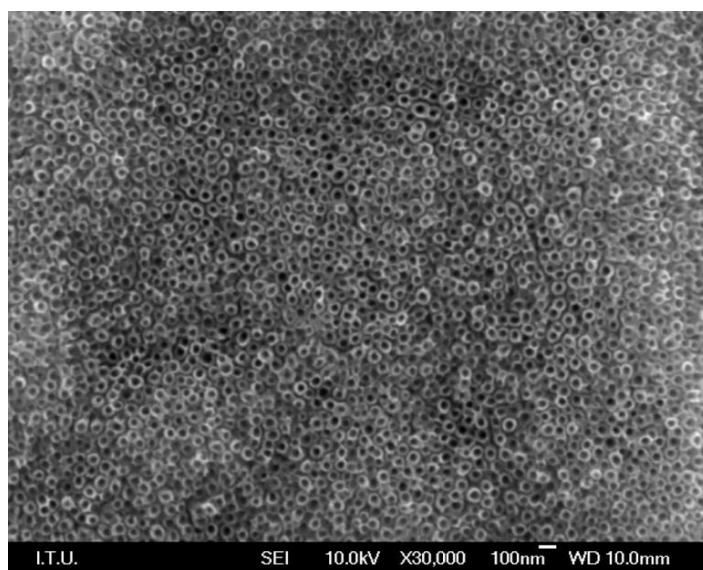


**Figure 4.8 :** The SEM image of resulting nanotubular structure formed on TiAl coating after the second anodization process

#### 4.1.2 The effects of potential in TiAl coating anodization

The applied voltage affects the surface morphology and also dimensions of nanotubes. The effects of anodization potential on nanostructure growth were investigated in 0.25 wt % and 0.61 wt %  $\text{NH}_4\text{F}$  containing electrolytes. The anodization processes were conducted at the voltages of 40, 50, 60, 65, 70 V. In 0.25 wt %  $\text{NH}_4\text{F}$  containing ethylene glycol, nanotubular structure was successfully fabricated in a voltage window from 40 to 70 V. The diameter and the length of the nanotubes increased gradually with increasing anodization voltage until 65 V. Above 65 V, the nanotube length began to decrease slightly and their structures began to deteriorate. At this high voltage, the dissolution rate may increase the growth rate of nanotubes since the  $\text{F}^-$  ions diffusion through the bottoms of nanotubes becomes difficult as the nanotube length increases. In addition as the titanium dissolves in electrolyte, the conductivity of electrolyte also increases and this may lead to an increase in dissolution rate of grown nanotubes. So, the optimal anodization potential was determined as 60 V for growing longer nanotubes and the cross sectional SEM image of nanotubular structure produced at 60 V for 250 min in 0.25 wt %  $\text{NH}_4\text{F}$  ethylene glycol containing was shown in Figure 4.9.

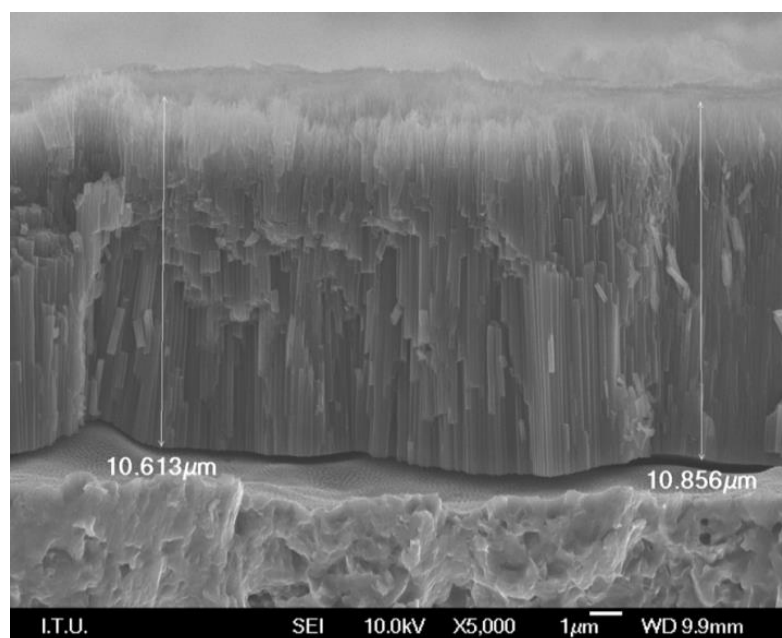


**Figure 4.9 :** The cross sectional SEM image of nanotubular structure formed on TiAl coating after the anodization process conducted at 60V and 13°C for 250 min in 0.25 wt %  $\text{NH}_4\text{F}$  containing electrolyte.

The effect of anodization potential on the structure of nanotubes grown in 0.61 wt %  $\text{NH}_4\text{F}$  consisting electrolyte was also investigated. In the range of anodizing potentials from 40 V to 70 V, well-aligned nanotube arrays were obtained at 40 V in this electrolyte concentration. As the voltage increased from 40 V to 50 V, these arrays became irregular and nanotubular structure was distorted as seen in Figure 4.10. Therefore 40 V was determined as the highest potential for producing well-ordered nanostructures in the electrolyte concentration used.

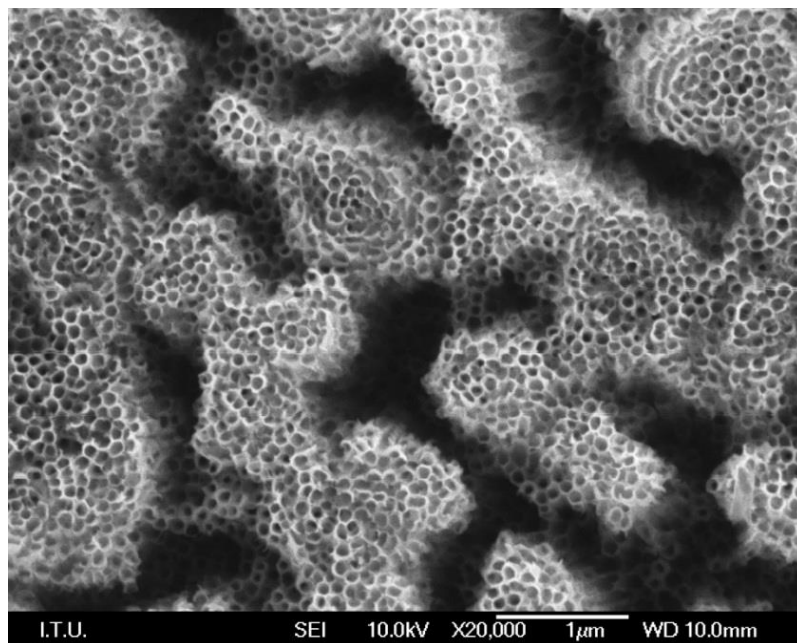


**Figure 4.10 :** The SEM image of nanotubular structure formed on TiAl coating after the anodization process conducted at 50V and 13°C for 120 min in 0.61 wt %  $\text{NH}_4\text{F}$  containing electrolyte.

#### 4.1.3 The effects of temperature in TiAl coating anodization

The optimal anodization voltage and  $\text{NH}_4\text{F}$  concentration for obtaining high thickness of nanotube length were determined as 60 V and 0.25 wt %  $\text{NH}_4\text{F}$ , respectively. The effects of temperature on nanotube length were investigated using these anodization parameters. When the all parameters were constant, the anodization temperature was increased from 13 °C to 21 °C and as a result, the nanotube length rised from 11 micron to 14 microns (seen in Figures 4.11 and 4.12). With further increasing the temperature up to 29°C, the nanotube length was increased to 16 microns as seen in Figure 4.13. Anodization temperature has a significant effect on the morphology of the as-anodized coatings. In the case of anodization process conducted at 21°C, only the porous layer was observed on the

anodized surfaces. However, as the temperature increased, highly disordered nanostructures were obtained on the anodized surfaces. Therefore, the optimal anodization temperature for obtaining highly ordered and as well as longer nanotubes was determined as 21 °C and the subsequent anodization experiments were conducted at this temperature.

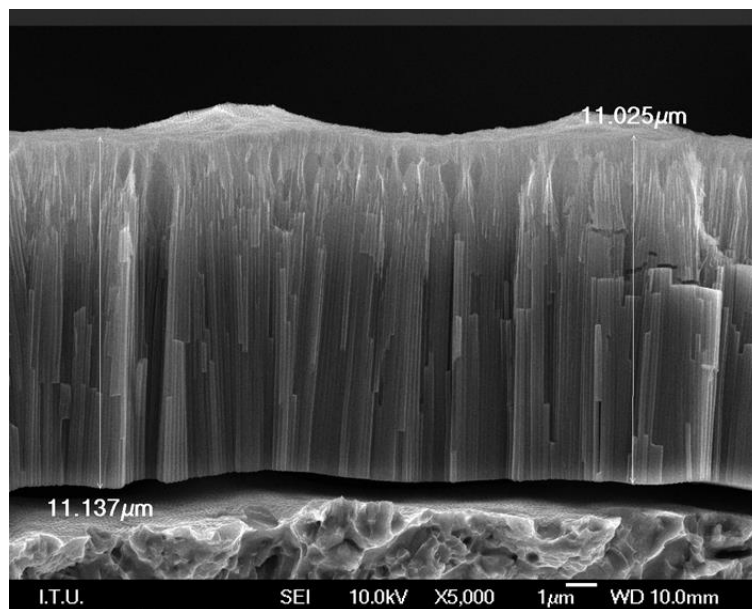


**Figure 4.11 :** The cross sectional SEM image of nanotubular structure formed on TiAl surface after 250 min anodic oxidation at 60 V in 0.25 wt %  $\text{NH}_4\text{F}$  containing electrolyte at 13°C.

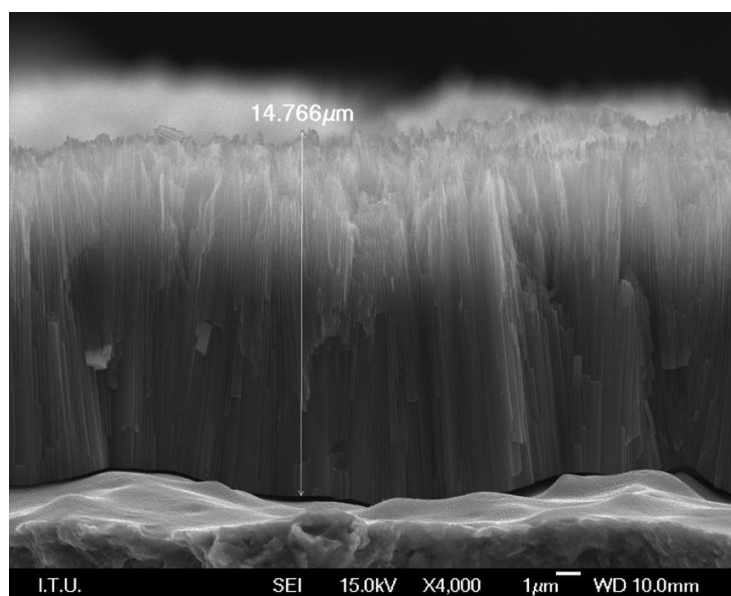


**Figure 4.12 :** The cross sectional SEM image of nanotubular structure formed on TiAl surface after 250 min anodic oxidation at 60 V in 0.25 wt %  $\text{NH}_4\text{F}$  containing electrolyte at 21°C.

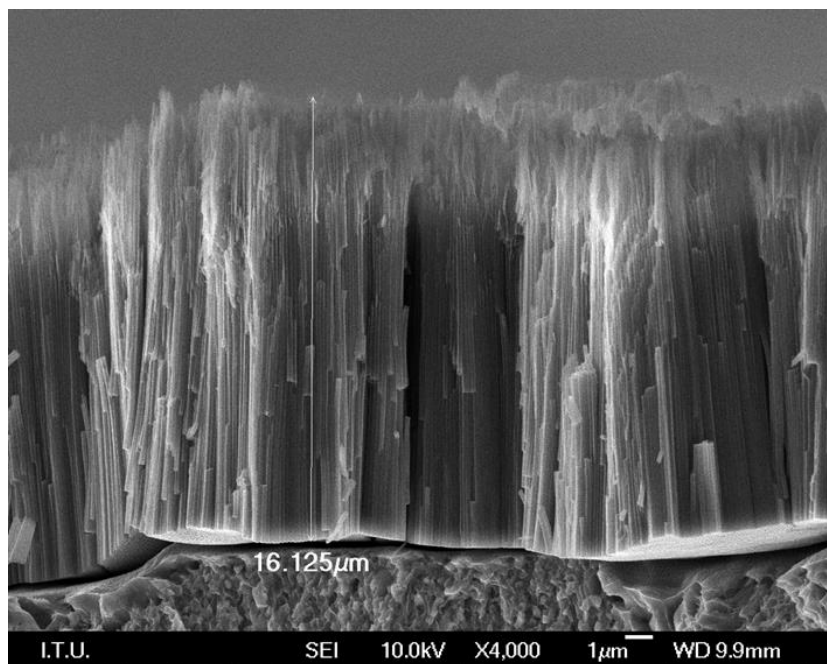


**Figure 4.13 :** The cross section SEM image of nanotubular structure formed on TiAl surface after 250 min anodic oxidation at 60 V in 0.25 wt %  $\text{NH}_4\text{F}$  containing electrolyte at 29°C.

#### 4.1.4 The effects of water content in electrolyte in TiAl coating anodization

A key parameter that influences the growth of nanotubes is water content in the electrolyte. In these experiments 0.25 wt %  $\text{NH}_4\text{F}$  was dissolved in 1 vol % water then mixed with ethylene glycol. When the water volume in electrolyte was increased to 1.6 vol %, it was observed that the nanotube length was increased from 4.8 microns to 5.7 microns for 40 min at 60 V and 21°C.

The surface SEM image of this nanostructure produced at 60 V and 21°C for 40 min in 1.6 vol % water and 0.7g  $\text{NH}_4\text{F}$  containing electrolyte was shown in Figure 4.14. At these conditions, the porous layer covered the entire surface of as-grown nanotubular structure. The measured nanotube diameters from surface and cross sectional images were 60-80nm and 145-155nm, respectively (Figure 4.15). By the increasing of water content, the nanotube diameters were slightly increased. Additionally, water content was increased to 2 vol %, however, a slight decrease was observed in the lengths of nanotubes. Therefore, 1.6 vol % water content was taken to be the highest water content for producing high thickness of nanotubes in the following anodization experiments.



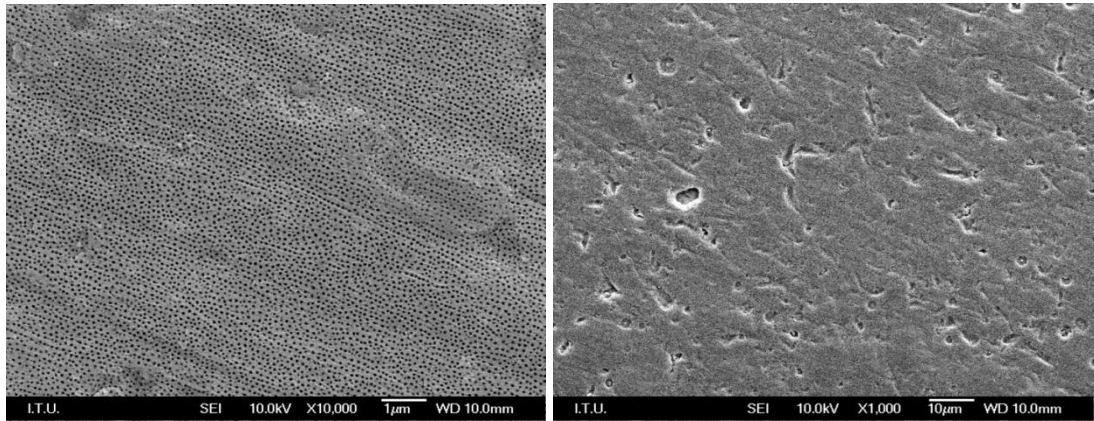


**Figure 4.14 :** The surface SEM image of nanotubular structure formed on TiAl surface after anodic oxidation at 60 V in 1.6 vol % water and 0.25 wt %  $\text{NH}_4\text{F}$  containing electrolyte at 21°C.

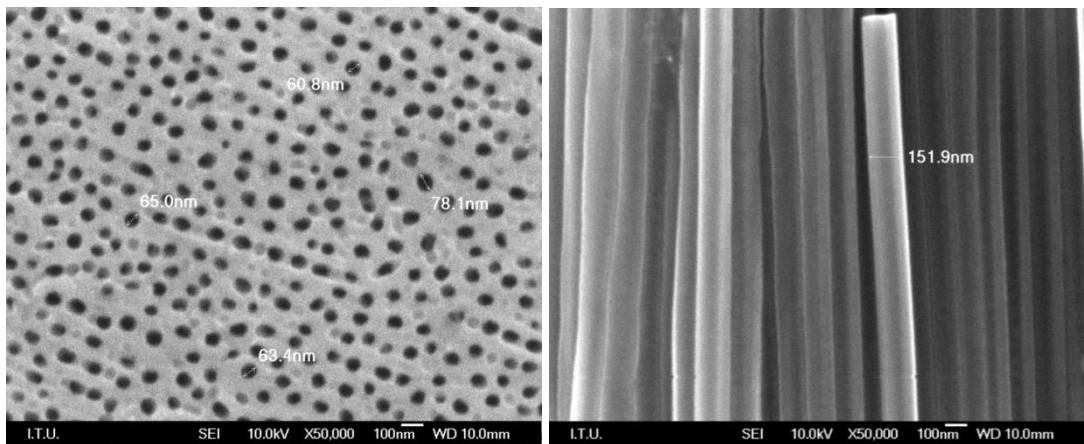


**Figure 4.15 :** The cross sectional SEM image of nanotubular structure formed on TiAl surface after anodic oxidation at 60 V in 1.6 vol % water and 0.25 wt %  $\text{NH}_4\text{F}$  containing electrolyte at 21°C.

#### 4.1.5 The effects of anodization duration in TiAl coating anodization

The influence of different anodization times on the growth rate of nanotubes was investigated in a range from 30 min to 270 min as shown in Fig 4.16. For these experiments, TiAl coatings were anodically oxidized at 60 V in 1.6 vol % water and 0.25 wt %  $\text{NH}_4\text{F}$  containing electrolyte at 21°C. In the earlier stages of anodization, nanotubes grow on TiAl surface more rapidly and then the growth rate slows down. While the length of nanotubes was 3.9 micron after 30 min anodic oxidation, their length was reached to 18.5 microns after 270 min as seen in Figure 4.16.a. and Figure 4.16.f, respectively. The relation established between anodization time and nanotube growth length was depicted in Figure 4.17. Additionally, the metallic film above alumina can be anodized totally using these conditions. These produced nanotubes with high thickness are thought to be appropriate for using as a sensor

material since there is a possibility to occur a short circuit between Pt circuits and the conductive layer underneath the nanotubes.

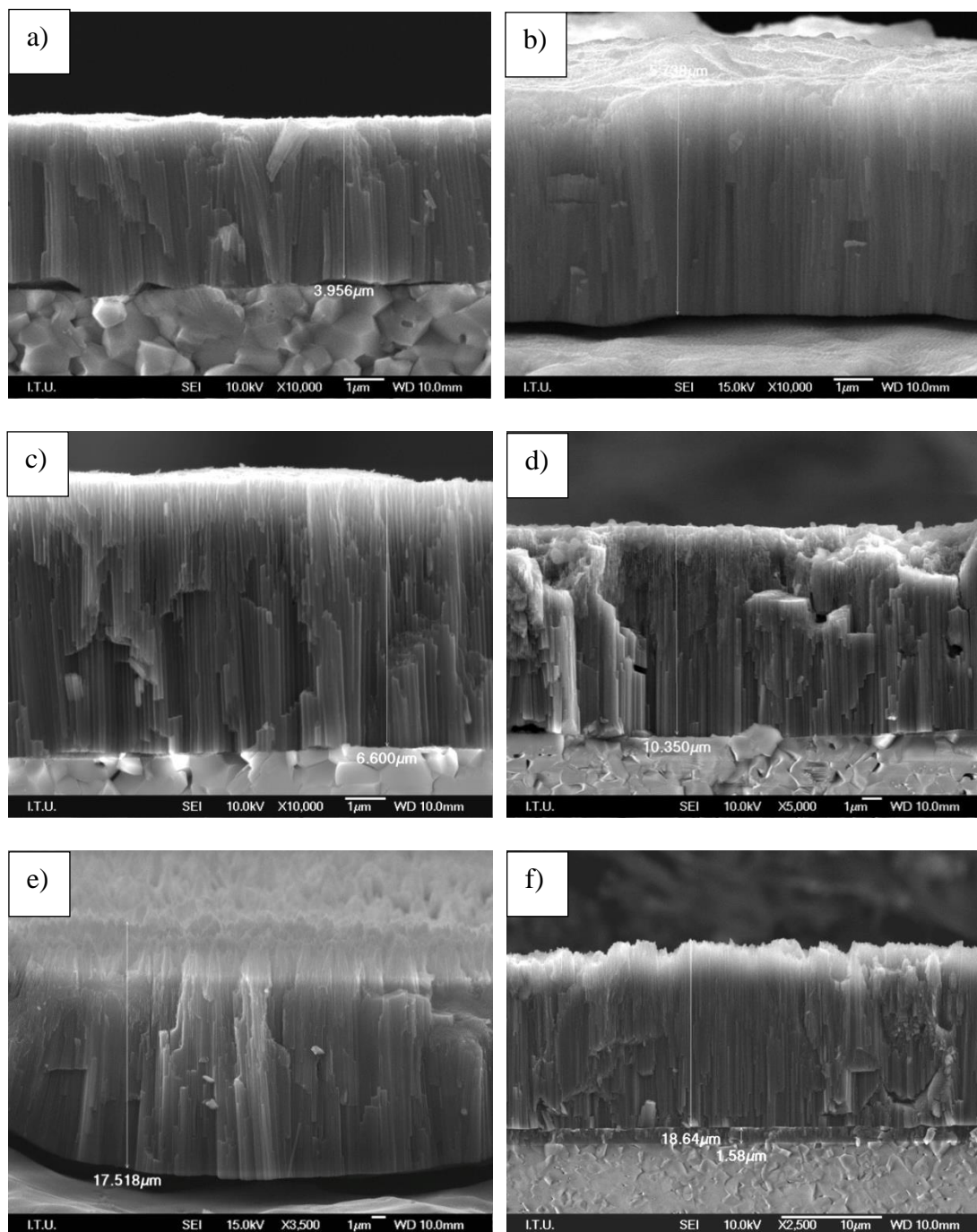


**Figure 4.16 :** The cross sectional images of nanotubular structures with different lengths formed on TiAl coating in 1.6 vol % water and 0.25 wt %  $\text{NH}_4\text{F}$  containing electrolyte at 60 V for a) 30 min b) 40 min c) 60 min d) 100 min e) 250 min f) 270 min

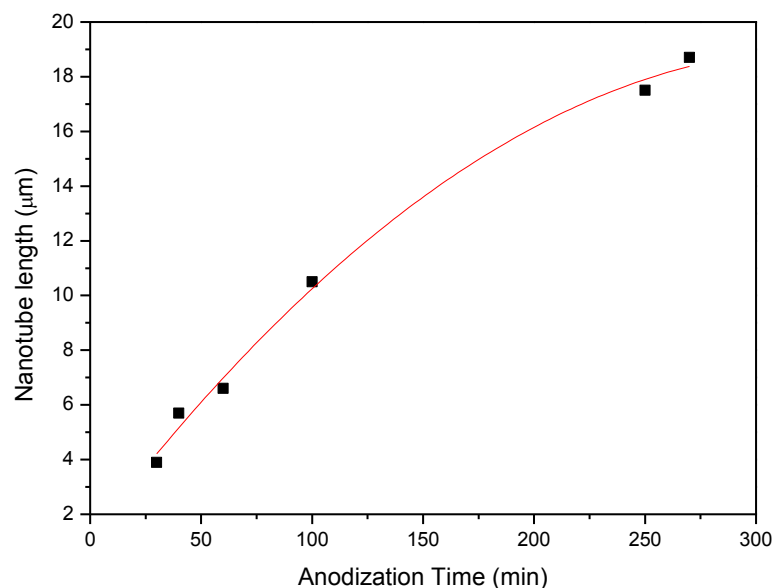


**Figure 4.17 :** The relationship between anodization time and nanotube length grown in 1.6 vol % water and 0.25 wt %  $\text{NH}_4\text{F}$  containing electrolyte at 60 V and 21°C.

#### 4.1.6 The effects of agitation in TiAl coating anodization

In optimization experiments, anodization processes were conducted at 60 V in 0.25 wt %  $\text{NH}_4\text{F}$  consisting electrolyte for different types of agitation. It was realized that there is no difference between the surface SEM images of nanotubes grown in magnetically and ultrasonically stirred electrolytes as seen in Figure 4.18.a and 4.18.b, respectively. Also, it was examined that the type of agitation has no considerable effect on nanotube length under the same conditions.

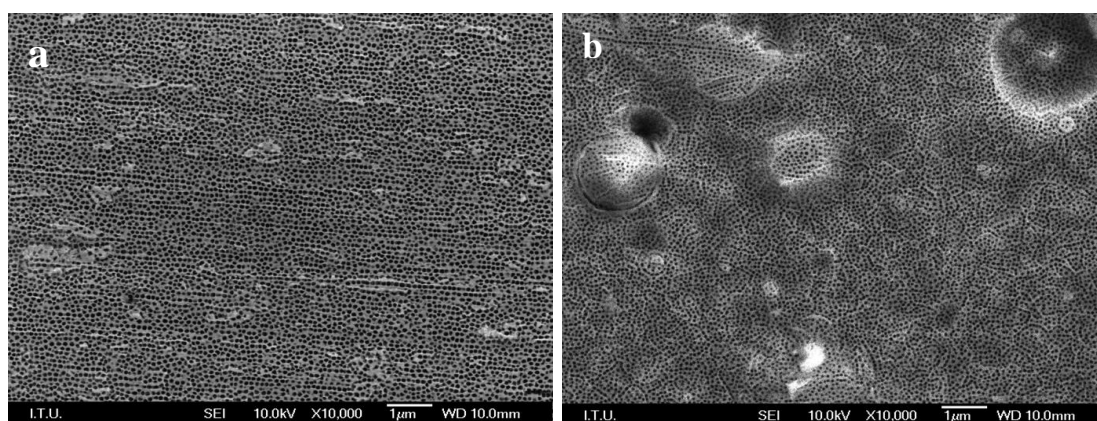


**Figure 4.18 :** The surface SEM images of TiAl nanotubular structure formed on TiAl coated substrate after anodic oxidation at 60 V for 250 min in 0.7g  $\text{NH}_4\text{F}$  containing electrolyte using Figure 4.18. The SEM images of nanotubular structures formed on TiAl coating in 1.6 vol % water and 0.25 wt %  $\text{NH}_4\text{F}$  containing electrolyte at 60 V for and 21°C using a) magnetron stirring b) ultrasonic stirring.



## 4.2 Optimization of Process Parameters for the Anodization of Ti Coatings

The optimal anodization parameters for producing nanotubes with high thickness and well-aligned nanotubes on TiAl coatings were used in anodization of Ti coatings. The metallic Ti coating on alumina was anodized at 40 V in 0.61 wt %  $\text{NH}_4\text{F}$  consisting ethylene glycol electrolyte for 40 min at 13°C. The sample was cleaned in acetone ultrasonically to remove the residues (dissolved nanotube walls) on the nanotubular structure that were formed during anodization. The surface SEM image of Ti nanotubular structure on alumina substrate was shown in Figure 4.19. Using the anodization conditions mentioned above, highly ordered nanotube arrays were created on the surface of Ti coating.

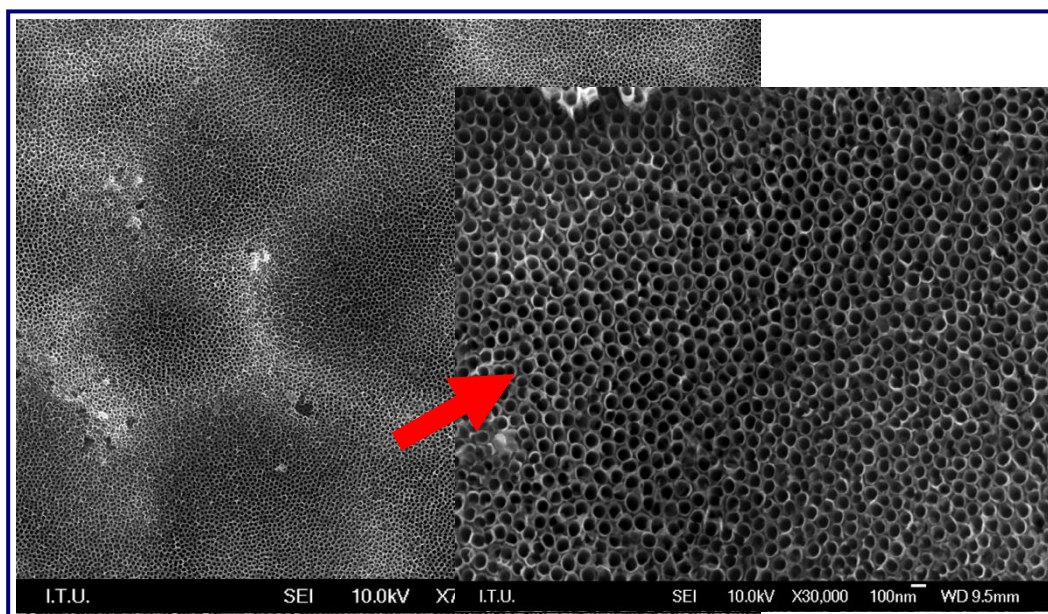


**Figure 4.19 :** The nanotubular structure which was formed on Ti coated alumina substrate after anodization process that conducted at 40 V and 13 °C in 0.61 wt %  $\text{NH}_4\text{F}$  consisting ethylene glycol for 40 min

Anodization process conducted using different conditions in order to examine the effects of anodization potential and electrolyte concentration on nanotubular Ti anodic oxides. For this purpose, Ti coatings were anodized at 40 V, 50 V, 60 V in 0.61 wt %  $\text{NH}_4\text{F}$  consisting ethylene glycol at a temperature of 13 °C. The resulting nanotube diameters were, respectively, 85-100 nm, 100-120nm, 140-160 nm for 40, 50, 60 anodization voltages. It was also determined that the amount of  $\text{NH}_4\text{F}$  in anodization electrolyte influenced the diameters of nanotubes and as well as their lengths. The nanotubular structure seen in Figure 4.20 was formed on Ti coating after the anodization process conducted at 60 V in 0.25 wt %  $\text{NH}_4\text{F}$  containing ethylene

glycol electrolyte during 250 min. The surface and cross sectional SEM images of these nanostructures at different magnifications were given in Figures 4.20 and 4.21, respectively. Increasing anodization potential from 40 V to 60 V, reducing the amount of  $\text{NH}_4\text{F}$  in electrolyte and increasing anodization duration led to formation of 9-10 microns nanotubes in length.

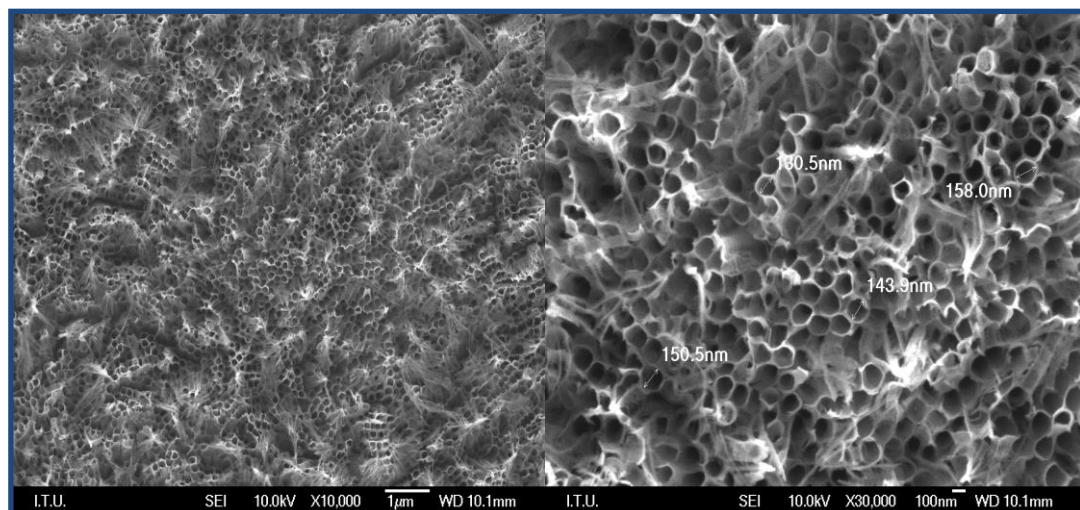


**Figure 4.20 :** The surface SEM image of nanotubular structure formed on Ti coating after the anodization process done at 60 V and 13 °C in 0.25 wt %  $\text{NH}_4\text{F}$  containing electrolyte for 250 min.

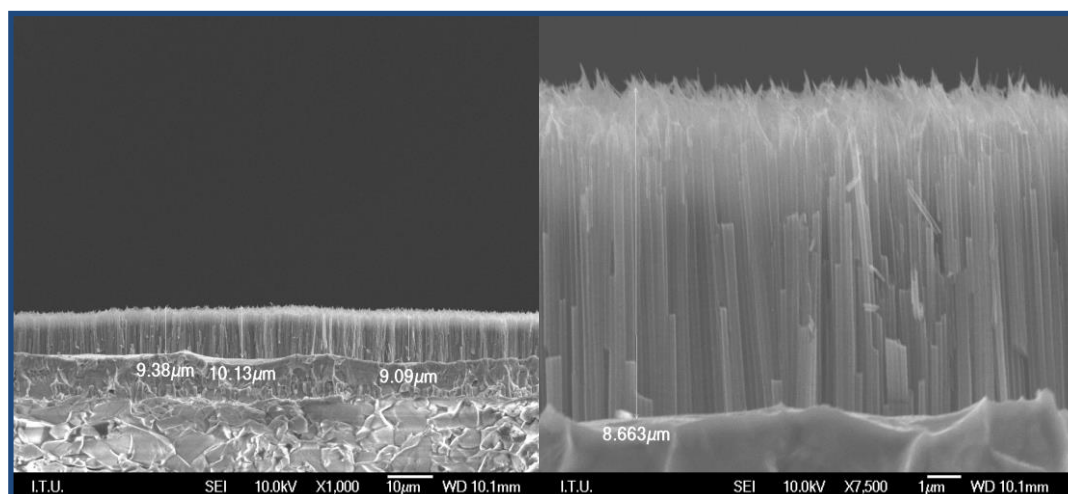


**Figure 4.21 :** The cross sectional SEM image of nanotubular structure formed on Ti coating after it was anodized at 60 V and 13°C in 0.25 wt %  $\text{NH}_4\text{F}$  containing electrolyte for 250 min.

The significant effects of temperature and water content on the anodized surface were also investigated. By increasing the temperature from 13°C to 21°C in 1.6 v % water and 0.25 wt %  $\text{NH}_4\text{F}$  containing electrolyte, it is possible to grow nanostructures with a thickness of 11-12 micron for 120 min (Figure 4.23). However, nanoporous

structure was obtained instead of nanotubular structure in these conditions as seen in Figure 4.22.

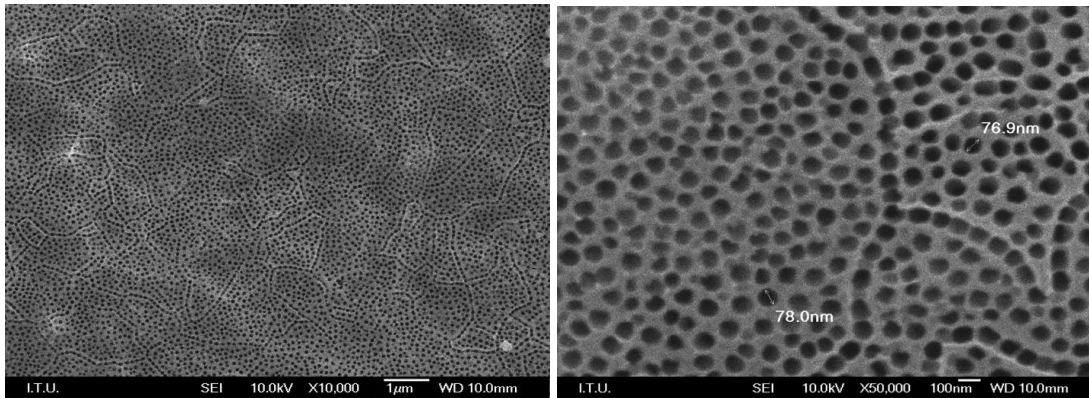


**Figure 4.22 :** The SEM image of nanotubular structure formed on Ti coating after it was anodized at 60 V and 21°C in 0.25 wt %  $\text{NH}_4\text{F}$  and 1.6 v % water containing electrolyte for 120 min.

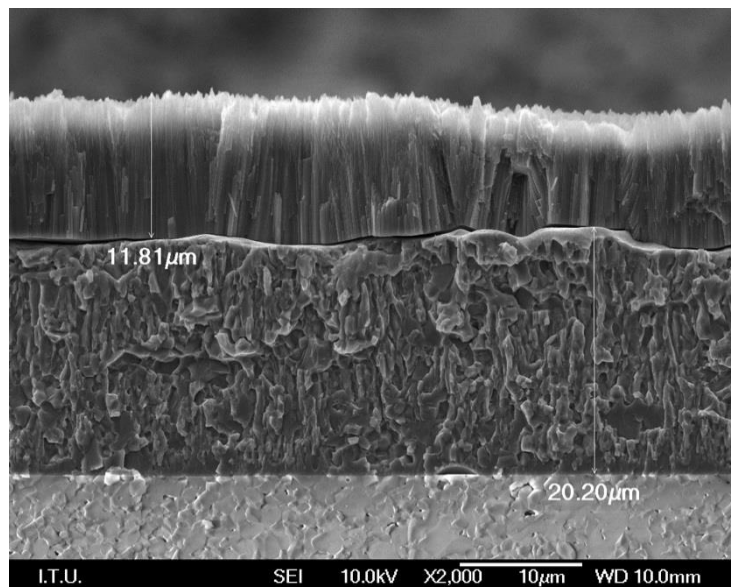


**Figure 4.23 :** The cross sectional SEM image of nanotubular structure formed on Ti coating after it was anodized at 60 V and 21°C in 0.25 wt %  $\text{NH}_4\text{F}$  and 1.6 v % water containing electrolyte for 120 min

### 4.3 The Influence of Different Coating Structures on Anodization Process

Two types of Ti-Al coatings were used in the optimization of anodization studies. These are the coatings produced at -100V bias with and without post treatment. The possible effects of post treatment on as grown nanoporous structure were investigated. Both these two different coating structures promoted the formation of highly ordered nanoporous-nanotubular structures on their surfaces. However, crack formation was observed on the surface of the post treated coatings after anodization

process as shown in Figure 4.24. This may arise from the internal stress induced by high bias voltage application or the volume expansion that may occur during the anodization process. Therefore, the coatings produced without post treatment was selected as the most appropriate coating structures for anodization process.

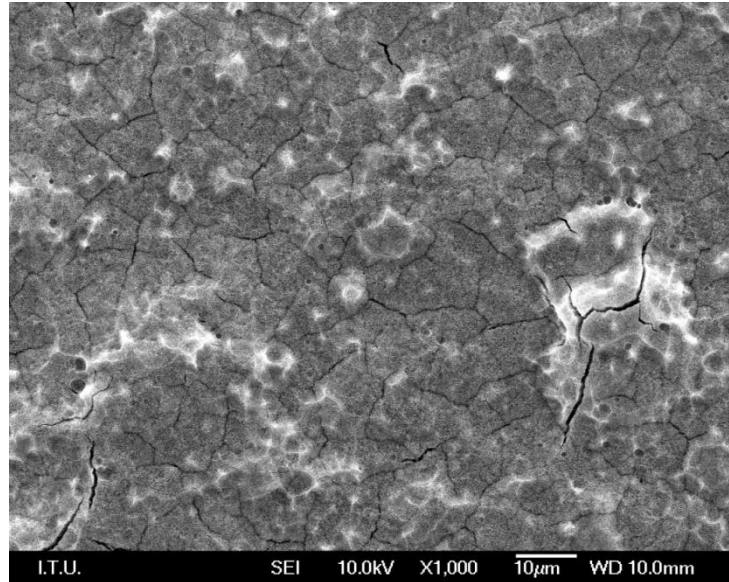


**Figure 4.24 :** The surface SEM image of anodically oxidized TiAl coating deposited at -100 V bias and then subjected to high bias voltage post treatment.





## **5. INVESTIGATION OF AMORPHOUS TO ANATASE AND ANATASE TO RUTILE PHASE TRANSFORMATIONS IN NANOSTRUCTURED Ti AND TiAl ANODIC OXIDES**

### **5.1 The Crystallization Behavior of Nanostructured Ti and TiAl Anodic Oxides**

In chemiresistive type of hydrogen sensors, surface reactions govern the gas detection and therefore the physical and chemical properties of sensor surface play a distinctive role in detection of analyte gas.  $\text{TiO}_2$  sensor material used in this study has mainly 3 different polymorphic phases (anatase, rutile, brookite) and  $\text{TiO}_2$  surface has to be in the most appropriate phase to detect hydrogen gas.

The meta-stable anatase phase of titania is more preferable for hydrogen gas sensor owing to its high sensitivity to hydrogen gas [35, 36] and high performance during the surface reactions [27]. In addition, anatase  $\text{TiO}_2$  phase has approximately 10 times larger electron mobility compared to rutile  $\text{TiO}_2$  and therefore anatase phase has a great importance in gas sensor applications [38, 93].

Since gas sensors are expected to work at high temperatures, shifting of the anatase-rutile transformation to higher temperatures is advantageous. By this way, anatase may remain stable at higher temperatures and thus the operating temperature range of sensor is extended. The anatase-rutile transformation takes place in the temperature range 600-700°C; however, the reported temperatures for the transformation can vary from 400°C to 1200°C. This wide range can arise from -the type and amount of additives, - impurities, - processing methods and conditions used in sample preparation, -the thermal treatment atmosphere and conditions, -the sample geometry (bulk, film, etc.) and use of different methods of determining the transition temperatures [16,37,40-44]. These parameters significantly affect and alter the transformation rate and activation energy. Therefore, anatase-rutile transformation occurs at a transition temperature either higher or lower than that of pure titania depending on the above mentioned parameters [43].

There are some studies in the literature [35,37,51] concerning the effects of Al doping on the phase transformation of bulk titania. However, there are no studies in the literature conducted on the phase transformation of nanoporous TiAl-oxide produced with anodization. In the present study, the effects of Al doping in TiO<sub>2</sub> lattice were investigated by the phase analyses of the undoped TiO<sub>2</sub> and Al-doped TiO<sub>2</sub> nanostructures after they were subjected to heat treatment processes. The crystallization behaviors of nanostructured Ti and TiAl anodic oxides were investigated after heat treatments conducted at different temperatures. For these experiments, Ti and TiAl (9-10 wt % Al content) coatings were deposited on alumina substrates at 100 V bias voltage for 30 min. All thin film coatings were produced using a cathode current of 60 A and 20 sccm argon gas flow rate. Then these thin film coatings were anodized at 60 V and 21°C for 60 min in ethylene glycol electrolyte consisting 0.25 wt % NH<sub>4</sub>F and 1.6 vol % H<sub>2</sub>O.

After anodization process, amorphous nanotubular structures were obtained on the surfaces of coatings (see section 4). Then the samples were subjected to heat treatments at 280°C, 350°C, 420°C, 485°C, 550°C, 600°C, 650°C and 720°C in air atmosphere for 1 hour and a separate sample was used for each heat treatment. Even after the heat treatment at 720 °C, the nanotube architecture remained on the surface of Ti and TiAl coatings without deteriorating or collapsing.

The phase detection and analyses of these anodic oxides were accomplished by XRD and micro-Raman measurements. The XRD analyses performed in glancing angle X-ray diffraction (GAXRD) and theta-2theta (powder) X-ray diffraction (PXRD) geometries. A glancing angle of 2° was used for all GAXRD measurements. The crystallite size was calculated using the Scherrer method by taking the full width half-maximum of some selected intense peaks.

According to heat treatment results, the crystallization had not yet started at 280 °C and completely amorphous structures were observed in both anodic oxides as seen in Figure 5.1.

After heat treatment at 350 °C, the amorph undoped TiO<sub>2</sub> structure was crystallized into the anatase and sharp anatase peaks appeared. However, anatase crystallization in Al-doped TiO<sub>2</sub> was retarded and amorphous structure was maintained as seen in Figure 5.2.

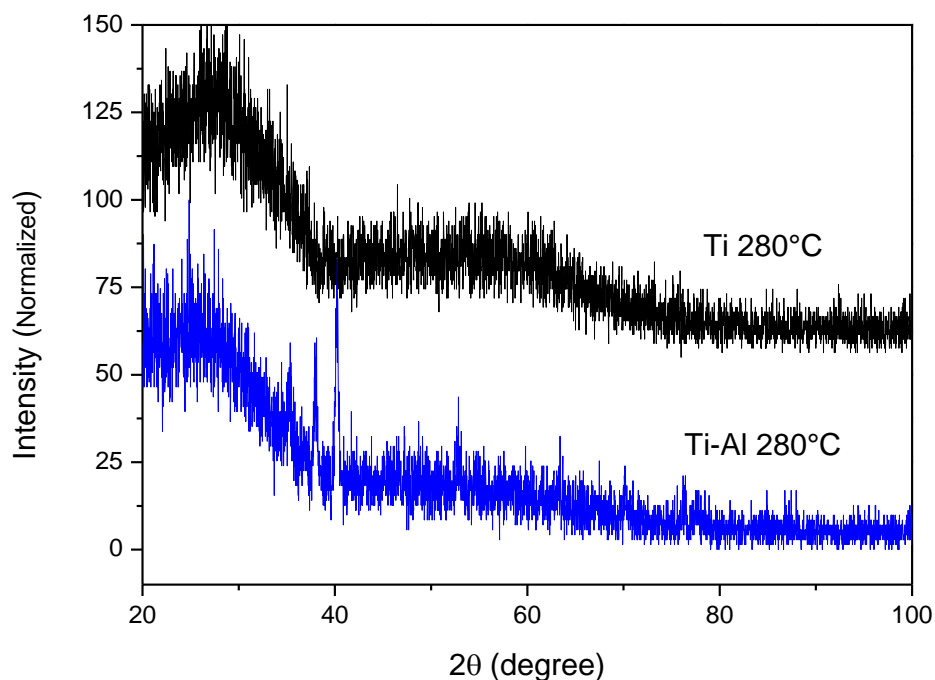


**Figure 5.1 :** The GAXRD patterns of Ti and TiAl anodic oxides after the heat treatment at 280 °C.

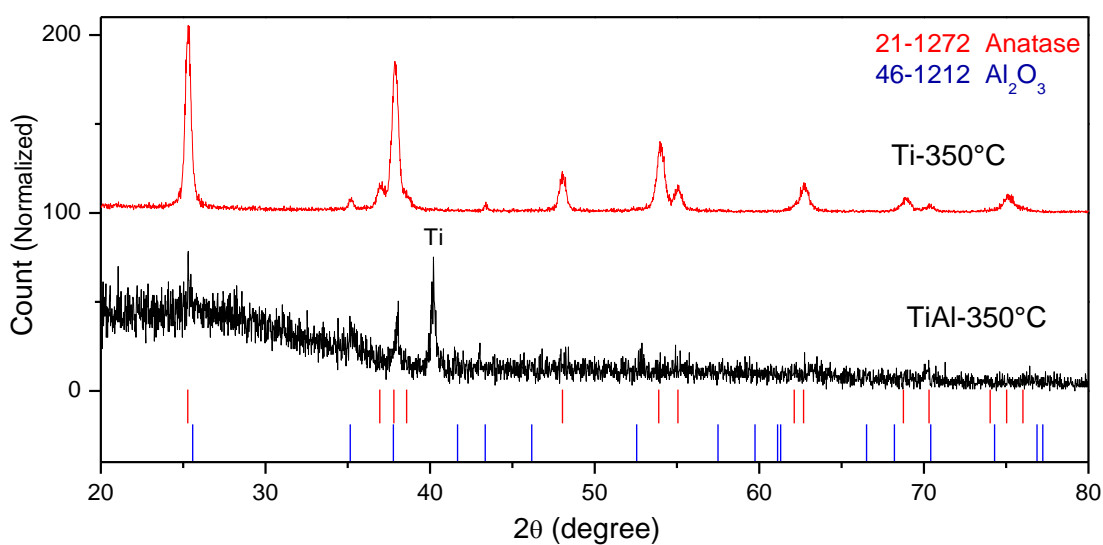


**Figure 5.2 :** The GAXRD patterns of Ti and TiAl anodic oxides after heat treatment at 350 °C.

The amorph-anatase phase transformation began to take place in Al-doped  $\text{TiO}_2$  near 420 °C as seen in Figure 5.3. (the reflection at 41 degree arises from metallic Ti that was underneath the nanotubes) According to the results of heat treatments conducted at 350°C and 420°C, Al doping has a retarding effect on crystallization of  $\text{TiO}_2$  structure that is measured in GAXRD mode. In Ti anodic oxide, the intensities of anatase peaks were higher at 420 °C compared to 350 °C. When the x-ray diffraction patterns of two anodic oxides are compared, it is obviously seen that the anatase  $\text{TiO}_2$

peaks are sharper and their intensities are higher than the peak intensities in Al-doped  $\text{TiO}_2$ . This result indicates that the crystallization in  $\text{TiO}_2$  is kinetically more favored than Al-doped  $\text{TiO}_2$ . Literature emphasized that the type of dopant is very effective on anatase-rutile transformation and it has no apparent effect on the crystallization of anatase [40]. The opposite tendency was observed in this study and this might have aroused from different methods used in sample preparation or the amount of Al ions doped to  $\text{TiO}_2$  lattice and duration of heat treatment. This effect can also be explained by the grain refinement effects of Al doping which kinetically hinders the transformation.

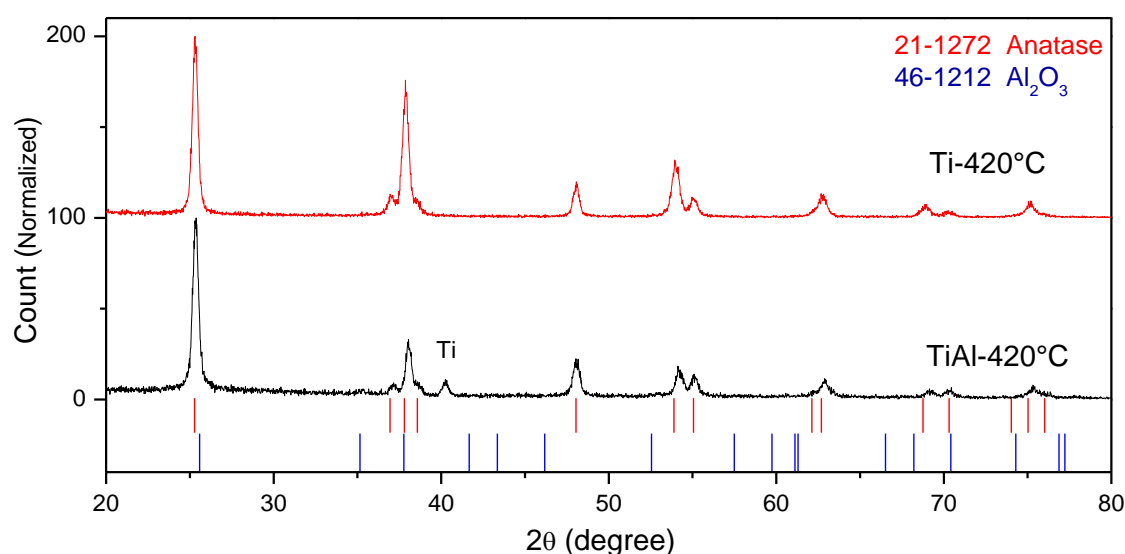


**Figure 5.3 :** The comparison of the GAXRD patterns of Ti and TiAl anodic oxides after heat treatment at 420 °C.

Then Ti and TiAl anodic oxides were subjected to heat treatments at 420 °C, 485 °C, 550 °C, 600 °C and 650 °C for 1 hour. The GAXRD patterns of Ti anodic oxide obtained after the heat treatments at different temperatures were represented in Figure 5.4. The anatase peak intensities of Ti anodic oxide were higher after the heat treatment at 485°C compared to 420°C and therefore the crystallization was further improved after heat treating at 485°C. Similar behavior was also seen in the Raman spectra given Figure 5.5. As a result of heat treatments conducted at 485°C, 550°C, 600°C and 650°C, in all cases increase in the intensities of the Raman peaks were observed. After the heat treatment processes conducted up to 650 °C, transformation to the rutile phase was not detected for both types of samples. For further checking, XRD patterns with theta-2 theta ( $\theta$ -2 $\theta$ ) configuration were also taken. In this mode

X-ray penetrate deeper into the structure. There is also no indication of rutile formation in Ti anodic oxides as seen in these XRD patterns (Figure 5.6)

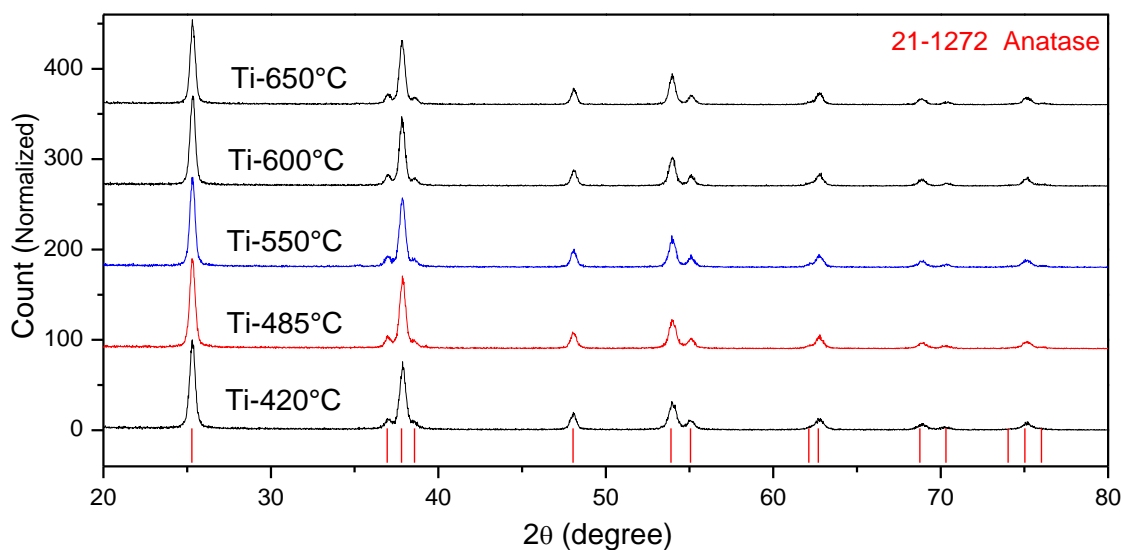


**Figure 5.4 :** The GAXRD patterns of Ti anodic oxide obtained after the heat treatments conducted at 420°C, 485°C, 550°C, 600°C and 650°C.

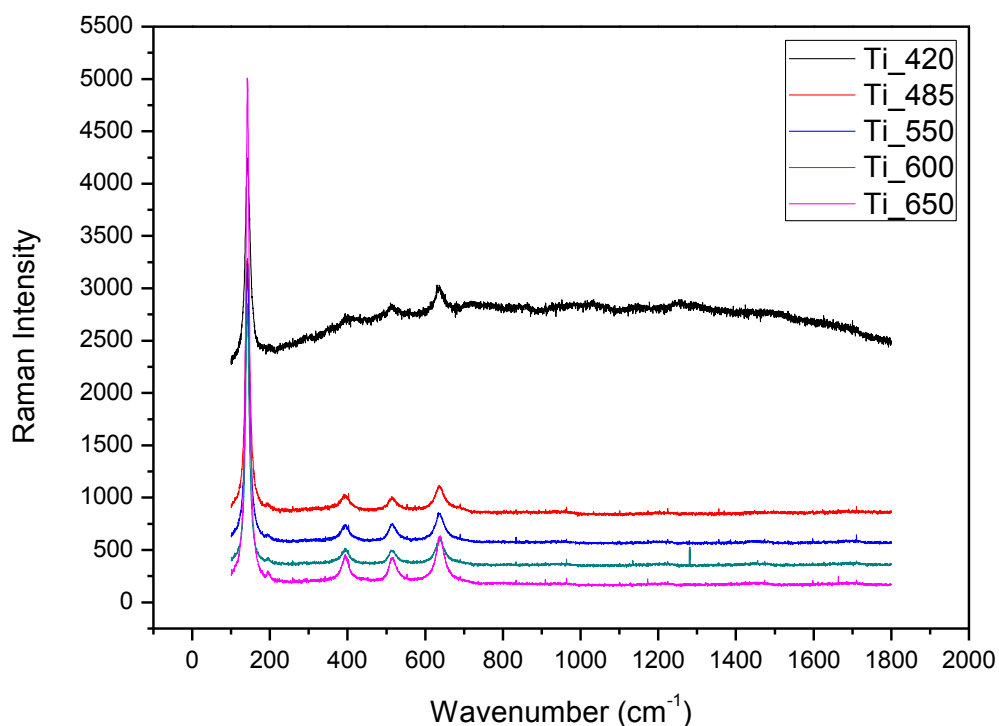


**Figure 5.5 :** The Raman spectra of Ti anodic oxide obtained after the heat treatments conducted at 420°C, 485°C, 550°C, 600°C and 650°C.

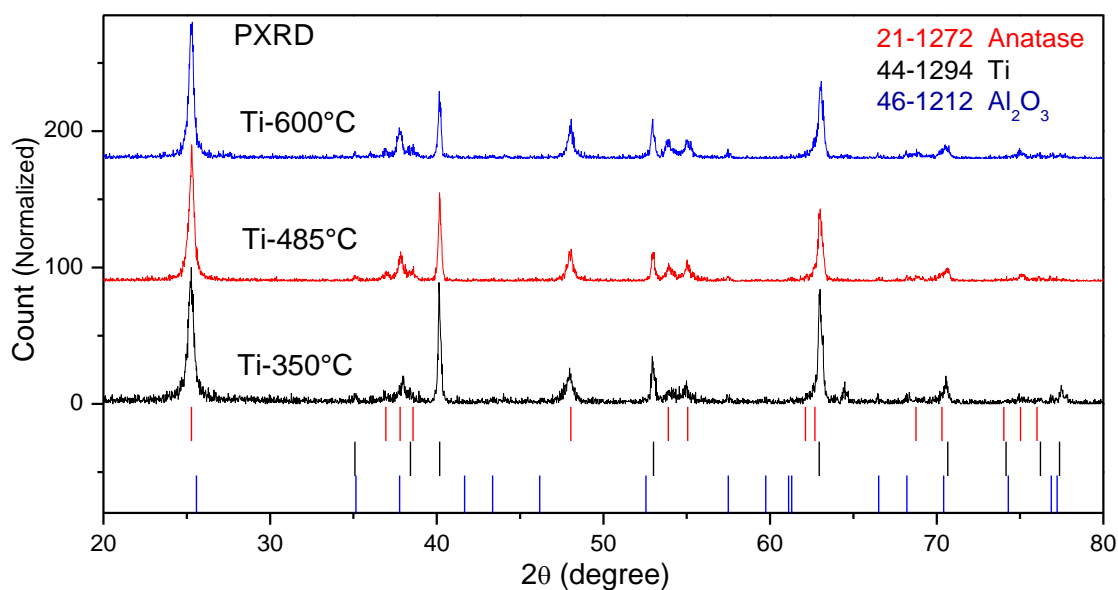


**Figure 5.6 :** The PXRD patterns of Ti anodic oxide obtained after the heat treatments conducted at 350°C, 485°C and 600°C.

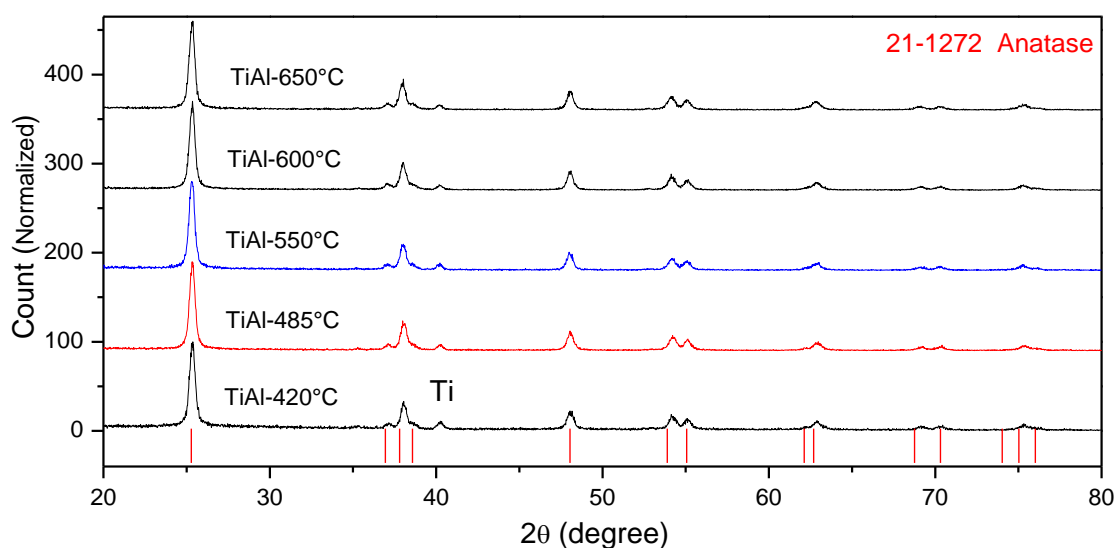


**Figure 5.7 :** The GAXRD patterns of TiAl anodic oxide obtained after the heat treatments conducted at 420°C, 485°C, 550°C, 600°C and 650°C.

TiAl anodic oxide was also heat treated at 420°C, 485°C, 550°C, 600°C and 650°C and GAXRD and Raman results were given in Figure 5.7 and 5.8, respectively. When the heat treatment temperature was raised to 485°C, crystallization was significantly increased and the structure was completely transformed into anatase phase. After the heat treatment at 485°C, 550°C, 600°C and 650°C, very small increases were observed in anatase peak intensities as the temperature increases. This result indicates the improvement in crystallization with increasing heat treatment

temperature. During these heat treatments rutile phase was not detected in neither GAXRD nor PXRD patterns as seen in Figure 5.7 and 5.9, respectively. When the heat treatment results of TiAl and Ti anodic oxides are compared, it can be concluded that slightly smaller peak intensities were observed in TiAl anodic oxide owing to the retarding effect of Al on  $\text{TiO}_2$  crystallization. In addition, slightly smaller peak intensity in TiAl anodic oxide may suggest that Al dopant in  $\text{TiO}_2$  has an inhibiting effect on grain growth.

In order to determine the temperature of anatase-rutile crystallization, Ti and TiAl anodic oxides were subjected to heat treatment at  $720^\circ\text{C}$ . Successively, PXRD and GAXRD analyses were performed for nanotubular Ti and TiAl anodic oxides. These anodic oxides exhibited different behaviors in the presence and absence of metallic film underneath the nanotube layer as summarized below.

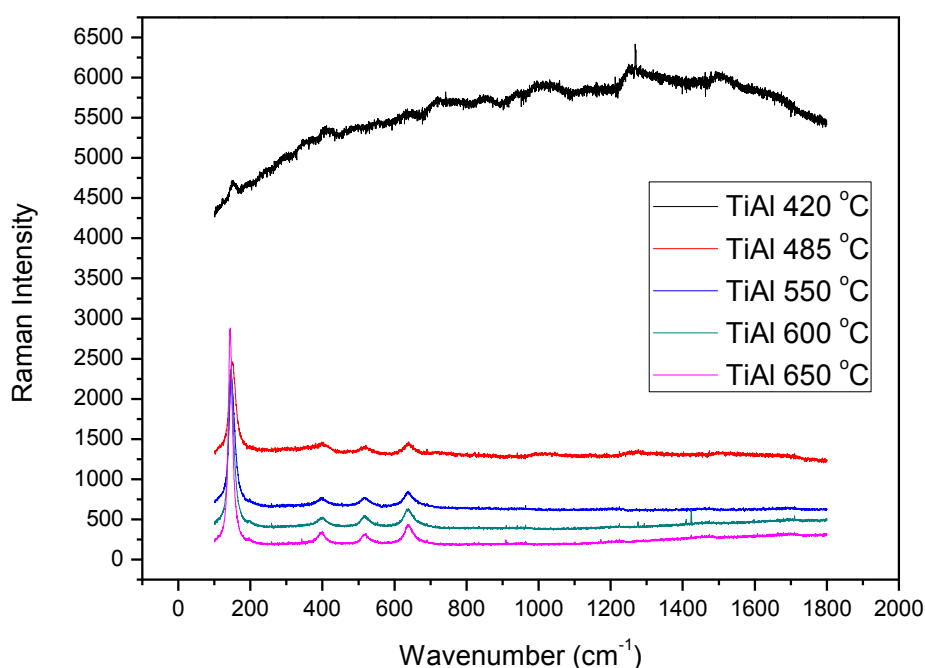


**Figure 5.8 :** The Raman spectra of TiAl anodic oxide obtained after the heat treatments conducted at  $420^\circ\text{C}$ ,  $485^\circ\text{C}$ ,  $550^\circ\text{C}$ ,  $600^\circ\text{C}$  and  $650^\circ\text{C}$ .

**Phase transformation in the presence of metallic film underneath the nanotubes;** This sample consisted of alumina substrate, metallic film and nanotubular layer (seen in Figure 4.2). The  $\theta$ - $2\theta$  X-ray diffraction patterns of Ti and TiAl anodic oxides that were heat treated at  $720^\circ\text{C}$  were given and compared in Figure 5.10. These patterns indicate that anatase and rutile phase co-exist in both Ti and TiAl anodic oxides at  $720^\circ\text{C}$ . It was also noticeable that (110) rutile peak in Ti

anodic has relatively higher intensity compared to TiAl anodic oxide. On the other hand, this result is in contrast with those obtained from GAXRD patterns of these two anodic oxides. In these GAXRD patterns given in Figure 5.11, while anatase to rutile transformation was obviously seen in Ti anodic oxides, TiAl anodic oxide remained anatase even after heat treatment at 720 °C. The results of Raman analyses given in Figure 5.12 were also compatible with these GAXRD results. When the conversion from anatase to rutile began to take place around 720 °C, the rutile bands at 446  $\text{cm}^{-1}$  and 609  $\text{cm}^{-1}$  appeared in Raman spectra of Ti anodic oxide which are the strongest bands indicating the existence of rutile nucleation [56,94-96]. However, in TiAl anodic oxide, the addition of Al ions into  $\text{TiO}_2$  structure cause a retardation in the temperature of anatase-rutile phase transformation and there is no indication of rutile nucleation in both GAXRD and Raman results at a temperature of 720 °C.

These results of XRD measurements in both geometries clearly indicated that during the heat treatment at 720 °C anodic oxide structure on titanium is converted to rutile in appreciable amounts since its presence is observed both in PXRD and GAXRD geometries. On the other hand for TiAl oxides, the presence of rutile phase was only observed in  $\theta$ -2 $\theta$  geometry indicating both the retarding role of Al on this transformation and also where the transformation is initiated. This result indicated that the anatase to rutile transformation is highly probably initiated at the metal – oxide interface as proposed in other studies [97,98].

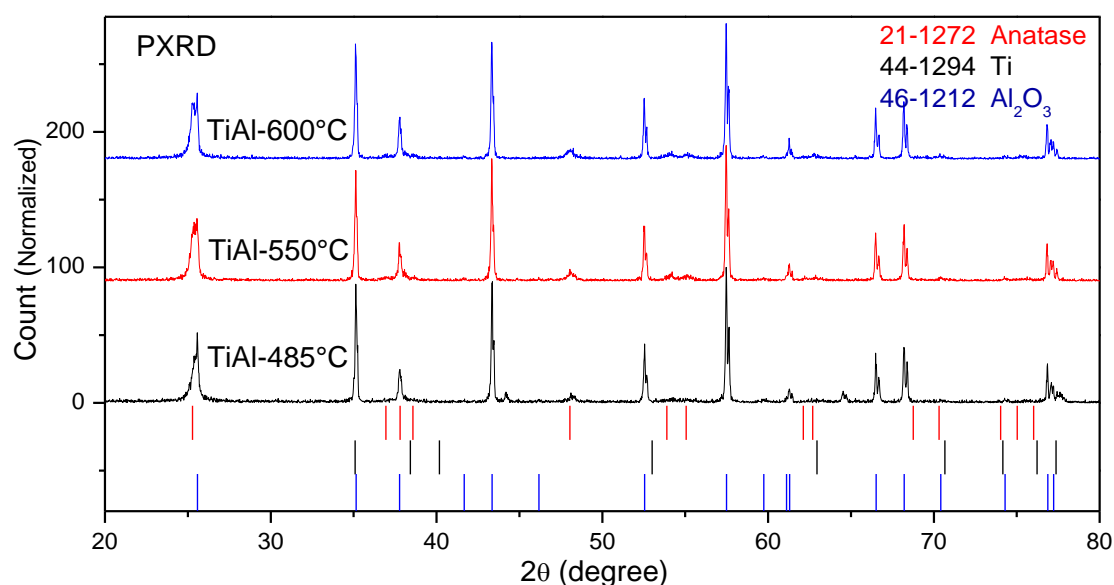


**Figure 5.9 :** The PXRD patterns of TiAl anodic oxide obtained after the heat treatments conducted at 485°C, 550°C and 600°C.



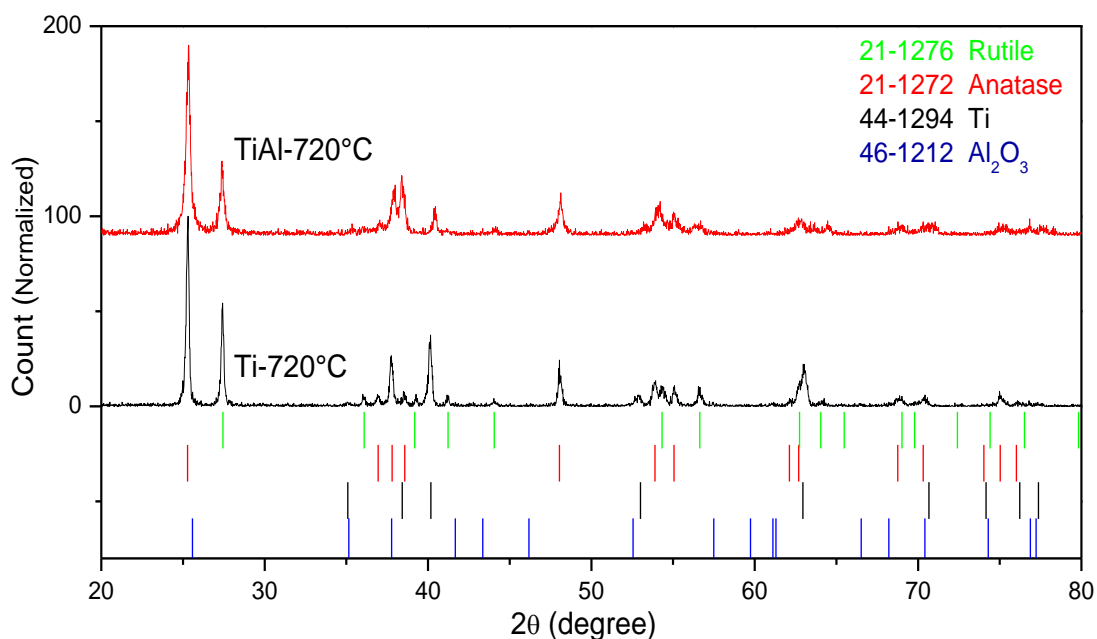


**Figure 5.10 :** The comparison of PXRD patterns of Ti and TiAl anodic oxides in the presence of metallic film underneath the nanotube layer which were obtained after the heat treatment at  $720^\circ\text{C}$ .

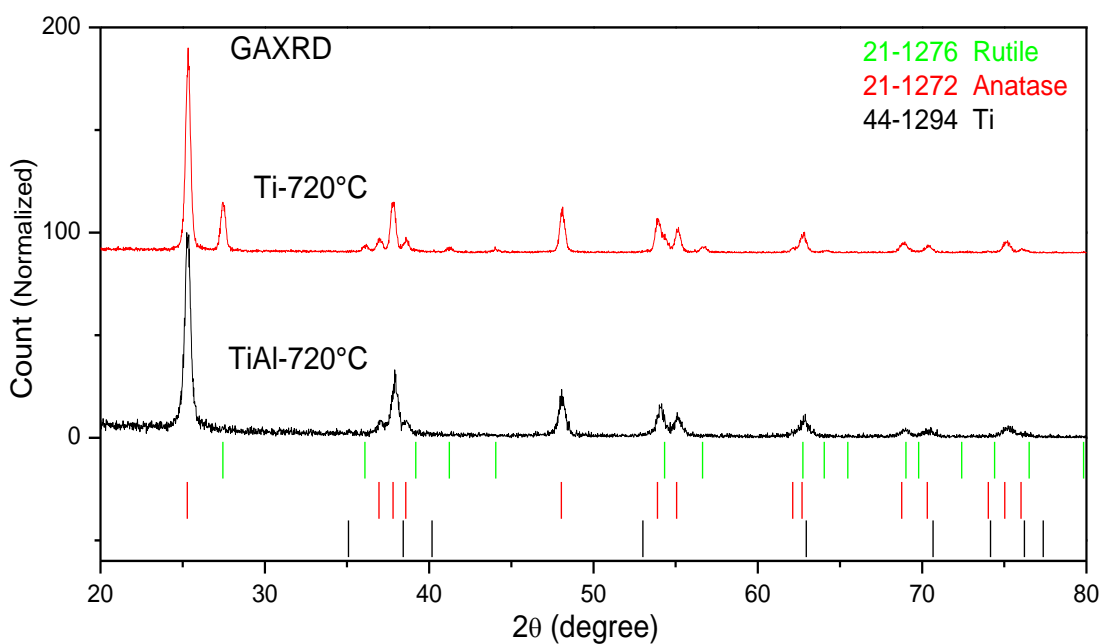


**Figure 5.11 :** The comparison of GAXRD patterns of Ti and TiAl anodic oxides in the presence of metallic film underneath the nanotube layer which were obtained after the heat treatment at  $720^\circ\text{C}$

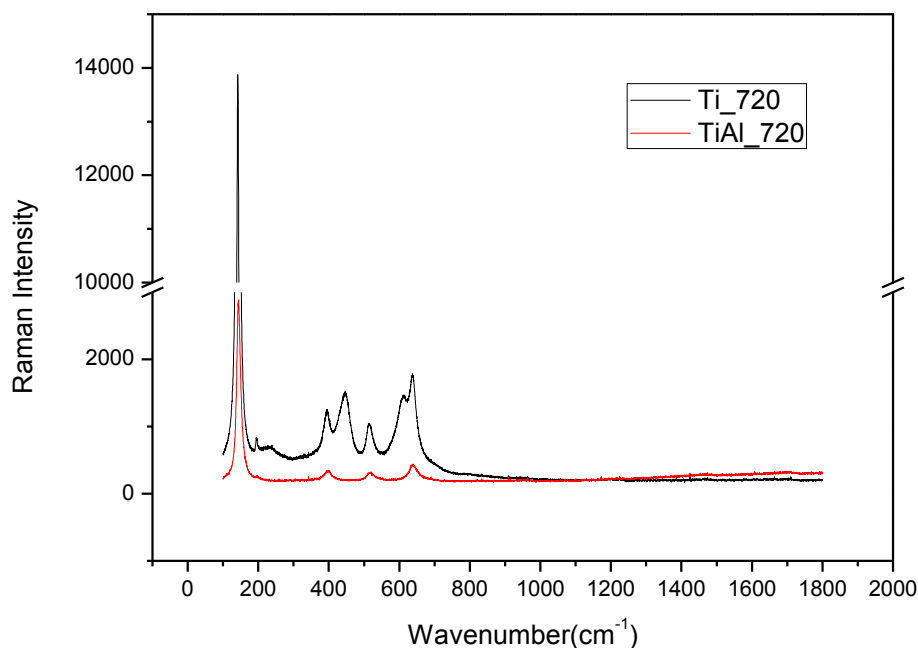


**Figure 5.12 :** The comparison of Raman spectra of Ti and TiAl anodic oxides in the presence of metallic film underneath the nanotube layer after the heat treatment at 720 °C.

#### **Phase transformation in the absence of metallic film underneath the nanotubes;**

This sample consisted of only alumina substrate and nanotube layer since the metallic film above the alumina substrate was totally oxidized during anodization process (seen in Figure 4.4.). In Figure 5.13, the PXRD and GAXRD patterns of nanostructured TiAl anodic oxide were shown, respectively. According to these results, no rutile phase was detected in both PXRD and GAXRD results in TiAl anodic oxide samples without a metallic layer.

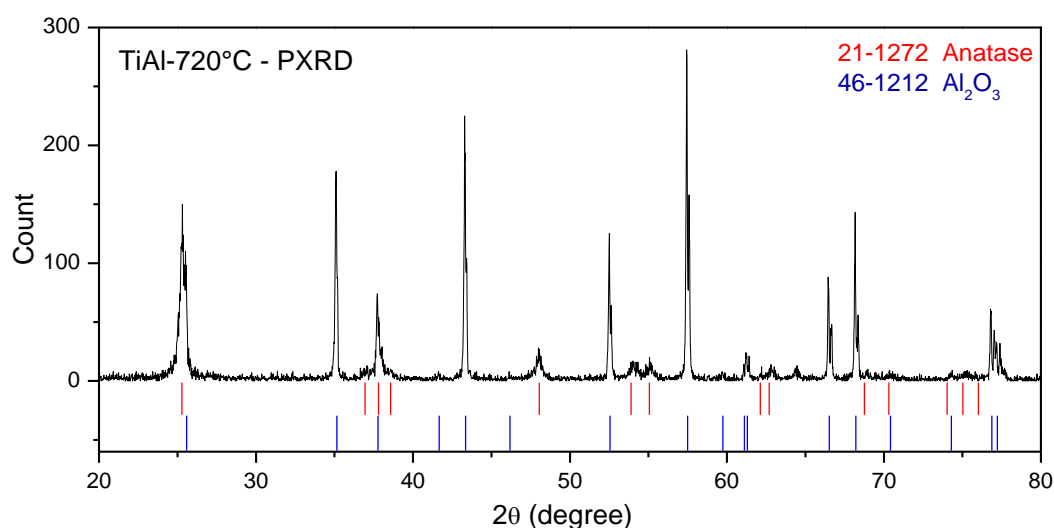


**Figure 5.13 :** The PXRD pattern of TiAl anodic oxide in the absence of metallic film underneath the nanotube layer which were obtained after the heat treatment at 720°C.

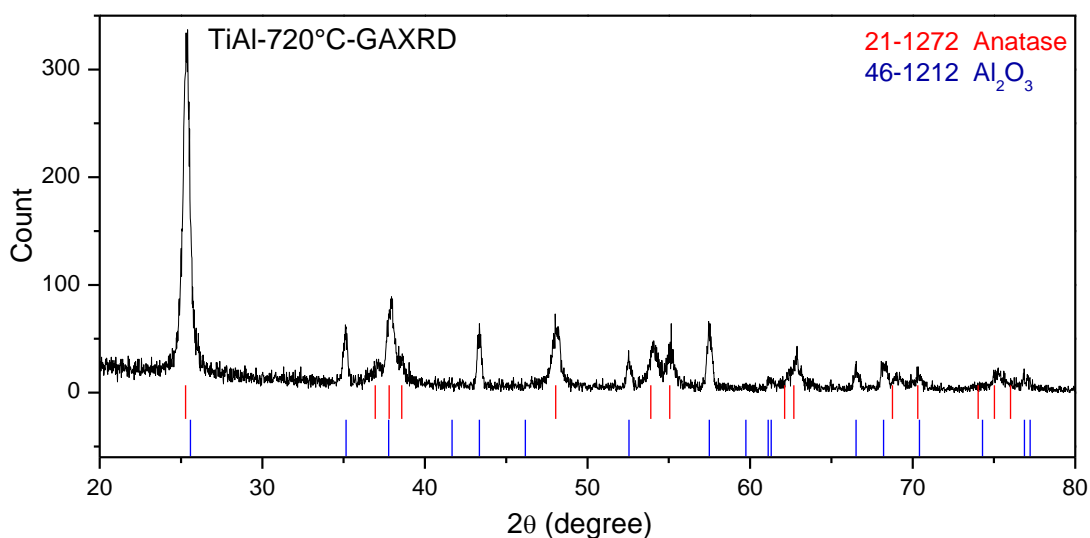


**Figure 5.14 :** The GAXRD pattern of TiAl anodic oxide in the absence of metallic film underneath the nanotube layer which were obtained after the heat treatment at 720°C.

According to the previous works in the literature [97,98], grain size of anatase particles has a critical role on the anatase to rutile transformation since this transformation requires a substantial amount of volume change. Thus for the transformation of nano scale anatase to rutile first anatase particles must reach to a critical size that will allow them to transform into larger volume rutile phase, which has a kinetically driven inhibition effect of this transformation. The transformation can be accomplished by the grain growth of anatase nano particles that are in contact to each other. Therefore during the grain growth of anatase particles transformation to rutile initiates at the anatase-anatase contact points. It is stated that the phase transformation of anatase nanopowders might start when an anatase particle becomes attached to a rutile particle [98].

Another mechanism is proposed for the case in which nanoscale anatase (such as nanotubes) are in contact with metallic titanium. Since metallic titanium does not have any volume restriction for the transformation of anatase to rutile, formation of rutile on metallic titanium is very easy. The rutile particles that are formed on the metallic film below the anodic oxide (barrier layer) when come into contact with the anatase, the conversion of anatase to rutile starts at this point. In nanotubular structures, anatase crystallites inside the walls are restricted and they have insufficient volume to rotate and reorient. Therefore, rutile nucleation inside the walls cannot occur easily due to the constraint induced by the nanotube walls. When the anatase crystallites inside the walls come into contact with the rutile crystallites at

the nanotube-metal film interface, small anatase grains get transformed into large rutile grains [97].

Our experimental results are in accordance with the literature, the phase analyses on nanostructured Ti and TiAl anodic oxides with and without a metallic film indicated that the presence of metallic film has a major contribution on anatase-rutile phase transformation. For samples with a metallic films below the nanoporous titania it became possible to initiate anatase to rutile transformation by heat treatment at 720 °C. The comparison of GAXRD and theta-2theta XRD measurements clearly indicated that this transformation has initiated at the barrier layer metal interface. For undoped titania the intensity of rutile phase peaks increased by the increase of the penetration angle of x-rays. This situation is far more clear for anodized TiAl. In this case rutile peaks were only observed in theta-two theta geometry clearly showing that the transformation is initiated at the oxide –metal interface. Another important conclusion that can be drawn from this result is the kinetic hinderance effect of Al doping on anatase-to rutile transformation. Another result supporting the requirement of metallic film beyond the anodic oxide for the transformation of anatase to rutile is obtained in experiments that are conducted for cases where there was no metallic film below the oxide. In this case it was not possible to convert anatase to rutile after heat treatment at 720 °C.

## 5.2 The Effect of Al Doping on TiO<sub>2</sub> Crystal Structure

In Al-doped TiO<sub>2</sub>, some of the peaks slightly shifted from TiO<sub>2</sub> anatase peak positions and these shifts were detected after the all heat treatment temperatures. As an example, the XRD pattern obtained after the heat treatment of TiAl anodic oxide at 600 °C was given in Figure 5.15. The shifts in TiO<sub>2</sub> anatase peak positions ( (103), (004), (112), (105), (204), (116) ) were also shown in high magnification in Figure 5.16. These slight shifts to the higher angles with respect to the original peak positions are the indication of decrease in d-spacing values. This result indicated that Al<sup>3+</sup> dopant entered into the anatase lattice owing to its smaller ionic radius compared to Ti<sup>4+</sup> and a solid solution was formed between Al<sup>3+</sup> ions and anatase TiO<sub>2</sub>. The presence of smaller ionic radius of Al<sup>3+</sup> ions in TiO<sub>2</sub> lattice causes a decrease in d value in crystal structure.

On the other hand, there was no shift in some of the anatase peak positions ( (101), (200), (211), (220), (107) ) and this situation can be explained by considering the crystal structure. In the case of  $\text{Al}^{3+}$  ions entering the tetragonal anatase crystal structure, “c” parameter decreased while “a” lattice parameter remained constant. This indicated that the shifts were observed in these planes are mainly affected from the changes in the dimensions of “c” axis [43,57]. In order to reveal the anatase planes that are affected from “c” lattice parameter, a simulation study was performed. For this simulation, Mercury 3.0 software and the Least Square Regression method were used. In this simulation “a” lattice parameter of tetragonal anatase  $\text{TiO}_2$  was kept constant and “c” parameter was reduced by 10%. The simulated pattern is given in Figure 5.17. Both the experimental XRD pattern of TiAl anodic oxide (Fig. 5.15) and the simulated pattern (Fig. 5.17) have the same characteristics, while the a-axis related peaks are in the same position, c axis related ones shifted to higher angles.

Using the same method, the experimental XRD pattern of TiAl anodic oxide was also simulated and the peak positions were calculated. The simulated and the experimental peaks in XRD pattern of TiAl anodic oxide (heat treated at 600 °C) are given in Figure 5.18. As a result of this simulation, it is found that Al dopant exhibits its main effect on c axis and “c” lattice parameter is decreased from 9.5139 Å to 9.4624 Å by the addition of Al dopant. This result also confirms that entry of aluminum into the lattice of anatase resulted in changes only on the “c” axis of tetragonal phase.

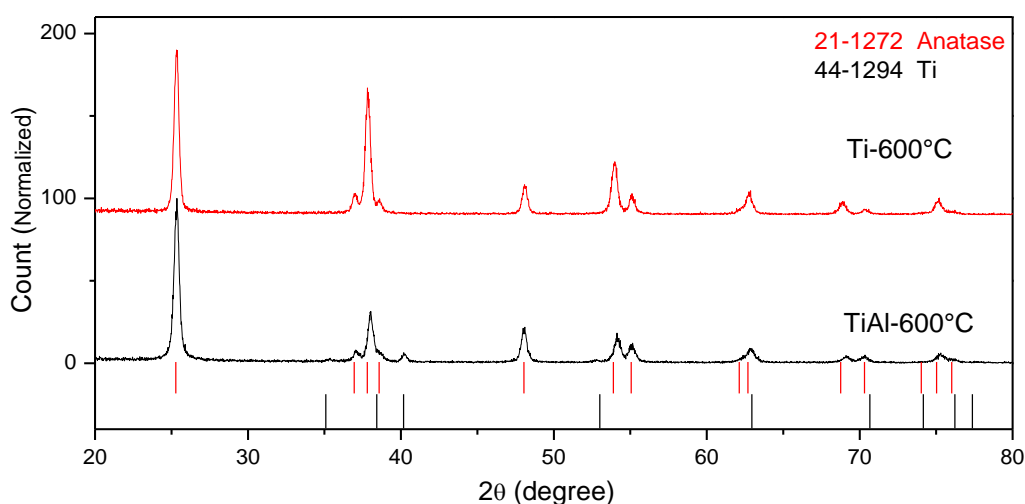


**Figure 5.15 :** The shifts in  $\text{TiO}_2$  anatase peak positions after the heat treatment of TiAl anodic oxide at 600°C.

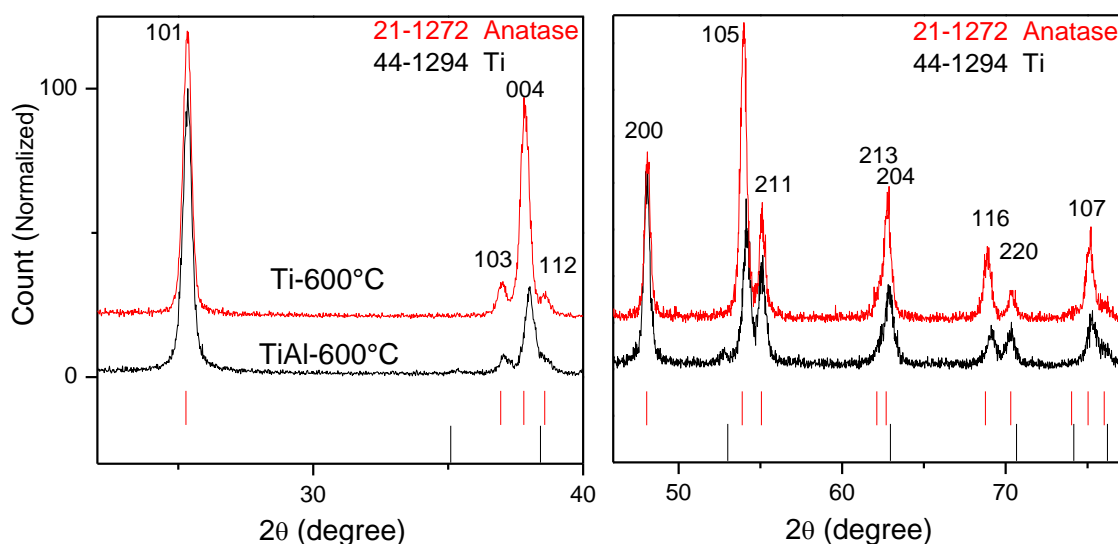


**Figure 5.16 :** The observed shifts in TiO<sub>2</sub> anatase peak positions after the heat treatment of TiAl anodic oxide at 600°C in high magnification.

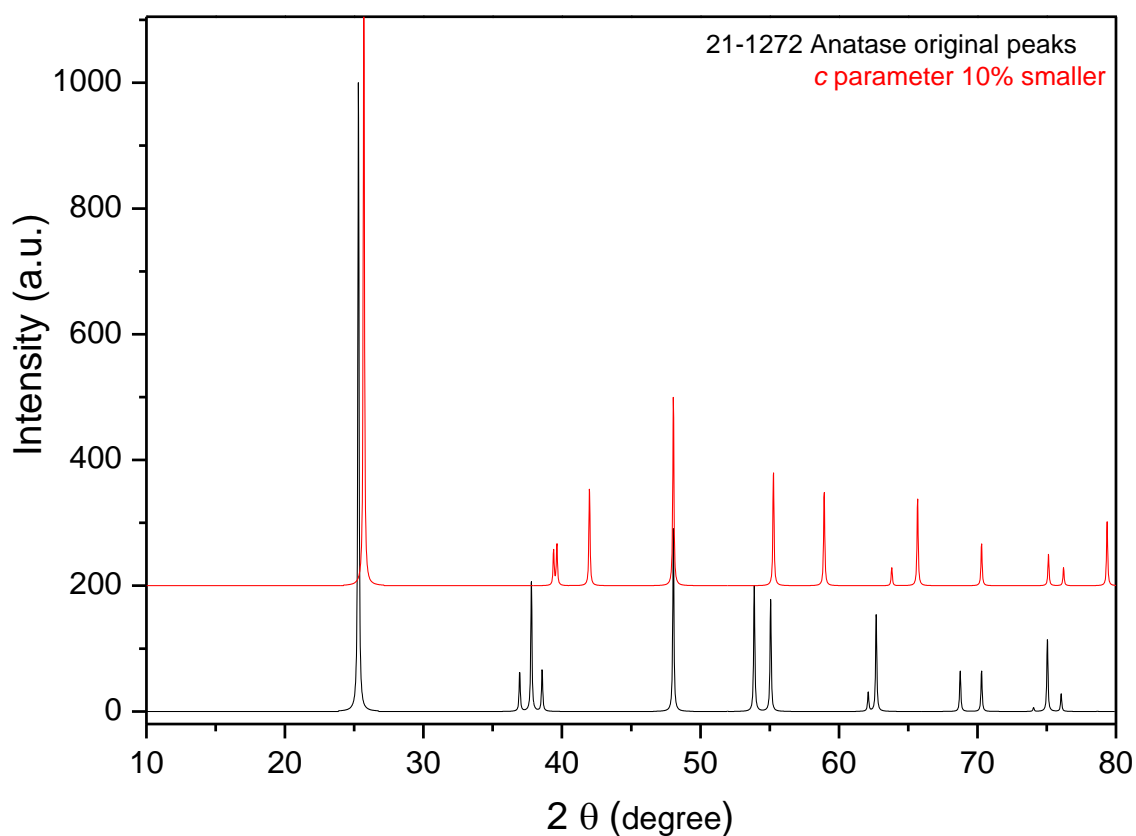


**Figure 5.17 :** The comparison of original TiO<sub>2</sub> anatase peak positions and the calculated TiO<sub>2</sub> anatase peak positions if "c" parameter is taken 10% less than the original values.

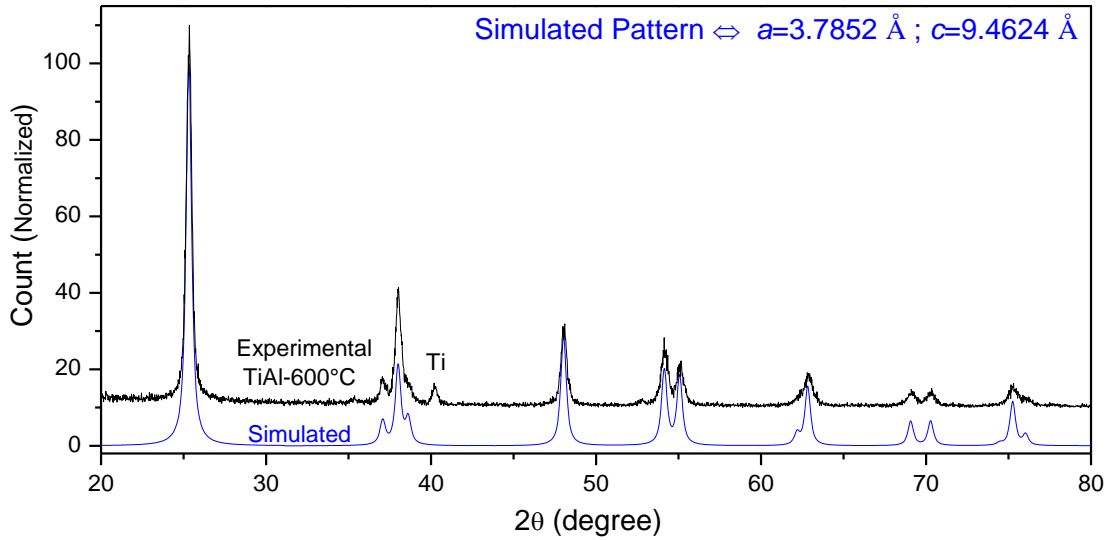


**Figure 5.18 :** The comparison of GAXRD pattern of heat treated TiAl anodic oxide and the simulated pattern

### 5.3 The Role Al Dopant on Grain Size

Al dopant restricts the grain growth [35,44,59,] and as well as particle growth [35,58,62]. depending on amount of dopant. In order to investigate the influence of Al doping on grain growth, the crystallite sizes of heat treated Ti and TiAl anodic oxides were calculated using the Scherrer formula (given in Equation 5.1). The Pseudo Voigt function was used for fitting the most intense anatase peak (101).

Reasonable peak fits were obtained in both cases as seen in Figure 5.19 and Figure 5.20. It is directly seen from the FWHM values, that the Al-doped TiO<sub>2</sub> sample has broader peaks which indicates smaller crystallite size. The calculated values for TiO<sub>2</sub> and Al-doped TiO<sub>2</sub> samples are, 23.7 nm and 20.3 nm, respectively. Although, results seem close to each other, the Al-doped TiO<sub>2</sub> sample has definitely smaller crystallite size. The same method was applied for the higher angle peaks and similar results were obtained. It can be concluded that addition of Al has an inhibiting effect on grain growth.

$$D = \frac{K\lambda}{\beta \cos \theta} \quad (5.1)$$

In equation, D denotes the mean crystallite size (Å), K is the shape factor (taken 0.9),  $\lambda$  is the X-ray Wave Length (Cu K $\alpha$  = 1.5418 Å),  $\beta$  is FWHM (in radians) and  $\theta$  is the diffraction angle.

#### 5.4 The Effect of Al Doping on Anatase-Rutile Transformation

The results of the investigations showed that the anatase-rutile phase transition occurred at about 720 °C in nanostructured Ti anodic oxide. However, this phase transition was kinetically hindered by the addition of Al doping into TiO<sub>2</sub> structure. It was also observed that “c” parameter decreased by the entry of Al ions into the anatase lattice. These results are closely related to the location of Al<sup>3+</sup> ions in TiO<sub>2</sub> lattice structure. Many controversial information have been published about the structure of Al or Al<sub>2</sub>O<sub>3</sub> doped TiO<sub>2</sub> crystal lattice. According to these studies, there are mainly three possibilities for accommodating Al<sup>3+</sup> in TiO<sub>2</sub> lattice. Since the ionic radius of Al<sup>3+</sup> (0.050 nm) is smaller than that of Ti<sup>4+</sup> (0.068 nm), Al ions may get located at Ti substitutional sites [35,55,64,99,100,] interstitial sites [59,64,99,100], a combination of both sites, or substitutional sites in combination with oxygen vacancies [64]. If Al<sup>3+</sup> ions with lower valence and smaller radius occupy Ti substitutional positions in TiO<sub>2</sub> anatase lattice, the charge neutrality of lattice is affected. In order to compensate the charge neutrality, oxygen vacancy concentration is increased and this leads to promotion of the anatase-rutile transformation through increase in lattice relaxation [35,37,55,63]. However, our results do not confirm this proposed assumption. In the case of Al<sup>3+</sup> ions are inserted at the interstitial sites, literature suggested that lattice contraction largely in c direction may occur without affecting the charge neutrality. This lattice constraint may result in lattice stabilization and consequent inhibition the transformation [37]. This assumption most likely better describes our experimental results. As in this assumption, lattice constraint occurs in c direction in nanostructured TiAl anodic oxides and also anatase to rutile transformation is kinetically hindered.

In addition, there is another study suggesting the inhibiting effect of Al<sup>3+</sup> on the phase transformation in both cases (Al<sup>3+</sup> location at substitutional or interstitial sites). According to this study, if Ti<sup>4+</sup> is substituted by Al<sup>3+</sup>, half an oxygen vacancy (lattice relaxation) and a Ti<sup>3+</sup> interstitial (lattice constraint) are created as seen in the equation 5.2, thereby promoting and inhibiting the phase transformation, respectively. However, the promoting effect is bigger than inhibiting effect. On the other hand, if Al<sup>3+</sup> ions occupy Ti<sup>3+</sup> interstitial sites, there is only inhibiting effect owing to the lattice constraint [37]. This proposed mechanism may also explain the results of investigations on nanostructured TiAl anodic oxides.



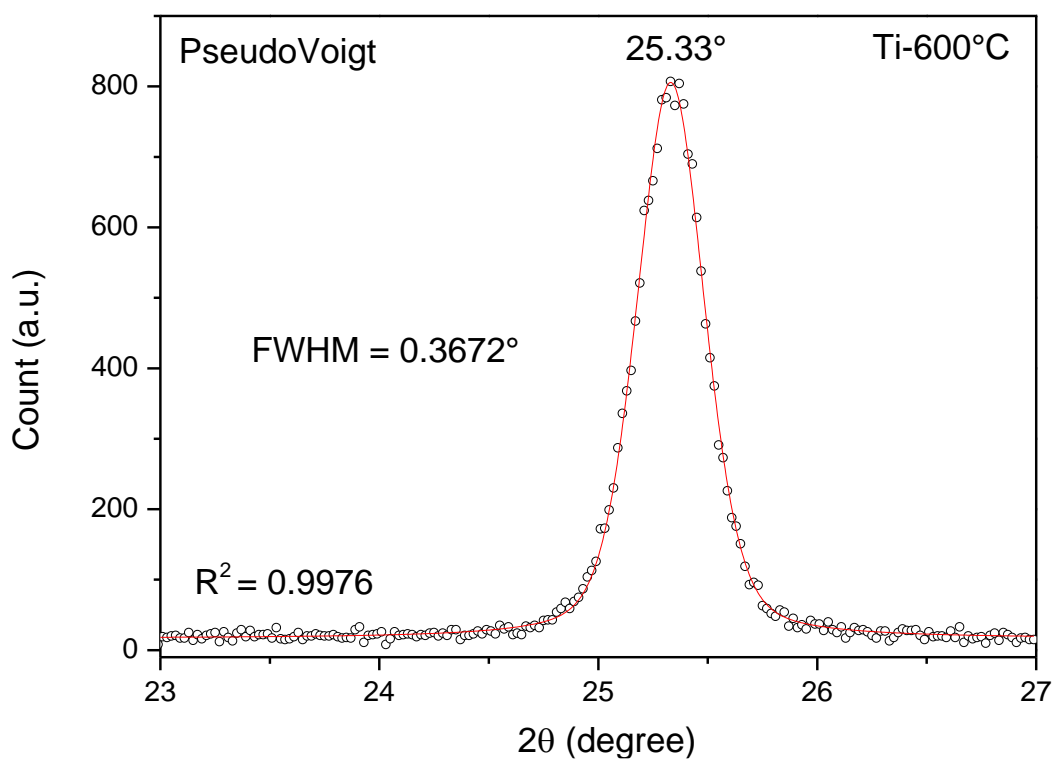


**Figure 5.19 :** The peak fitting for the calculation of the crystallite size of Ti anodic oxide which was heat treated at 600°C.

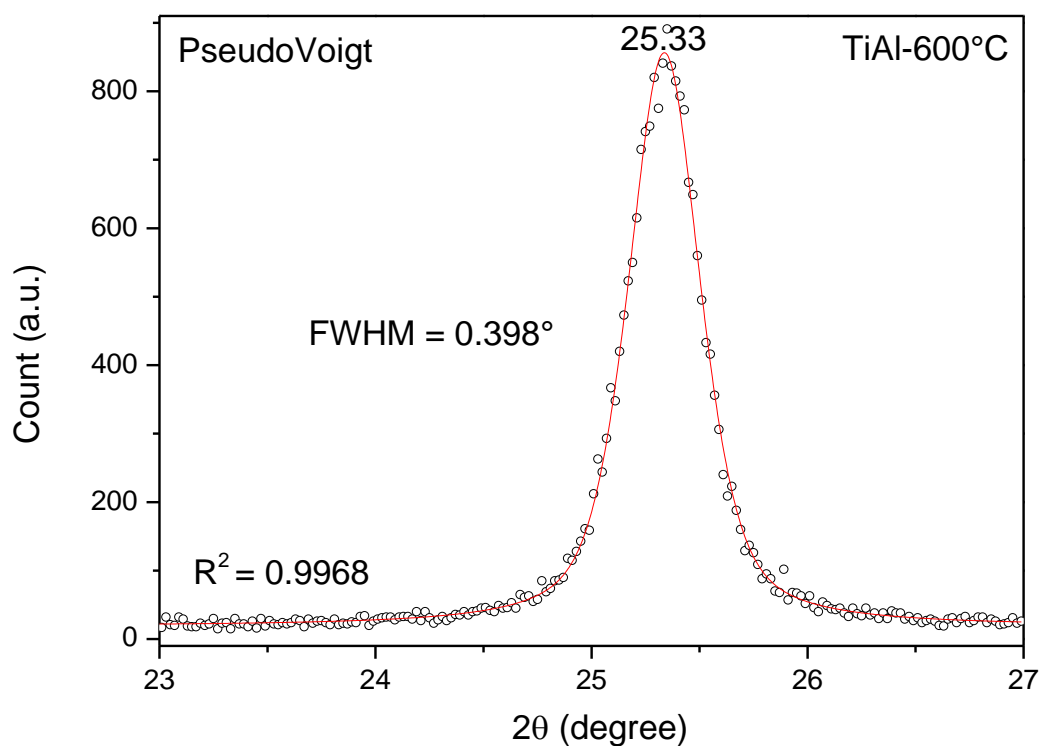
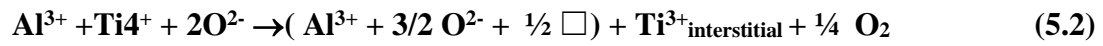


**Figure 5.20 :** The peak fitting for the calculation of the crystallite size of TiAl anodic oxide which was heat treated at 600°C.

The similar mechanism may occur in nanostructured TiAl anodic oxides.



( $\square$  denotes an oxygen vacancy) [37].

All these heat treatment investigations showed that 3 parameters mainly affect the anatase to rutile transformation in nanostructured anodic oxides. These are;

- Nano-sized rigid structure
- The presence or absence of metallic film underneath the nanotubes,
- Addition of Al dopant.

## 6. H<sub>2</sub> SENSING PROPERTIES OF NANOSTRUCTURED Ti AND TiAl ANODIC OXIDES

### 6.1 Fabrication and Characterization of Sensor Electrode Materials

In the fabrication stage of sensors, first, TiAl metallic coatings consisting 9 wt % Al were deposited on alumina substrates at 100 V bias voltage using the cathodic arc based technique (The SEM image of the corresponding coating is given in Section 3, Figure 3.20). Subsequently, nanotubular structures were formed on the surface of TiAl thin film coatings by anodizing the coatings at 60 V and 21 °C for 40 minutes in ethylene glycole electrolyte consisting 0.25 wt % NH<sub>4</sub>F and 1.6 vol % water. In Figures 6.1. and 6.2, the surface and cross sectional SEM images of nanotubular structures formed on TiAl coatings were presented, respectively. This sample consisted of only alumina substrate and nanotube layer since the metallic TiAl film above the alumina substrate was totally oxidized during anodization process. The produced nanotubes have diameters ranging from 60 nm to 80 nm and the lengths of nanotubes are approximately 5 microns.

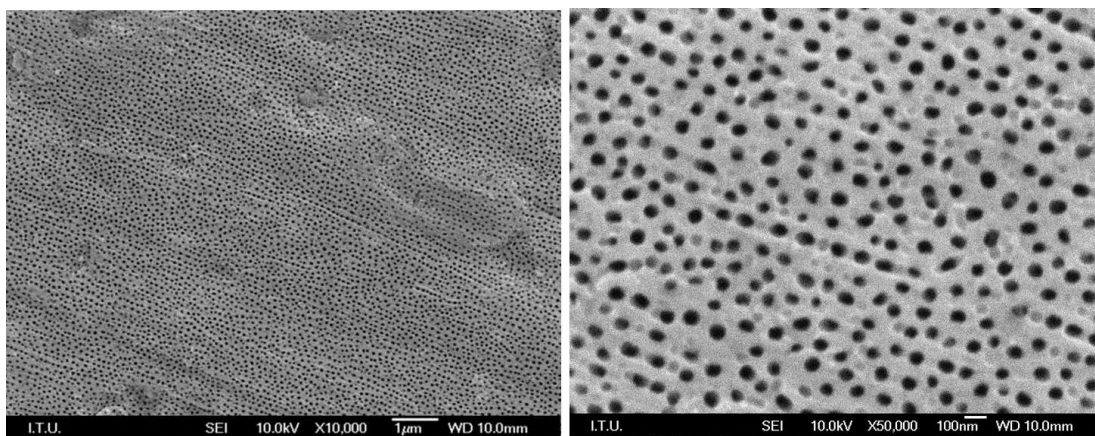


**Figure 6.1 :** The surface SEM image of nanotubular structure formed on TiAl surface after anodic oxidation at 60 V in 1.6 vol % water and 0.25 wt % NH<sub>4</sub>F containing electrolyte at 21°C.

Then the porous anodized TiAl structures were subjected to heat treatment at 450 °C for 3 hours to obtain crystallized anatase nanostructures. XRD analyses showed that

the amorphous nanotube structures completely transformed to anatase phase after this heat treatment.

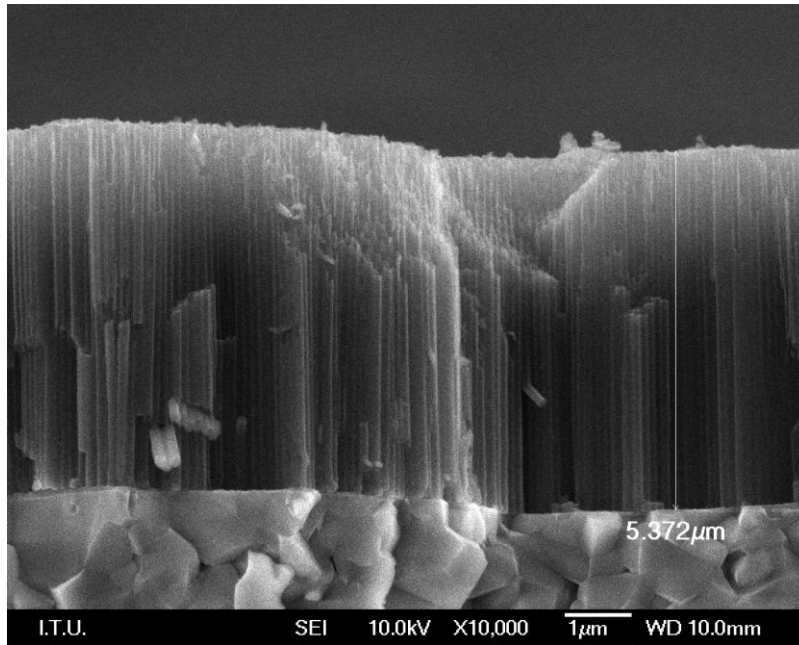


**Figure 6.2 :** The cross sectional SEM image of nanotubular structure formed on TiAl surface after anodic oxidation at 60 V in 1.6 vol % water and 0.25 wt %  $\text{NH}_4\text{F}$  containing electrolyte at  $21^\circ\text{C}$ .

Finally, the sensor fabrication was completed by placing Pt electrodes on the surface of nanostructured coatings. These Pt electrodes serve as electrical contacts in produced gas sensor and exhibits a catalyst effect in activating the adsorption and dissociation of hydrogen molecules [1,73,77]. In this step, two parallel Pt contact pads (13mm x 2mm in size) were deposited on the surface of masked nanotubes using magnetron sputtering technique as presented in Figure 6.3. The spacing between two Pt contact pads is 2 mm.

## 6.2. Hydrogen Sensing Behavior of the Nanotubular TiAl Oxide Sensor

The significant parameters that characterizes the sensing behavior of a sensor material are sensitivity, response time and recovery time, selectivity and long term stability.

The sensitivity value of the sensor was calculated from the resistance vs. time graph using the following equation.

$$S = \frac{R_0}{R_g} \quad (6.1)$$



**Figure 6.3 :** The image of the fabricated nanotubular TiAl oxide sensor after placing the Pt electrodes on the surface.

In this equation,  $S$  symbolizes sensitivity and it is the ratio of the resistance zero to resistance  $g$ .  $R_0$  is the point where the resistance of sensor against recovery gas is stable and  $R_g$  is the point where the resistance of sensor against the mixture gas consisting analyte gas and carrier gas.

From the resistance vs. time graphs of the sensor, the response times, that required to reach 10% of the initial resistance value upon gas exposure was calculated using the following equation (6.2). According to this equation, first the difference between  $R_0$  and  $R_g$  was found and this value was accepted as 100% and then  $d_{90\%}$  (90% of this difference according to equation) was calculated. The final result was subtracted from  $R_0$  and thus  $R_{90\%}$  value was found. The durations of  $t_{90\%}$  and  $t_0$  which corresponds to  $R_{90\%}$  and  $R_0$ , respectively were determined from the response graph. The difference between  $t_{90\%}$  and  $t_0$  gave the response time.

$$\begin{aligned}
 d_{100\%} &= R_0 - R_g \\
 d_{90\%} &= (R_0 - R_g) \times 0.9 \\
 R_{90\%} &= R_0 - (R_0 - R_g) \times 0.9
 \end{aligned}
 \quad \text{Response Time} = t_{90\%} - t_0 \quad (6.2)$$

The recovery time is the time required for a sensor to switch back its resistance to the 10 % of the saturation value. The recovery times of the sensor was calculated using the following equation (6.3).

$$\begin{aligned} d_{100\%} &= R_0 - R_g \\ d_{90\%} &= (R_0 - R_g) \times 0.9 \\ R_{90\%} &= R_g + (R_0 - R_g) \times 0.9 \end{aligned} \quad \text{Recovery Time} = t_{90\%} - t_0 \quad (6.3)$$

Sensor tests were conducted at different temperatures since the adsorption/desorption of gas molecules at the surface of the sensor material are functions of temperature and so, sensitivity, selectivity and response time are dependent on not only the type of receptor, they also dependent on temperature. Therefore, by varying the operating temperature of the sensor, the sensing properties of sensor can be improved. For this purpose, the tests were performed at RT, 100°C, 200°C, 250°C, 300°C and 350°C. The calculated sensor parameters for all the operating temperatures were given in Table 6.1.

The room temperature behavior of the sensor on exposure to various concentration of H<sub>2</sub> (50 ppm, 100 ppm, 300 ppm, 500 ppm, 1000 ppm and 2500 ppm H<sub>2</sub>) was given in Appendix Figure 1. In this resistance vs. time plot, the initial resistance is of the order of 653 kilohm in dry air and drops to about 623 kilohm when exposed to 50 ppm of hydrogen. The magnitude of the gas response increased gradually with increasing H<sub>2</sub> concentration from 50 ppm to 2500 ppm. According to the calculated values given in Table 6.1, the sensitivity value was slightly increased with increasing gas concentration at RT. The response times were prolonged at RT, however they were getting better for higher concentrations. The recovery times at RT was increasing as the gas concentration was increased. This result may be due to the desorption mechanism of H<sub>2</sub> molecules on the nanotubular TiO<sub>2</sub> surface at this operating temperature. In addition, some hydrogen atoms may remain in the nanotubular structure and these trapped hydrogen atoms may prolong the sensor recovery.

At an operating temperature of 100°C, the sensor exhibited a regular response graph when exposed to alternating atmospheres of Ar containing hydrogen and air. The sensitivity values calculated at 100°C were slightly increased compared to the values at room temperature. The concentration dependence of the H<sub>2</sub> gas response in the

sensor was clearly observed in Figure 6.4. The sensor completely recovers after H<sub>2</sub> flow was terminated and the needed recovery time for the sensor considerably decreased.

**Table 6.1 :** Calculated sensor parameters for nanotubular TiAl anodic oxide sensor for different hydrogen concentrations at RT, 100°C, 200°C, 250°C, 300°C and 350°C.

Temperature (°C)	Gas Concentration (ppm)	Sensitivity	Response Time (sec)	Recovery Time (sec)
RT	50	1.05	643	120
	100	1.11	576	135
	300	1.12	405	156
	500	1.14	386	177
	1000	1.15	346	185
	2500	1.17	340	196
100 °C	50	1.12	638	115
	100	1.45	609	45
	300	1.77	574	90
	500	1.93	526	40
	1000	2.2	475	45
	2500	2.8	429	30
200 °C	50	78	357	56
	100	51	261	31
	300	62	181	25
	500	80	190	15
	1000	100	186	11
	2500	152	210	10
250 °C	50	48	114	5
	100	93	100	5
	300	140	75	8
	500	158	65	9
	1000	175	45	4
	2500	203	40	4
300 °C	50	117	105	7
	100	166	75	10
	300	203	44	10
	500	226	50	3
	1000	239	40	3
	2500	268	40	5
350 °C	50	133	109	21
	100	169	60	65
	300	200	65	10
	500	236	35	11
	1000	255	33	5
	2500	305	30	5

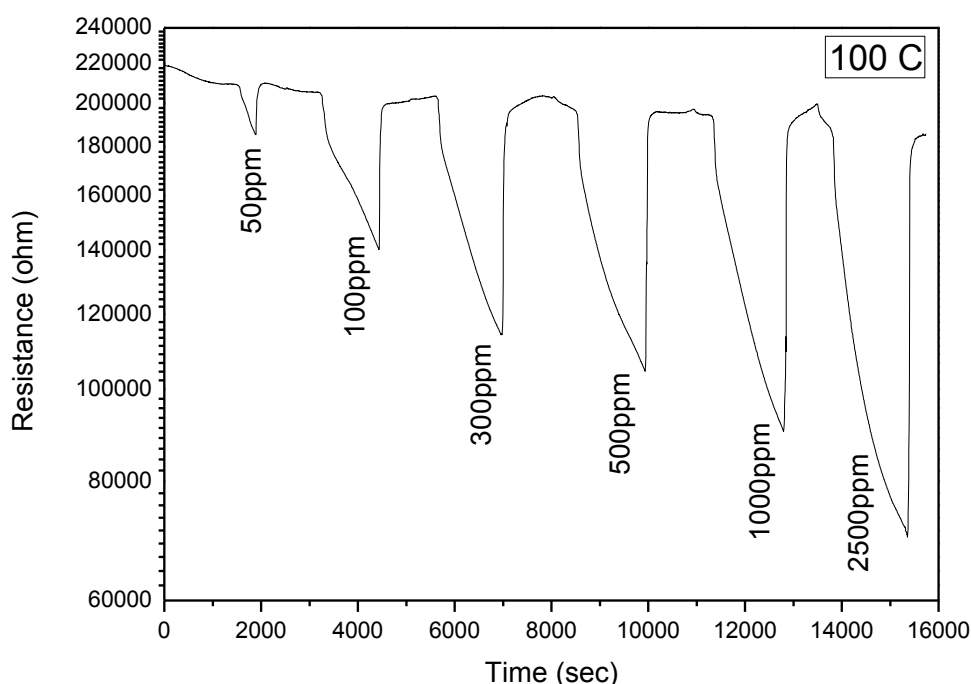


**Figure 6.4 :** The response graph of the nanotubular TiAl anodic oxide against different H<sub>2</sub> concentrations at 100°C.

At 200°C, the sensitivity values significantly increased compared to that calculated at RT and 100°C. While the calculated sensitivity values were in the range of 1-2.8 at RT and 100°C, these values reached to 152 at 200°C. On exposure to 50 ppm hydrogen a rapid reduction in resistance from 83 kilohm to 1 kilohm was observed (The response graph is given in Appendix Figure 2). The response times were getting better with increasing gas concentration at 200°C. The resistance of sensor regained its original level after the hydrogen flow shut-off and the recovery times decreased to 10 sec at 2500 ppm. The sensor showed good repeatability and high stability. When the operating temperature was increased to 250°C, the sensitivity values significantly increased compared to lower temperatures than 250°C. The magnitude of the gas response to 2500ppm was 203, which was approximately 200 times larger than the values calculated at RT and 100°C. Figure 6.5. depicted the variation of sensor resistance with the variation of hydrogen concentration at 250°C. While the concentration dependence behavior of the sensor was obviously seen at lower concentrations, this dependence was decreased at higher concentrations. Fast, regular and repetitive response graphs were obtained at this temperature. The response time decreased to 40 sec at 2500 ppm and the recovery times varies between 4-9 sec at all H<sub>2</sub> concentrations. It is also a good property of this sensor that it completely recovered after H<sub>2</sub> flow was terminated.



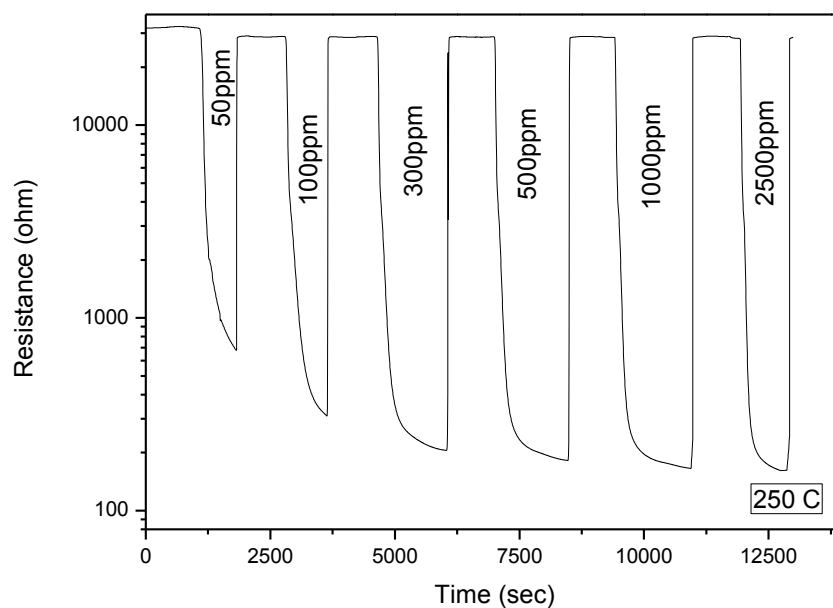


**Figure 6.5 :** The response graph of the nanotubular TiAl anodic oxide against different  $H_2$  concentrations at 250°C.

At an operating temperature of 300°C, higher sensitivity values and significantly lower response and recovery times were obtained. According to the response graph represented in Figure 6.6, the sensor exhibited a factor of 268 change in measured electrical resistance upon exposure to 2500 ppm hydrogen. The response times decreased to 105 sec to 40 sec as the gas concentration increased. The recovery of sensor took very short time and the sensor completely recovered for 3-10 sec after  $H_2$  flow was terminated.

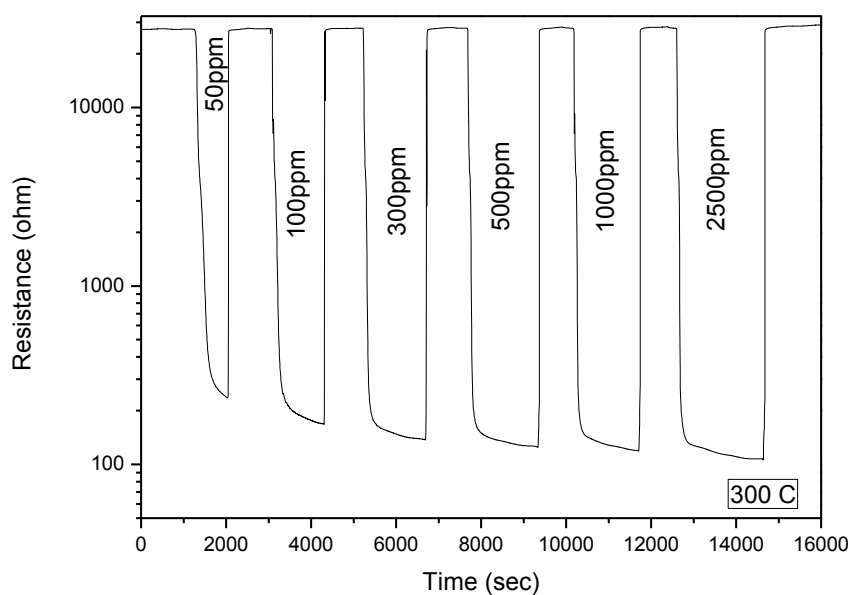


**Figure 6.6 :** The response graph of the nanotubular TiAl anodic oxide against different  $H_2$  concentrations at 300°C.

Lastly, hydrogen gas sensing performance of the sensor was tested at 350°C and the response graph of the sensor was given in Appendix in Figure 3. Similar to 300°C, higher sensitivity values were obtained and the calculated sensitivity value at 2500 ppm raised to 305. The sensitivity to hydrogen increased with operating temperature up to 350°C, however the recover resistance increased gradually at 350°C. The sensor demonstrated quick response and recovery behavior. In addition the concentration dependence behavior of sensor decreased obviously.

### **6.3. Evaluation and Discussion of the Sensor Measurement Results**

In literature there are many studies reporting the H<sub>2</sub> sensing performance of the TiO<sub>2</sub> sensors. In Table 6.2. H<sub>2</sub> sensing properties of the TiO<sub>2</sub> sensors produced by various techniques were summarized. These sensors exhibited a wide variation in sensitivity values depending on operating temperature, H<sub>2</sub> gas concentration, test ambient and the fabrication method of the TiO<sub>2</sub> sensor material. Among TiO<sub>2</sub> sensors, nanostructured ones demonstrate high gas sensing performance and improvement in the sensor characteristics. However, nanostructured TiO<sub>2</sub> sensors exhibit higher resistance values in air ambient. The reported resistance values for nanotubular TiO<sub>2</sub> sensors in air ambient are in the range of 50 Megaohm-1Gigaohm at RT and 400 Megaohm at 290°C [66,68,72]. Although their initial resistances are high and they may show very high response towards H<sub>2</sub> gas, their resistances can drop below the detection limit which may lead to problems in concentration dependent sensing. The increase in electrical conductivity of a TiO<sub>2</sub> sensor may cause an increase in sensor stability and sensitivity [52]. In order to improve the electrical properties and microstructural properties of TiO<sub>2</sub>, certain amount of suitable dopants have been added to TiO<sub>2</sub> material [49-51] and Al dopant can be considered as one of these dopants since the presence of Al species in TiO<sub>2</sub> lattice leads to band gap narrowing [58-60]. In the literature, addition of Al or Al<sub>2</sub>O<sub>3</sub> to bulk TiO<sub>2</sub> leads to an increase in sensing or selectivity property of TiO<sub>2</sub> against different gases. Adding 7.5 wt% Al increased the O<sub>2</sub> and CO gas sensitivities [35], 5 wt% Al<sub>2</sub>O<sub>3</sub> (with 0.5 wt% Pd) increased H<sub>2</sub>S gas sensitivity [51] and 10 wt% Al<sub>2</sub>O<sub>3</sub> improved the H<sub>2</sub> gas sensitivity and selectivity of TiO<sub>2</sub> sensor [36].

In the present study, the electrical resistance of TiO<sub>2</sub> decreased to lower values by using Al dopant and the electrical conductivity provided by Al doping may cause an

increase in the sensor stability and sensitivity. The produced nanotubular TiAl oxide sensor exhibits good responses towards  $H_2$  gas at all operating temperatures. The sensitivity values of the sensor increase with increasing operating temperature as depicted in Figure 6.7. Above  $100^\circ\text{C}$ , the sensitivity increases rapidly with temperature due to the chemical adsorption (chemisorption) takes place. Since high activation energy is required for chemisorption process, this type of adsorption can occur at high temperature. This chemisorption process led to generation of high amount of electrons in the titania matrix and increased the sensitivity of sensor in the beginning. Then the increase in sensitivity with temperature is beginning to reach limiting value. This behavior of sensor is also consistent with the temperature dependent chemisorption process illustrated in Figure 6.8. (A decrease in sensitivity is also expected as the temperature rises according to chemisorption mechanism) The produced sensor can also detect the hydrogen gas at low temperatures due to it has extended surface area, however, the sensitivity values of sensor at RT and  $100^\circ\text{C}$  are lower than the values obtained at high temperatures.

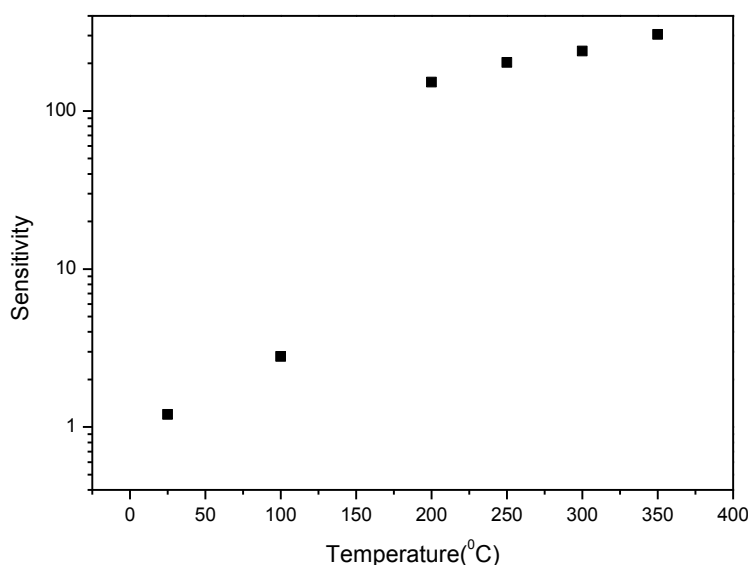


**Figure 6.7 :** The temperature dependence of sensor sensitivity upon exposure to 2500ppm hydrogen.

The prepared sensor is also sensitive to the variations in hydrogen gas concentration and its sensitivity increases as the gas concentration increases. It can detect even lower concentrations of  $H_2$  gas in carrier gas and demonstrate considerable resistance drop upon exposure to 50 ppm  $H_2$  gas. While the concentration dependence behavior of the sensor was obviously seen at all  $H_2$  concentrations up to  $250^\circ\text{C}$ , this behavior began to disappear after  $250^\circ\text{C}$  especially at higher concentrations. This result may

indicate that monomolecular layers were formed on the sensor surface during the chemisorption of hydrogen atoms. When the hydrogen atoms covered all the surface of sensor and occupied all the adsorption sites, the sensor saturated the gas concentration and the concentration dependence of the sensor began to decrease.

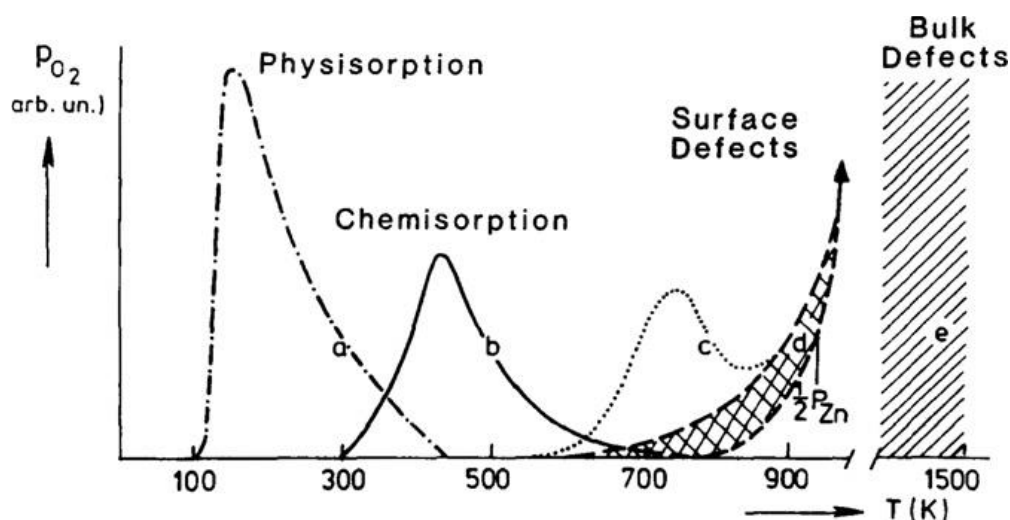


**Figure 6.8 :** The interactions between the surface and the gas phase depends on temperature [101].

The response times of nanotubular TiAl oxide sensor are getting better with increasing gas concentration and the recovery of the sensor takes very short time at all temperatures. After 200°C, the calculated response times and recovery times decreased to 30-100 sec and 3-10 sec, respectively, depending on H<sub>2</sub> gas concentration. It can be concluded that the optimum operating temperature for maximum sensor response was determined as 300°C since high sensitivity, lower response and recovery times without any hysteresis were obtained at this temperature. It is also a good property of this sensor that it shows good repeatability and high stability after a long term usage.

As a result of the sensor measurements, the hydrogen sensing performance of nanotubular TiAl oxide sensor was investigated at operating temperatures in the range of 25°C-350°C and the sensor showed sensitivity towards hydrogen gas at all temperatures. The addition of Al caused a decrease in the initial resistance of the sensor in air ambient compared to TiO<sub>2</sub> sensors. Therefore, the drastical drop in sensor resistance is not observed in concentration dependent measurements and the sensor can operate successfully. The sensing mechanism is driven by chemisorption process and this process leads to rapid increase in sensor sensitivity above 100°C. When the hydrogen atoms occupy all adsorption sites on the surface of sensor, the

sensor begins to saturate against hydrogen gas and the rapid increase in sensitivity slows down. In addition, the sensor shows quick response and recovery as the operating temperature rises. It also exhibits repetitive responses and remain stabil after a long-term usage.

**Table 6.2 :** H<sub>2</sub> sensing properties of the TiO<sub>2</sub> sensors produced by various techniques.

Sensor Material	T(°C)	Gas Concentration	Sensitivity	Test Ambient	Response Time	Recover Time
Pd or Pt/ Titanate NT supported on gamma-Al <sub>2</sub> O <sub>3</sub> catalytic gas sensor Han et al.	250 °C	500ppm	0.05	H <sub>2</sub> +Air / Air	5 sec	
Transparent TiO <sub>2</sub> NT+10nm Pd layer (supported on a glass substrate) Mor et al.	RT	1000ppm	10 <sup>4</sup>	H <sub>2</sub> +N <sub>2</sub> / N <sub>2</sub>	30 sec	
Electrochemically etched porous titania S.K. Hazra et al.	250°C	1000ppm	0.5-1.5	H <sub>2</sub> +Air / Air	21-74 sec	119-292
Nanostrucutred TiO <sub>2</sub> /PtO- Pt Dual layer films ( on glass substrate) X.Du et al.	180-200°C	20.000ppm	8	H <sub>2</sub> +Air / Air	600 sec	600 sec
TiO <sub>2</sub> NT (on Ti folyo)G.A.,Grimes et al.	290°C	500ppm	30	H <sub>2</sub> +N <sub>2</sub> / N <sub>2</sub>	600sec	
TiO <sub>2</sub> on AAO (substrate wafer coated SiO <sub>2</sub> ) C. Lu et al.	500°C	50ppm	50	H <sub>2</sub> +N <sub>2</sub> / N <sub>2</sub>	10 sec	10 sec
Tritanate-derived TiO <sub>2</sub> H.- S. Kim et al.	500°C	10.000ppm	10 <sup>4</sup>	H <sub>2</sub> +N <sub>2</sub> / N <sub>2</sub>	1-81 sec	
TiO <sub>2</sub> NT H. Miyazaki et al.	250°C	8.000ppm	2-185	H <sub>2</sub> +Air / Air	60-120sec	
TiO <sub>2</sub> NT K Gong et al.	RT	1.000ppm	10 <sup>8</sup>	H <sub>2</sub> +N <sub>2</sub> / Air		
TiO <sub>2</sub> thick film (on alumina) G. C. Mather et al.	500°C	100.000ppm	10 <sup>3</sup>	H <sub>2</sub> +N <sub>2</sub> / Air		
Porous TiO <sub>2</sub> thin film T. Mukherjee et al.	300°C	500ppm	0.74	H <sub>2</sub> +N <sub>2</sub> / Air	254 sec	
TiO <sub>2</sub> NT O.K.,Varghese et al.	290°C	500ppm	10 <sup>2</sup> -10 <sup>3</sup>	H <sub>2</sub> +N <sub>2</sub> /Air	200 sec	
TiO <sub>2</sub> NT (with Pd) G.K. Mor et al.	RT	1.000ppm	10 <sup>3</sup>	H <sub>2</sub> +N <sub>2</sub> /Air	417 sec	
TiO <sub>2</sub> NT E.Sennik et al.	RT	1.000ppm	10-20	H <sub>2</sub> +N <sub>2</sub> /N <sub>2</sub>	60sec	60sec
TiO <sub>2</sub> +10 wt% Al <sub>2</sub> O <sub>3</sub> mixture L.D., Birkefeld et al.	500°C	20.000ppm	10 <sup>3</sup>	H <sub>2</sub> +N <sub>2</sub> /Air	-	
AAO coated Pd thin film N.,Tasaltın et al.	RT	1.000ppm	1.5	H <sub>2</sub> +N <sub>2</sub> /Air	360 sec	
SnO <sub>2</sub> nanowire B., Wang et al.	300°C	1000ppm	3.25	H <sub>2</sub> +Air /Air	50-100sec	
Nanoporous Pd film D. Ding et al.	RT	250ppm	% 12	H <sub>2</sub> +N <sub>2</sub> /Air	240-300 sec	600 sec



## 7. CONCLUSION

The results of all investigations are summarized as in the below:

- The well-adherent and dense metallic Ti and TiAl thin films were deposited on alumina substrates using CAPVD method. This has been accomplished for the first time in this study. The pretreatment process applied before deposition generated heat on the surface of substrates by the effect of energetic ions and this heating provided good adhesion between substrate and coating.
- The main effects of different bias voltage on the resulting coating structures were investigated. The surface morphologies of all coatings altered with the increase in bias voltage. As the deposition bias voltage was increased, the columnar structure of coatings became denser and this resulted in a decrease in Ti and TiAl coating thicknesses. The aluminum content of the films showed dependence on the bias voltage. Coatings deposited at 0 V bias voltage had a similar Al content as the target material (25 at %). By the increase of bias voltage, the Al content decreased to a level 11-15 at %.
- The high bias voltage applied during post treatment caused a heating on the surface of coatings. Post treatment of the coating resulted in the densification of the coating structure. The columnar structure of coatings was converted into equiaxed structure by the effect of post treatment with high bias voltage. Surface morphologies of coatings were improved compared to the coatings without post treatment and smoother surfaces were obtained. However, internal stress formation was detected in the post treated Ti and TiAl coatings.
- There was no apparent effect of bias voltage increase on XRD patterns of Ti coatings. In the XRD patterns of TiAl coatings presence of  $\text{Ti}_3\text{Al}$  phase was detected. The amount of this phase increased with the aluminum content. The

rapid heat treatment supplied by the application of high bias voltage led to stabilize the meta-stable  $\text{Ti}_3\text{Al}$  phase in TiAl coatings.

- The droplet formation was observed on the coating surfaces induced from production method. For overcoming the detrimental effects of droplets on electrochemical reactions during anodization process, the coatings were subjected to pretreatments before anodization process.
- All the coatings produced by CAPVD method were anodized in ethylene glycol electrolyte without any spalling. This result confirms the assumption that CAPVD is a suitable method for producing coatings which are resistant to electrolytic processes.
- Among the coatings produced, two types of Ti and TiAl coatings were selected for the optimization of anodization studies. These are the coatings produced at -100 V bias voltage with and without high bias voltage post treatment. The coatings deposited at -100 V bias were selected due to their optimum coating thickness and relatively denser structure. Two versions of these coatings, with and without post treatment, were used since they have different morphological and structural properties. Therefore, the suitability and durability of these two different Ti and TiAl coating structures were tested for anodization process and the possible effects of post treatment on as grown nanoporous structure were investigated. Both these two different coating structures promoted the formation of highly ordered nanoporous-nanotubular structures on their surfaces. In post treated coatings crack formation induced by internal stresses was observed on the surface of anodized structures. Therefore, the coatings produced without post treatment was selected as the most appropriate coating structures for anodization process.
- Anodization processes were performed in the ethylene glycol electrolytes containing different amount of fluoride since the fluoride concentration is a key parameter in determining the kinetics of nanotube growth. Consequently, the optimal  $\text{NH}_4\text{F}$  concentration in ethylene glycol was determined as 0.61 wt % and 0.25 wt % for well-aligned and high thickness of nanotubes, respectively. Therefore, these electrolyte concentrations were



used in the subsequent detailed investigations about anodization of Ti and TiAl thin film coatings.

- The effects of anodization potential on nanostructure growth were investigated in 0.25 wt % and 0.61 wt %  $\text{NH}_4\text{F}$  containing electrolytes. In 0.25 wt %  $\text{NH}_4\text{F}$  containing ethylene glycol, nanotubular structure was successfully fabricated in a voltage window from 40 to 70 V. The diameter and the length of the nanotubes increased gradually with increasing anodization voltage until 65 V. So, the optimal anodization potential was determined as 60 V for growing longer nanotubes.
- The effects of temperature on nanotube length and surface morphology were investigated by anodizing the samples in a temperature range from 13 °C to 29 °C. As a result, extending nanotube length was obtained. Considering the effect of temperature on the surface morphology of the as-anodized coatings, the optimal anodization temperature was determined as 21 °C for obtaining highly ordered and as well as longer nanotubes.
- The content of water used in electrolyte is also significant parameter in the growth of nanotubes. 1.6 vol % is the highest water content for producing high thickness of nanotubes.
- The relation established between anodization time and nanotube growth length. In the earlier stages of anodization, nanotubes grow on TiAl surface more rapidly and then growth rate slows down. The conditions for total anodization of the metallic film above alumina were determined. These produced nanotubes with high thickness are thought to be appropriate for using as a sensor material since there is a possibility to occur a short circuit between Pt circuits and the conductive layer underneath the nanotubes.
- There was no considerable effect of agitation type on nanotube length under the same conditions.
- The nanotubes with high thickness and well-aligned nanotubes were formed on Ti coatings using the optimal anodization parameters for TiAl coatings. The effects of anodization parameters on as-grown  $\text{TiO}_2$  nanotubes were examined.

- The crystallization behaviors of nanostructured Ti and TiAl anodic oxides were investigated after heat treatments conducted at different temperatures from 280 °C to 720 °C.
- In TiAl anodic oxide, the addition of Al ions into TiO<sub>2</sub> structure cause a retardation in the temperatures of amorph-anatase and anatase-rutile phase transformations and there is no indication of rutile nucleation even after 720 °C. However, rutile peaks were appeared at a temperature of 720 °C in Ti anodic oxides.
- The nanostructured Ti and TiAl anodic oxides exhibited different behaviors in the presence and the absence of metallic film underneath the nanotube layer. The presence of metallic film favors the anatase-rutile phase transformation in the nanotube structure. The initial rutile nucleation occurs in the bulk metallic film at about 720 °C and when the anatase crystallites inside the nanotube walls come into contact with the rutile crystallites at the nanotube-metal film interface, small anatase grains get transformed into large rutile grains.
- In Al-doped TiO<sub>2</sub>, some of the peaks slightly shifted from TiO<sub>2</sub> anatase peak positions due to the presence of smaller ionic radius of Al<sup>3+</sup> ions in TiO<sub>2</sub> lattice. The indicated peak shifts were observed in the planes which are mainly affected from the changes in c axis. The anatase TiO<sub>2</sub> planes that are affected from “c” lattice parameter were revealed as a result of the simulation study. The experimental XRD pattern of TiAl anodic oxide was also simulated and the peak positions were calculated.
- The broader peaks indicating smaller crystallite size were detected in Al-doped TiO<sub>2</sub> sample. The crystallite sizes of heat treated Ti and TiAl anodic oxides were calculated using the Scherrer formula and definitely smaller crystallite size was calculated for Al-doped TiO<sub>2</sub>.
- The anatase-rutile phase transformation was observed at about 720 °C in nanostructured Ti anodic oxide. However, this phase transformation was kinetically hindered by the addition of Al dopant into TiO<sub>2</sub> structure.
- The heat treatment investigations indicate 3 parameters, which are mainly effective on anatase to rutile transformation. These are; rigid nano-sized

structure, the presence or absence of metallic film underneath the nanotubes and the addition of Al dopant.

- The resistance changes in nanotubular TiAl oxides were measured upon exposure the various concentration of H<sub>2</sub> gas in the temperature range of 25°C-350°C. Although the sensor showed sensitivity towards hydrogen gas at all temperatures, the best response graph was obtained at 300°C.
- The electrical conductivity provided by Al dopant and hence, the sensor operated successfully in concentration dependent measurements. The sensor sensitivity towards hydrogen gas was also increased by the addition of Al.
- The sensitivity values of the sensor increase with increasing operating temperature, however, the sensitivity increased rapidly above 100°C due to the chemisorption process occurred at this temperature. During this process, the trapped electrons are released back into the conduction band of the TiO<sub>2</sub> and the resistance of the sensor is decreased. When the hydrogen atoms occupy all adsorption sites on the surface of sensor, the sensor begins to saturate against hydrogen gas and the rapid increase in sensitivity slows down.
- The prepared sensor is also sensitive to the variations in hydrogen gas concentration and its sensitivity increases as the gas concentration increases. It can detect even lower concentrations of H<sub>2</sub> gas in carrier gas.
- The concentration dependence behavior of the sensor was obviously seen at all H<sub>2</sub> concentrations up to 250°C, this behavior began to disappear after 250 °C especially at higher concentrations.
- The sensor showed quick response and recovery as the operating temperature rises.
- The response times of nanotubular TiAl oxide sensor were getting better with increasing gas concentration and the recovery of the sensor took very short time at all temperatures. After 200°C, the calculated response times and recovery times decreased to 30-100 sec and 3-10 sec, respectively, depending on H<sub>2</sub> gas concentration.
- It is a good property of the sensor that it exhibited good repeatability and high stability after a long term usage.



## REFERENCES

- [1] Aswal, D.K. and Gupta, S.K. (2007). *Science and Technology of Chemiresistor Gas Sensors*. New York: Nova Science Publishers.
- [2] Comini, E., Faglia, G. and Sberveglieri, G. (2009). *Solid State Gas Sensing*. New York: Springer.
- [3] Carotta, M., Ferroni, M., Gherardi, S., Guidi, V., Malagù, C., Martinelli, G., Sacerdoti, M., Vona, M., Licoccia, S. and Traversa, E. (2004). Thick-film gas sensors based on vanadium–titanium oxide powders prepared by sol-gel synthesis. *Journal of the European Ceramic Society*, 24 (6), 1409-1413.
- [4] Seo, M., Yuasa, M., Kida, K., Huh, J., Shimanoe, K. and Yamazoe, N. (2009). Gas sensing characteristics and porosity control of nanostructured films composed of TiO<sub>2</sub> nanotubes. *Sensors and Actuators, B Chemical*, 137 (2), 513-520.
- [5] Serra, A., Filippo, E., Buccolieri, A., Giulio, M. and Mano, D. (2009). Self-assembling of micro-patterned titanium oxide films for gas sensors. *Sensors and Actuators, B Chemical*, 140 (2), 563-567.
- [6] Macak, J., Tsuchiya, H., Ghicov, A., Yasuda, K., Hahn, R., Bauer, S. and Schmuki, P. (2008). TiO<sub>2</sub> nanotubes: self-organized electrochemical formation, properties and applications. *Current Opinion in Solid State and Materials Science*, 11, 3–18.
- [7] Wang, J. and Lin, Z. (2009). Anodic formation of ordered TiO<sub>2</sub> nanotube arrays: effects of electrolyte temperature and anodization potential. *J. Phys. Chem. C*, 113, 4026–4030.
- [8] Kuang, D., Brillet, J., Chen, P., Takata, M., Uchida, S., Miura, H., Sumioka, K., Zakeeruddin, S.M. and Gratzel, M. (2008). Application of highly ordered TiO<sub>2</sub> nanotube arrays in flexible dye-sensitized solar cells. *Acsnano*, 2 (6), 1113–1116.
- [9] Mor, G. and Varghese, O. (2003). Fabrication of tapered, conical-shaped titania nanotubes. *J. Mater. Res.*, 18 (11), 2588-2593.
- [10] Yoon, J., Fan, M., Yang, D., He, H., Liu, D., Yuan, A., Zhu, J. and Chen, T. (2009). Application of immobilized nanotubular TiO<sub>2</sub> Electrode for photocatalytic hydrogen evolution: reduction of hexavalent chromium (Cr(VI)) in water. *Journal Of Hazardous Materials*, 161, 1069–1074.
- [11] Lin, F., Zhou, G., Li, Z., Li, J., Wu, J. and Duan, W. (2009). Molecular and atomic adsorption of hydrogen on TiO<sub>2</sub> nanotubes: an ab initio study. *Chemical Physics Letters*, 475, 82–85.
- [12] Anukunprasert, A. (2005). The development of gas sensor for carbon

monoxide monitoring using nanostructure of Nb-TiO<sub>2</sub>. *Science and Technology of Advanced Materials*, 6 (3-4), 359-363.

- [13] **Li, Y., Wlodarski, W., Galatsis, K., Moslih, S.H., Cole, J., Russo, S. and Rockelmann, N.** (2002). Gas sensing properties of p-type semiconducting Cr-doped TiO<sub>2</sub> thin films. *Sensors and Actuators B*, 83, 160-163.
- [14] **Yamada, Y., Seno, Y., Masuoka, Y., Nakamura, T. and Yarashita, K.** (2000). NO<sub>2</sub> sensing characteristics of Nb doped TiO<sub>2</sub> thin films and their electronic properties. *Sensors and Actuators B: Chemical*, 66 (1-3), 164-166.
- [15] **Sharma, R.K., Bhatnagar, M.C. and Sharma, G.L.** (1997). Mechanism of highly sensitive and fast response Cr doped TiO<sub>2</sub> oxygen gas sensor. *Sensors and Actuators B Chemical*, 45 (3), 209-215.
- [16] **Ruiz, A.M., Sakai, G., Cornet, A., Shimanoe, K., Morante, J.R. and Yamazoe, N.** (2003). Cr-doped titania gas sensor for exhaust NO<sub>2</sub> monitoring. *Sensors and Actuators B*, 93, 509-518.
- [17] **Savage, N., Chwieroth, B., Ginwalla, A., Patton, B.R., Akbar, S.H. and Dutta, P.K.** (2001). Composite n-p semiconducting titanium oxides as gas sensors. *Sensors and Actuators B: Chemical*, 79 (1), 17-27.
- [18] **Alessandri, I., Comini, E., Bontempi, E., Faglia, G., Depero, L. and Sberveglieri, G.** (2007). Cr-inserted TiO<sub>2</sub> thin films for chemical gas sensors. *Sensors and Actuators, B: Chemical*, 128 (1), 312-319.
- [19] **Varghese, O.K., Gong, D., Paulose, M., Ong, K.G. and Grimes, C.A.** (2003). Hydrogen sensing using titania nanotubes. *Sensors A and Actuators B*, 93, 338-344.
- [20] **Mohammadi, D.J. and Fray, M.R.** (2007). Semiconductor TiO<sub>2</sub>-Ga<sub>2</sub>O<sub>3</sub> thin film gas sensors derived from particulate sol-gel route. *M.R. Acta Materialia*, 55 (13), 4455-4466.
- [21] **Mohammai, D.J. and Fray, M.R.** (2009). Development of nanocrystalline TiO<sub>2</sub>-Er<sub>2</sub>O<sub>3</sub> and TiO<sub>2</sub>-Ta<sub>2</sub>O<sub>5</sub> thin film gas sensors: controlling the physical and sensing properties. *Sensors and Actuators, B: Chemical*, 141 (1), 76-81.
- [22] **Ruiz, A.** (2002). Preparation of Cr-doped TiO<sub>2</sub> thin film of p-type conduction for gas sensor application. *Chemistry Letters*, 9, 892-893.
- [23] **Savage, N.** (2001). Composite n-p semiconducting titanium oxides as gas sensors. *Sensors and Actuators B: Chemical*, 79 (1), 17-27.
- [24] **Ruiz, A.M., Sakai, G., Cornet, A., Shimanoe, K., Morante, J.R. and Yamazoe, N.** (2003). Cr-doped titania gas sensor for exhaust NO<sub>2</sub> monitoring. *Sensors and Actuators B*, 93, 509-518.
- [25] **Sharma, R.K., Bhatnagar, M.C. and Sharma, G.L.** (1997). Mechanism of highly sensitive and fast response Cr doped TiO<sub>2</sub> Oxygen gas sensor. *Sensors and Actuators B Chemical*, 45 (3), 209-215.
- [26] **Ren, F., Ling, Y. and Feng, J.** (2010). The role of W doping in response of hydrogen sensors based on MAO titania films. *Applied Surface Science*, 256, 3735-3739.

- [27] **Sotter, E., Vilanova, X., Llobet, E. and Stankova, M.** (2005). Niobium-doped titania nanopowders for gas sensor applications. *Journal of Optoelectronics and Advanced Materials*, 7 (3), 1395-1398.
- [28] **Ferroni, M., Carotta, M.C., Guidi, V., Martinelli, F., Ronconi, O., Richard, D., Dyck, V. and Landuyt, J.** (2000). Structural characterization of Nb-TiO<sub>2</sub> nanosized thick films for gas sensing application. *Sensors and Actuators B: Chemical*, 68 (1-3), 140-145.
- [29] **Shimizu, K.** (2008). Impedancemetric gas sensor based on Pt and WO<sub>3</sub> Co-loaded TiO<sub>2</sub> and ZrO<sub>2</sub> as total NO<sub>x</sub> sensing materials. *Sensors and Actuators B-Chemical*, 130 (2), 707-712.
- [30] **Ferroni, D., Boscarino, E., Comini, D., Gnan, V., Guidi, G., Martinelli, P., Nelli, V., Rigato and G., Sberveglieri.** (1999). Nanosized thin films of tungsten-titanium mixed oxides as gas sensors. *Sensors and Actuators B: Chemical*, 58 (1-3), 289-294.
- [31] **Nelli, P., Depero, L.E., Ferroni, M., Groppelli, V., Guidi, F., Ronconi, L. and Sangaletti, G.** (1996). Sub-ppm NO<sub>2</sub> sensors based on nanosized thin films of titanium-tungsten oxides. *Sensors and Actuators B: Chemical*, 31 (1-2), 89-95.
- [32] **Akbar, S.A.** (1998). Selectivity of an anatase TiO<sub>2</sub>-based gas sensor. *Polymers in Sensors*, 690, 161-167.
- [33] **Ferroni, M., Carotta, C., Guidi, V., Martinelli, G., Ronconi, F., Sacerdoti, M. and Traversa, E.** (2001). Preparation and characterization of nanosized titania sensing film. *Sensors and Actuators B: Chemical*, 77 (1-2), 163-166.
- [34] **Wisioraar, A., Tuantranont, E., Comini, G., Sberveglieri, W. and Wlodarski, A.** (2009). Characterization of n-type and p-type semiconductor gas sensors based on NiO<sub>x</sub> doped TiO<sub>2</sub> thin films. *Thin Solid Films*, 517 (8), 2775-2783.
- [35] **Choi, Y.J., Seeley, Z., Bandyopadhyay, A., Bose, S. and Akbar, S.A.** (2007). Aluminum-doped TiO<sub>2</sub> nano-powders for gas sensors. *Sensors and Actuators B*, 124, 111-117.
- [36] **Birkefeld, L.D., Azad, A.M. and Akbar, S.A.** (1992). Carbon monoxide and hydrogen detection by anatase modification of titanium dioxide. *Journal of the American Ceramic Society*, 75, 11-15.
- [37] **Hanaor, D.A.H. and Sorrell, C.C.** (2011). Review of the anatase to rutile phase transformation. *J. Mater. Science*, 46, 855-874.
- [38] **Joskowsk, D., Pomoni, K., Vomvas, A., Kościelska, B. and Anastassopoulos, D.L.** (2010). Electrical and photoconductive properties of mixed Nb<sub>2</sub>O<sub>5</sub>/TiO<sub>2</sub> sol gel thin films. *Journal of Non-Crystalline Solids*, 356 (37-40), 2042-2048.
- [39] **Comini, E., Ferroni, M., Guidi, V., Vomiero, A., Merli, P.G., Morandi, V., Sacerdoti, M., Della Mea, G. and Sberveglieri, G.** (2005). Effects of Ta/Nb doping on titania based thin film gas sensor. *Sensors and Actuators B*, 108, 21-28.

- [40] Talavera, R.R., Vargas, S., Murillo, R.A., Campos, R.M. and Poniatowski, E.H. (1997). Modification of the phase transition temperatures in titania doped with various cations. *Journal of Materials Research*, 12 (2), 439-443.
- [41] Suresh, C., Biju, V., Mukundan, P. and Warriar, K.G.K. (1998). Anatase to rutile transformation in sol-gel titania by modification of precursor. *Polyhedron*, 6, 3131-3135.
- [42] Kumar, S.R., Pillai, S.C, Hareesh, U.S., Mukundan, P. and Warriar, K.G.K. (2000). Synthesis of thermally stable, high surface area anatase–alumina mixed oxides. *Materials Letters*, 43, 286–290.
- [43] Yang, J. and Ferreira, J.M.F. (1998). Inhibitory effect of the Al O –SiO mixed additives on the anatase–rutile phase transformation. *Materials Letters*, 36, 320–324.
- [44] Depero, L. E., Marino, A., Allieri, B., Bontempi, E., Sangaletti, L., Casale, C. and Notaro, M. (2000). Morphology and microstructural properties of TiO<sub>2</sub> nanopowders doped with trivalent Al and Ga cations. *Journal of Materials Research*, 15 (10), 2080-2086.
- [45] Carotta, M. C., Ferroni, M., Gnani, D. Guidi, V., M. Merli, Martinelli, G., Casale, M. and Notaro, M. (1999). Nanostructured pure and Nb doped TiO<sub>2</sub> as thick film gas sensors. *Sensors and Actuators B* 58, 310-317.
- [46] Bonini, N., Carotta, M.C., Chiorino, A., Guidi, V., Malagu, C., Martinelli, G., Paglialonga, L. and Sacerdoti, M. (2000). Doping of a nanostructured titania thick film: structural and electrical investigations. *Sensors and Actuators B*, 68, 274-280.
- [47] Sharma, R.K. and Bhatnagar, M.C. (1999). Improvement of the oxygen gas sensitivity in doped TiO thick films. *Sensors and Actuators B*, Vol 56, 215–219.
- [48] Kazuhito, H., Higuchi, M., Takahashi, J. and Kohei, K. (1996). Floating zone growth and characterization of aluminum-doped rutile single crystals. *Journal of Crystal Growth*, 163 (3), 279-284.
- [49] Hazra, S. and Basu, S. (2006). High sensitivity and fast response hydrogen sensors based on electrochemically etched porous titania thin films. *Sensors and Actuators B*, 115, 403–441.
- [50] Chaudhari, G. N., Bambole, D. R., Bodade, A.B. and Padole, P.R. (2006). Characterization of nanosized TiO<sub>2</sub> based H<sub>2</sub>S gas sensor. *Journal of Material Science*, 41, 4860–4864.
- [51] Ding, X., Liu, L., Ma, X., Qi, Z. and He, Y. (1994). The influence of alumina dopant on the structural transformation of gel-derived nanometre titania powders. *Journal of Materials Science Letters*, 13 (6), 462-464.
- [52] Hatta, K., Higuchi, M., Takahashi, J. and Kodaira, K. (1996). Floating zone growth and characterization of aluminum-doped rutile single crystals. *Journal of Crystal Growth*, 163, 279-284.



- [53] **Liu, S., Liu, G. and Feng, Q.** (2010). Al-doped TiO<sub>2</sub> mesoporous materials: synthesis and photodegradation properties. *J. Porous Mater.*, 17, 197–206.
- [54] **Kumar, S.R., Pillai, S.C, Hareesh, U.S., Mukundan, P. and Warriar, K.G.K.** (2000). Synthesis of thermally stable, high surface area anatase–aluminum mixed oxides. *Materials Letters*, 43, 286–290.
- [55] **Akhtar, K.M., Pratsinis, S.E. and Mastrangelo, S.V.R.** (1994). Vapor phase synthesis of Al-doped titania powders. *Journal of Materials Research*, 9 (5), 1241–1249.
- [56] **Zhang, J., Li, M., Feng, Z., Chen, J, Li, C.** (2006). UV Raman spectroscopic study on TiO<sub>2</sub> phase transformation at the surface and in the bulk. *J. Phys. Chem. B*, 110, 927–935.
- [57] **Yang, J., Huang, Y.X. and Ferreira, J.M.F.** (1997). Inhibitory effect of alumina additive on the titania phase transformation of a sol-gel-derived powder. *Journal of Materials Science Letters*, 16, 1933–1935.
- [58] **Choi, Y.J., Bandyopadhyay, A. and Bose, S.** (2005). Nanostructured alumina doped TiO<sub>2</sub> ceramics for gas sensors. *MRS Conference*, Boston, CA, USA: November 23–28.
- [59] **Lee, J.E., Ohb, S.M. and Parka, D.W.** (2004). Synthesis of nano-sized Al doped TiO<sub>2</sub> powders using thermal plasma. *Thin Solid Films*, 457, 230–234.
- [60] **Cheng, Y., Kuo, T. and Hsi, H.** (2012). Fabrication of Al-doped TiO<sub>2</sub> visible-light photocatalyst for low-concentration mercury removal. *International Journal of Photoenergy*, 2012, 1–8.
- [61] **Xu, L., Garrett, M.P. and Hu, B.** (2012). Doping effects on internally coupled seebeck coefficient, electrical, and thermal conductivities in aluminum-doped TiO<sub>2</sub>. *J. Phys. Chem. C*, 116, 13020–13025.
- [62] **Badadhe, S.S. and Mulla, I.S.** (2011). Effect of aluminium doping on structural and gas sensing properties of zinc oxide thin films deposited by spray pyrolysis. *Sensors and Actuators B*, 156, 943–948.
- [63] **Gesenhues, U.** (2001). Al-doped TiO<sub>2</sub> pigments: influence of doping on the photocatalytic degradation of alkyd resins. *Journal of Photochemistry and Photobiology A: Chemistry*, 139, 243–251.
- [64] **Islam, M.M., Bredow, T. and Gerson, A.** (2007). Electronic properties of oxygen-deficient and aluminum-doped rutile TiO<sub>2</sub> from first principles. *Physical Review B*, 76, 45217–45226.
- [65] **Pena, P. and DeAza, S.** (1992). *Phase diagrams for ceramists*. Ohio: The American Ceramic Society.
- [66] **Mor, G. K., Varghese, O.K., Paulose, M., Shankar, K. and Grimes, C.A.** (2006). A review on highly ordered, vertically oriented TiO<sub>2</sub> nanotube arrays: fabrication, material properties, and solar energy applications. *Solar Energy Materials & Solar Cells*, 90, 2011–2075.
- [67] **Barsan, N. and Weimar, U.** (2001). Conduction model of metal oxide gas sensors. *Journal of Electroceramics*, 7, 143–167.

- [68] **Mor, G.K., Varghese, O.K., Paulose, M., Ong, K.G and Grimes, C.A.** (2006). Fabrication of hydrogen sensors with transparent titanium oxide nanotube-array thin films as sensing elements. *Thin Solid Films*, 496 (1), 42-48.
- [69] **Yongxiang, L.** (2009). Fabrication of TiO<sub>2</sub> nanotube thin films and their gas sensing properties. *Journal of Sensors*, 1687-725, 1-19
- [70] **Lu, C. and Chen, Z.** (2009). High-temperature resistive hydrogen sensor based on thin nanoporous rutile TiO<sub>2</sub> film on anodic aluminum oxide. *Sensors and Actuators B*, 140, 109–115.
- [71] **Şennik, E., Çolak, Z.C., Kılınç, N. and Öztürk, Z.Z.** (2010). Synthesis of highly-ordered TiO<sub>2</sub> nanotubes for a hydrogen sensor. *International Journal of Hydrogen Energy*, 34, 4420-4427.
- [72] **Paulose, M., Varghese, O.K., Mor, G.K, Grimes, C.A and Ong, K.G.** (2006). Unprecedented ultra-high hydrogen gas sensitivity in undoped titania nanotubes. *Nanotechnology*, 17(2), 398-402.
- [73] **Seo, M.H., Yuasa, M., Kida, T., Huh, J., Yamazoe, N. and Shimanoe, K.** (2009). Detection of organic gases using TiO<sub>2</sub> nanotube-based gas sensors. *Procedia Chemistry*, 1 (1), 192-195.
- [74] **Sadek, A.Z., Partridge, J.G., McCulloch, D.G., Li, Y.X., Yu, X.F., Wlodarski, W. and Kalantarzadeh, K.** (2009). Nanoporous TiO<sub>2</sub> thin film based conductometric H<sub>2</sub> sensor. *Thin Solid Films*, 518, 1294–1298.
- [75] **Chu, S.Z., Inoue, S., Wada, K., Li, D. and Suzuki, J.** (2005). Fabrication and photocatalytic characterizations of ordered nanoporous x-doped (X- N, C, S, Ru, Te, and Si) TiO<sub>2</sub>/Al<sub>2</sub>O<sub>3</sub> Films on ITO/Glass. *Langmuir*, 21, 8035-8041.
- [76] **Paulose, M., Peng, L., Popat, K.C., Varghese, O.K., Latempa, T.J., Bao, N.J., Desai, T.A. and Grimes, C.A.** (2008). Fabrication of mechanically robust, large area, polycrystalline nanotubular/porous TiO<sub>2</sub> membranes. *Journal of Membrane Science*, 319, 199–205.
- [77] **Yang, H.** (2008). Fabrication and characterization of highly-ordered titania nanotubes via electrochemical anodization. *Materials Letters*, 62, 2688–2691.
- [78] **Grimes, C.A., Ong, K.G. and Varghese, O.K.** (2003). Sensor network for hydrogen sensing. *Sensors*, 3, 69-82.
- [79] **Mor, G.,K., Shankar, K., Paulose, M., Varghese, O.K. and Grimes, C.A.** (2005). Enhanced photocleavage of water using titania nanotube arrays. *Nano Letters*, 5 (1), 191-195.
- [80] **Raja, K.S., Misra, M. and Paramguru, K.** (2005). Formation of self-ordered nano-tubular structure of anodic oxide layer on titanium. *Electrochimica Acta*, 51, 154–165.
- [81] **Liu, S.** (2008). Synthesis and characterization of self organized oxide nanotube arrays via a facile electrochemical anodization. *J.Phys. Chem. C*, 112, 19852-19859.

- [82] **Macak, M., Tsuchiya, H., Taveria, L., Ghicov, A. and Schmuki, P.** (2005). Self-organized nanotubular oxide layers on Ti-6Al-7Nb and Ti-6Al-4V formed by anodization in  $\text{NH}_4\text{F}$  solutions. *Journal of Biomedical Materials Research Part A*, 75 (4), 928-933.
- [83] **Bayoumi, F.M. and Ateya, B.G.** (2006). Formation of self-organized titania nano-tubes by dealloying and anodic oxidation. *Electrochemistry Communications*, 8, 38-44.
- [84] **Tsuchiya, H.** (2007). Self-organized porous and tubular oxide layers on TiAl alloys. *Electrochemistry Communications*, 9, 2397-2402.
- [85] **Comini, E., Faglia, G., Sberveglieri, G., Alessandri, I., Bontempi, E. and Depero, L.E.** (2005). Characterization of p-type Cr :  $\text{TiO}_2$  gas sensor. *Ieee Sensors*, 3, 1320-1322.
- [86] **Homoudi, I.A., Thakur, J.S., Naik, R., Auner, G.W. and Newaz, G.** (2007). Anatase  $\text{TiO}_2$  films based CO gas sensor: film thickness, substrate and temperature effects. *Applied Surface Science*, 253 (21), 8607-8614.
- [87] **Homoudi, K.** (2006). Anatase  $\text{TiO}_2$  thin films based CO gas sensor. *Material and Devices for Smart Systems*, 888, 283-288.
- [88] **Chou, J.** (2006). Study of the characteristics of titanium oxide hydrogen ion sensor using XRD and AES. *Rare Metal Materials and Engineering*, 35, 250-251.
- [89] **Sanders, D.M. and Anders, A.** (2000). Review of cathodic arc deposition technology at the start of the new millennium. *Surface and Coatings Technology*, 133-134, 78-90.
- [90] **Corlu, B. and Urgan, M.** (2010). Modification of copper surfaces with cathodic arc aluminum plasma. *Surface and Coatings Technology*, 205 (2), 540-544.
- [91] **Arpat, E. and Urgan, M.** (2011). Production of free standing Cu-Al intermetallics by cathodic arc plasma treatment. *Intermetallics*, 19 (12), 1817-1822.
- [92] **Massalski, T.B.** (Ed.). (1990). *Binary Alloy Phase Diagrams*. Ohio: ASM International.
- [93] **Diebold, U.** (2003). The surface of titanium oxide. *Surface Science Reports*, 48 (5-8), 53-229.
- [94] **Sun, J., Gao, L., and Zhang, Q.** (2003). Synthesizing and comparing the photocatalytic properties of high surface area rutile and anatase titania nanoparticles. *Journal of the American Society*, 86 (10), 1677-1682.
- [95] **Suzana, M., Francisco, P. and Mastelaro, V.R.** (2002). Inhibition of the anatase-rutile phase transformation with additon of  $\text{CeO}_2$  to  $\text{CuO-TiO}_2$ . *Chem. Mater.*, 14, 2514-2518.
- [96] **Chang, H. and Huang, P.J.** (1998). Thermo-Raman studies on anatase and rutil. *Journal of Raman Spectroscopy*, 29 (2), 97-102.

- [97] **Varghese, O.K.** (2012). Crystallization and high-temperature structural stability of titanium oxide nanotube arrays. *J. Mater. Res.*, 18 (1), 156-165.
- [98] **Gouma, P.I. and Mills, M.J.** (2001). Anatase-to-rutile transformation in titania powders. *J. Am. Ceram. Soc.*, 84, 619-622.
- [99] **Kim, S.K., Choi, G.J., Kim, J.H. and Hwang, C.S.** (2008). Growth behavior of Al-doped TiO<sub>2</sub> thin films by atomic layer deposition. *Chem. Mater.*, 20, 3723–3727.
- [100] **Kim, S.K., Choi, G., Lee, S.Y., Han, J.H., Ahn, H., Han, S. and Hwang, C.D.** (2008). Al-doped TiO<sub>2</sub> films with ultralow leakage currents for next generation DRAM capacitors. *Advanced Materials*, 20 (8), 1429-1435.
- [101] **Kim, D., Rothschild, A. and Tuller, H.L.** (2013). Advances and new directions in gas-sensing devices. *Acta Materialia*, 61, 974–1000.

## **APPENDICES**

**APPENDIX A:** The response graph of the nanotubular TiAl anodic oxide against different H<sub>2</sub> concentrations at various temperature

## APPENDIX A

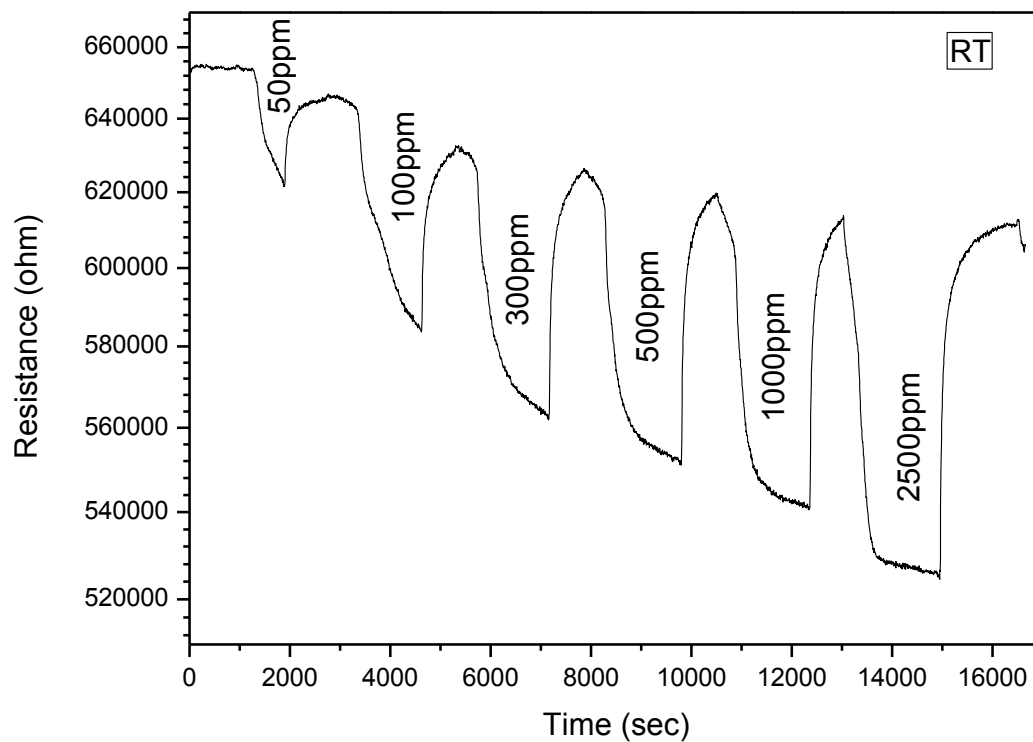


**Figure A.1 :** The response graph of the nanotubular TiAl anodic oxide against different H<sub>2</sub> concentrations at room temperature.

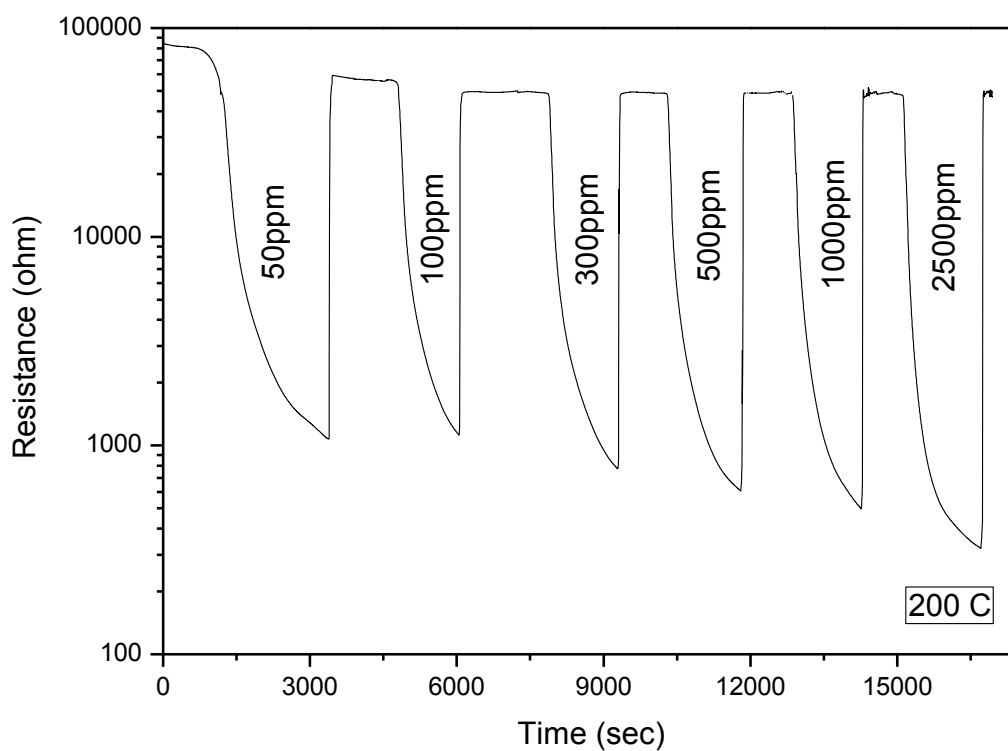


**Figure A.2 :** The response graph of the nanotubular TiAl anodic oxide against different H<sub>2</sub> concentrations at 200°C.

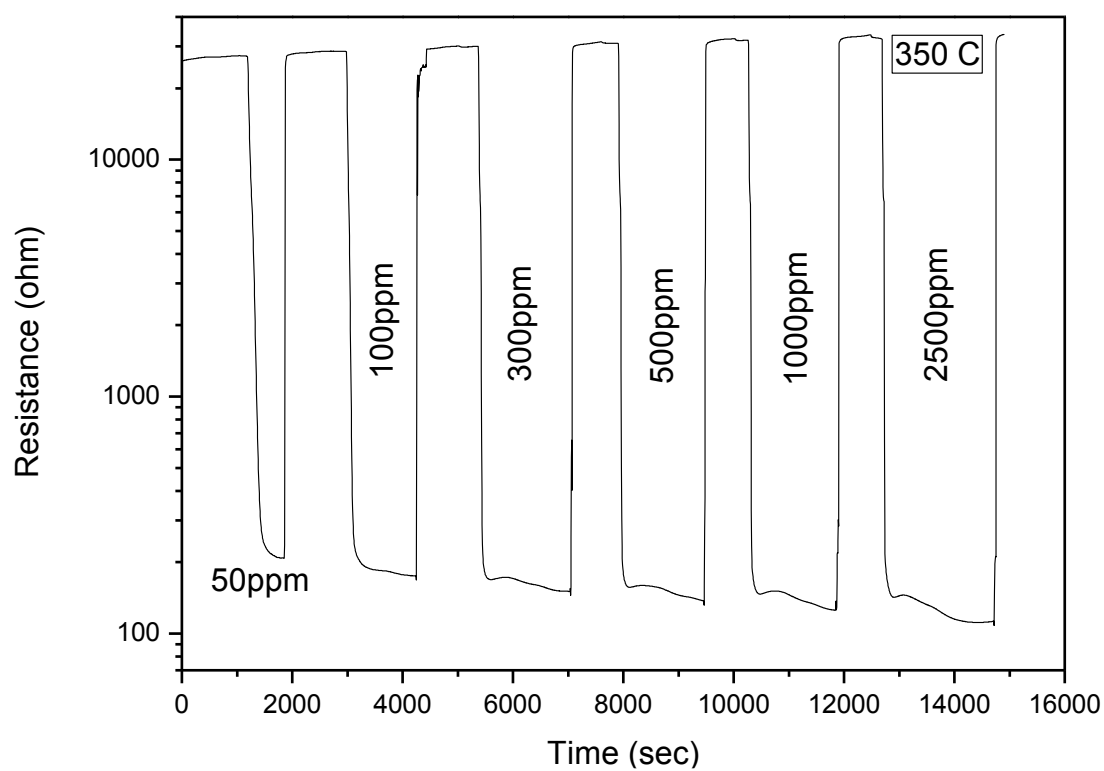


**Figure A.3 :** The response graph of the nanotubular TiAl anodic oxide against different  $H_2$  concentrations at  $350^\circ\text{C}$ .





## CURRICULUM VITAE



**Name Surname:** Fatma BAYATA  
**Address:** İTÜ Maslak Lojmanları D2-77 Şişli/İstanbul  
**E-Mail:** fbayata@yahoo.com  
**B.Sc.:** İTÜ Dept. Chemistry  
**M.Sc.:** İTÜ Polymer Science & Technology

### List of Publications:

1. N. S. Tuzun, **F. Bayata**, A. S. Sarac “An experimental and quantum mechanical study on electrochemical properties of N-substituted pyrroles Original Journal of Molecular Structure: THEOCHEM, Volume 857, Issues 1–3, 30 May 2008, Pages 95-104
2. **F. Bayata**, Z. B. Akinci, A. S. Donatan, M. Urgan “A novel free-standing nanowire substrate with surface enhanced Raman scattering (SERS) activity” Materials Letters, Volume 67, Issue 1, 15 January 2012, Pages 387-389.
3. M. Urgan, Ö. Keles, B. D. Polat, **F. Bayata** “Generation of a Surface Pattern Having Conical Surface Features by Anodic Polarization of Aluminum” J. Electrochem. Soc. 2012 159(9): C411-C415.

### List of Presentations:

1. **F.Bayata**, F.Karaosmanoğlu “Biodiesel production”, Chamber of Mechanical Engineers, Istanbul, 2006.
2. B. Saruhan, A. Yüce, **F. Bayata**, M. Ürgen, “Development of high efficiency integrated gas sensors with nanorod sensing electrode of doped oxides”, The American Ceramic Society, Electronic Materials and Applications Meeting, Florida, 2010.
3. **F.Bayata**, M.Urgan, N. Solak, “A Novel Fabrication Technique For Free Standing Nickel Nanowires And Their Possible Applications” ICMCTF-SanDiego, 2011.

4. **F.Bayata**, Y. Gönüllü, M. Ürgen, B. Saruhan, “The Hydrogen Sensing Properties of Nanotubular TiO<sub>2</sub>, Al-TiO<sub>2</sub> and Cr-TiO<sub>2</sub> Sensor Materials”, International Symposium on Surface Modification Technologies, Istanbul, 2011.
5. B. D. Polat, **F. Bayata**, Ö. Keleş, and M. Urgen “Surface Patterning of Aluminum in H<sub>3</sub>PO<sub>4</sub> and H<sub>2</sub>SO<sub>4</sub> Mixtures and Using Them as Templates for Fabrication of Free Standing Nanowires” 220th ECS Meeting - Boston, MA, 2011
6. Z.B. Akıncı, **F. Bayata**, M. Urgen, A Novel Free Standing Gold Nanowire Substrate For Surface Enhanced Raman Scattering Activity SERS, International Symposium on Surface Modification Technologies, Istanbul, 2011.
7. Y. Gönüllü, A. Yüce, G. Montragon-Rodrigues, B. Saruhan, **F.Bayata**, M. Ürgen, “Effect of Doping at TiO<sub>2</sub>- Nanotubular Gas Sensors”, Sensor+Test Conferences, Germany, 2011.